Effects of finite Rossby radius on vortex-boundary interactions

Rahul Suresh Nilawar

Department of Mathematics
University College London
Gower Street
London
WC1E 6BT

A THESIS SUBMITTED FOR THE DEGREE OF DOCTOR OF PHILOSOPHY

Supervisors: N. R. McDonald & E. R. Johnson

APRIL 2012

"For when you are put into the Vortex you are given just one momentary glimpse of the entire unimaginable infinity of creation, and somewhere in it a tiny little marker, a microscopic dot on a microscopic dot, which says 'You are here'. "

−Douglas Adams, The restaurant at the end of the universe

I, Rahul Suresh Nilawar, confirm that the work presented in this thesis is my own. Where information has been derived from other sources, I confirm that this has been indicated in the thesis.

SIGNED

Abstract

The effect of the finite Rossby radius on vortex motion is examined in a two-dimensional inviscid incompressible fluid, assuming quasigeostrophic dynamics in a single layer of fluid with reduced gravity for two geophysically significant problems: a vortex near a gap in a wall and a pair of steady translating vortices.

For the motion of a point vortex near a gap in an infinite barrier, a key parameter determining the behaviour of the vortex is a, the ratio of the Rossby radius of deformation and the half-width of the gap. For large a, depending on the location of the vortex, a vortex sheet is placed either over the gap (gap method) or over the two semi-infinite barriers (barrier method). When the vortex sheet is over the gap, numerical inaccuracies are encountered when the vortex is close to the gap, therefore the conjugate (barrier) method is used. Both integral equations contain singularities which can be de-singularised and solved iteratively using the known exact solution in rigid-lid limit, i.e. $a \to \infty$. For large a, there is only slight deviation from the analytical ($a \to \infty$) trajectories.

For smaller a, the integral equation from the conjugate method is solved by numerically approximating the integral equation into a system of linear equations and solving using matrix inversion. The integral equation is further simplified by splitting into even and odd parts, thus reducing the problem to the half plane. It is also found that decreasing a, increases the tendency for vortices to pass through the gap.

Background flows influence vortex trajectories and are incorporated by modifying the conjugate method integral equation. These equations are solved using the matrix method. Streamlines for uniform symmetric and anti-symmetric (which has no analogy in the rigid-lid limit) flow through the gap are computed and their effect on the vortex trajectories are found.

The motion of finite area patches of constant vorticity near a gap in a wall is computed using the matrix method in conjunction with contour dynamics. For

fixed a, vortex patches are normalised to travel at the same speed as a point vortex. The normalisation is non-trivial and depends nonlinearly on the patch area and a. In the rigid-lid limit, it reduces to the 'usual' normalisation based on the patch circulation. For near circular patches, the trajectory of the centroid of the patches also follows the trajectory of the point vortices. When the patch becomes distorted the agreement is not so close. The splitting and joining of contours is also computed using contour surgery and some examples showing this sudden change of behaviour is presented.

The next problem determines the effect of the Rossby radius of deformation, on steady translating vortex pairs or, equivalently, a patch in steady translation near a wall. The velocities for the normalised vortex patch are compared to the velocity of a point vortex located at the centroid of the patch. It is found there is good agreement for a range of patch sizes. When the patches are sufficiently far from the wall, decreasing the Rossby radius makes the steadily translating shapes more circular. However, when close to the wall, the effect of the Rossby radii results in patches deforming greatly, forming long slug-like shapes. These are shown to be stable using a time dependent contour dynamics code. Background flows are also incorporated and give different vortical shapes for finite Rossby radii flows, ranging from slug-like to tear-drop in shape.

Acknowledgements

I owe a huge debt of gratitude to both my supervisors, Robb McDonald and Ted Johnson, whose enthusiasm and passion for vortex dynamics were a continual source of inspiration. I feel truly privileged to have benefitted from their experience and knowledge of the field. I would like to thank them for the patience and support with which they have advised me.

I would like to thank my fellow postgrads who have provided me with stimulating conversation and copious amounts of tea and coffee; the fuel that drives mathematicians. In particular, I would like to thank Rhodri Nelson for insightful comments about contour dynamics and pearl jam. I also wish to acknowledge the support of UCL and NERC for the funding I received during my Ph.D. and thank the administrative staff of the Mathematics department who helped me obtain it.

I also wish to acknowledge the contribution of my former maths teacher, Kishore Naik. He taught me that there was more to maths than calculating compound interest. His enthusiasm and encouragement instilled in me my love for the subject and my desire to pursue it. For this I am eternally grateful.

I am sincerely grateful to my friends who have helped me take my mind off research. I'd like to thank everyone in Sliced Alone for all the great times at the Sheephaven Bay. I'd also like to thank Lukman Chowdhury for taking time out on a weekly basis to allow me to beat him at cards.

Without my girlfriend's faith in me, this thesis would not be possible. Bron, I can't even begin to thank you enough.

Last but not least, I would like to thank my parents and my sisters who have always believed in me and supported me in everyway possible. This is dedicated to them.

ॐ नमः शिवाय

Contents

Chapter 1

Introduction

1.1 Background and motivation

The systematic study of fluid mechanics has its origins in ancient Greece. Before his deat in 212 B.C., Archimedes famously discovered his eponymous principle relating the displacement of fluid to buoyancy. Before the discovery of calculus, hydrostatics was studied widely leading to the production of tools such as the hydraulic press and the forcing pump. Euler (1757) was one of the first to extend the static principles of fluid mechanics to dynamic ones by deriving equations of motion for an ideal fluid based on Newton's laws using calculus, and the formulation of these equations allowed fluid dynamics to become a key field of applied mathematics.

Helmholtz (1858) was the the first to define the concept of a vortex filament in his seminal work, '*Über integrale der hydrodynamischen Gleichungen, welche den wirbelbewegungen entsprechen*'. The translation of this paper by Tait (1867) inspired Kelvin to develop his theory of vortex atoms (Kelvin, 1867) and more importantly his eponymous circulation theorem (Kelvin, 1869) which proves that circulation is conserved around a material contour within an ideal fluid. By the early twentieth century the subject of vortex dynamics had become an important subfield of fluid dynamics owing to its many applications in physics, engineering and mathematics.

As famously noted by Küchemann (1965), vortices are the 'sinews and muscles of fluid motions'.

The scope of this work has its basis in the realm of geophysical fluid dynamics, in particular vortex-vortex and vortex-boundary interactions. It is well known that instabilities present in ocean currents cause mesoscale (i.e. 20∼200 km in width) eddies to be shed. These eddies are intense localised flows which rotate about the vertical (i.e. gravitational) axis, and are roughly circular. They are stable structures able to traverse large distances and in some cases, have been tracked for several years. They contribute significantly to the global transport and mixing of properties such as momentum, heat and salt. During their lifetime, ocean eddies frequently encounter topographic features such as island chains, narrow straits and gaps between ocean basins. Their ability to influence the large scale ocean circulation and hence the climate system, means that understanding vortex motion, particularly in the presence of topographic features, is of vital importance.

In such systems, a low Mach number is assumed as well as a high Reynolds number. Hence, the fluid in the mathematical model is assumed to be incompressible and inviscid. Furthermore, two dimensional flows are studied in particular as the vertical displacements in the fluid are considered negligible with respect to the the horizontal displacements.

This chapter presents a derivation of the fundamental equations considered in the thesis as well as a discussion of the related point vortex solutions.

1.2 Model of the ocean

The problems considered in the following chapters investigate the two dimensional motion of vortices in an ideal geophysical fluid. A reduced gravity shallow water system is used to model the ocean. The top layer is considered to be the active shallow layer, where the vortex resides and it is separated from the deep stagnant ocean by the thermocline. The thermocline is the thin but distinct transistional layer where the temperature changes abruptly between the upper active layer and the lower stagnant layer. Within the deep stagnant layer, the fluid has greater density and does not interact dynamically with the top layer. Equivalently, the active layer could represent a thin dense layer at the bottom of the ocean above which lies a stagnant upper ocean.

Small oscillations in the free surface (the air-sea interface) are allowed. By scaling the shallow water equations and expanding in a small parameter, the Rossby number R_0 (to be defined later) which measures the relative importance of inertial effects to rotational effects, a quasigeostrophic system is devised. This is one of the most widely used dynamical models for the theoretical study of the atmosphere and ocean (see Vallis 2006). Although these approximations simplify the dynamics of the ocean, the results obtained give insight into the effects of the Rossby radius of deformation (to be defined) on the dynamics of ocean vortices. The derivation of reduced gravity quasigeostrophic potential vorticity equation system is given in the next section.

1.2.1 Reduced gravity shallow water equations

Consider a shallow top layer, with density $\rho = \rho_0$ and free upper surface given by $z = h_0(x, y, t)$ above a layer of deep, stagnant (i.e. velocity $\mathbf{u} = 0$) fluid with a greater density $\rho = \rho_1$. The interface between the two layers is described by $z = h_1(x, y, t)$. The system experiences constant rotation about the $\mathbf{k}$ axis,

$$\boldsymbol{\Omega} = \frac{f}{2}\mathbf{k}, \tag{1.1}$$

where f is the (constant) Coriolis parameter (which is the frequency of the Earth's rotation) and the unit vector $\mathbf{k}$ is in the direction against gravity. The depth of the undisturbed upper layer is D. A typical horizontal length scale is given by L. A schematic of the system is shown in Fig. 1.1.

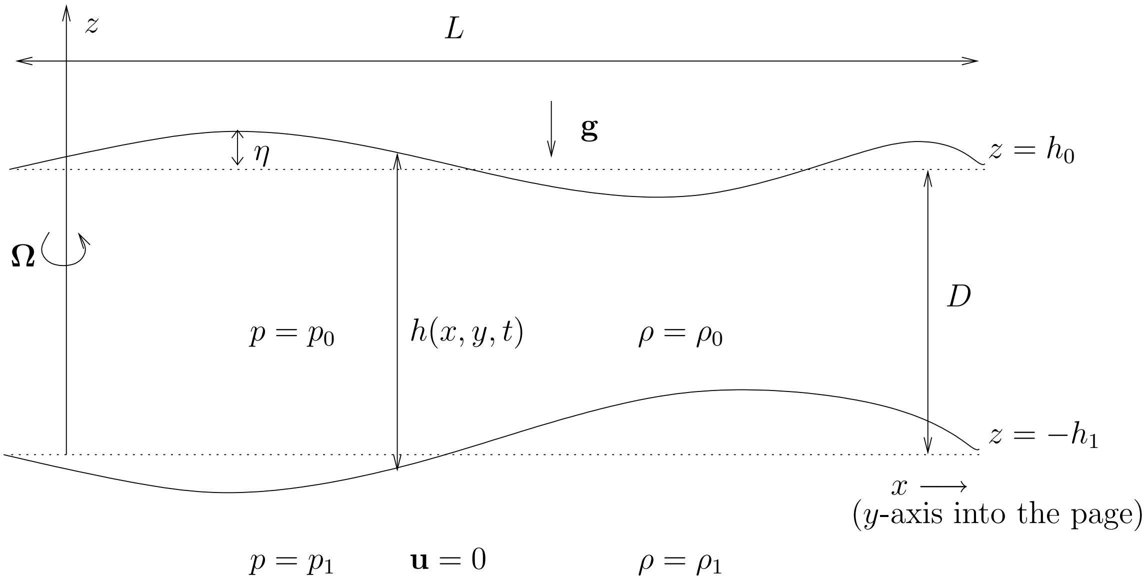

Figure 1.1: Two layer system. Top layer is shallow and active. The bottom layer is deep and stagnant.

The momentum equation of the top layer is given by

$$\frac{D\mathbf{u}}{Dt} + f\mathbf{k} \times \mathbf{u} = -\frac{1}{\rho_0}\nabla p_0 - \boldsymbol{\Phi} + \mathbf{F}, \tag{1.2}$$

where $\mathbf{u}$ is the velocity field, $p_0(x, y, z, t)$ is the pressure in the top layer, $\boldsymbol{\Phi}$ is the gravitational potential per unit mass, $\mathbf{F}$ represents other external forces and the operator D/Dt is given by

$$\frac{D}{Dt} = \frac{\partial}{\partial t} + \mathbf{u} \cdot \nabla. \tag{1.3}$$

For our purposes, $\mathbf{F} = \mathbf{0}$, i.e. the effects of friction and dissipation are ignored, this being a reasonable approximation for the large length scales involved in oceanic mesoscale vortex dynamics. In the ocean the vertical scale of the fluid is small compared to the horizontal scale ($D \ll L$), so we can make the hydrostatic assumption i.e. the vertical pressure gradient is balanced by the gravitational force. Thus, we can calculate the pressure in the active layer:

$$p_0 = \rho_0 g(h_0 - z),\ h_1 \le z \le h_0 \tag{1.4}$$

and for the bottom layer, due to the added weight of the top layer,

$$p_1 = \rho_0 g(h_0 - h_1) + \rho_1 g(h_1 - z),\ z \leq h_1. \tag{1.5}$$

As the bottom layer is quiescent, the horizontal pressure gradient is zero. That is, at any given value of z, p_1 must be independent of x and y. It follows that there is a relation between the free-surface of the upper layer, at $z = h_0$, and the interface between the two layers, at $z = h_1$, namely

$$\rho_0 g h_0 = -\rho_0 g' h_1 + \text{constant}, \tag{1.6}$$

where g' is the reduced gravity given by $g' = g(\rho_1 - \rho_0)/\rho_0 \ll g$, since typically in the ocean $\Delta\rho = \rho_1 - \rho_0 \ll \rho_0$. Note that the fact $g' \ll g$ implies that displacements in the free surface $z = h_0(x, y, t)$ are considerably smaller than the displacements in the interface $z = h_1(x, y, t)$ between the two layers. The horizontal momentum equation of the shallow layer can thus be written,

$$\frac{D\mathbf{u}}{Dt} + f\mathbf{k} \times \mathbf{u} = g'\nabla h_1, \tag{1.7}$$

where $\mathbf{u} = (u, v)$ and $h_1 = h_1(x, y)$.

Also, the fluid is incompressible, i.e.

$$\nabla \cdot \mathbf{u} = 0. \tag{1.8}$$

As the horizontal velocities are independent of z, (1.8) can be integrated with respect to z in the shallow layer, giving

$$\left[\left(\frac{\partial u}{\partial x} + \frac{\partial v}{\partial y}\right) z\right]_{z=h_1}^{z=h_0} = -\left[w(x, y, z, t)\right]_{z=h_1}^{z=h_0}, \tag{1.9}$$

As fluid does not pass through the interfaces, we have

$$w(x, y, h_0, t) = \frac{Dh_0}{Dt},\ w(x, y, h_1, t) = \frac{Dh_1}{Dt}. \tag{1.10}$$

Hence, the mass conservation equation (1.8) can be written as

$$\frac{D}{Dt}(h_0 - h_1) + \left(\frac{\partial u}{\partial x} + \frac{\partial v}{\partial y}\right)(h_0 - h_1) = 0. \tag{1.11}$$

The component form of (1.7) together with (1.11) are the reduced gravity shallow water equations,

$$\frac{\partial u}{\partial t} + u\frac{\partial u}{\partial x} + v\frac{\partial v}{\partial y} - fv = g'\frac{\partial h_1}{\partial x}, \tag{1.12}$$

$$\frac{\partial v}{\partial t} + u\frac{\partial u}{\partial x} + v\frac{\partial v}{\partial y} + fu = g'\frac{\partial h_1}{\partial y}, \tag{1.13}$$

$$\frac{1}{h}\frac{Dh}{Dt} + \left(\frac{\partial u}{\partial x} + \frac{\partial v}{\partial y}\right) = 0, \tag{1.14}$$

where

$$h = h_0 - h_1. \tag{1.15}$$

1.3 Quasigeostrophic scaling

Note that as the deviations in the free surface height are small compared to the deviation of the interface between the shallow layer and the deep layer, then $h \sim -h_1$, and let $h = D + \eta$ where, η is the deviation from the mean position of the interface.

We non-dimensionalise the reduced gravity momentum equations (1.12-1.13) using the following scales of length, time, velocity and depth.

$$x = L\hat{x},\ y = L\hat{y},\ t = T\hat{t},\ u = U\hat{u},\ v = U\hat{v},\ \eta = \mathcal{N}\hat{\eta}, \tag{1.16}$$

where scale factors, L, T, U and $\mathcal{N}$ are the scales of magnitude of the system.

After substituting (1.16) into (1.12) and (1.13), the equations are divided through by fU to give,

$$\frac{1}{fT}\frac{\partial \hat{u}}{\partial \hat{t}} + \frac{U}{fL}\left[\hat{u}\frac{\partial \hat{u}}{\partial \hat{x}} + \hat{v}\frac{\partial \hat{u}}{\partial \hat{y}}\right] - \hat{v} = -\frac{g'\mathcal{N}}{fUL}\frac{\partial \hat{\eta}}{\partial \hat{x}}, \tag{1.17}$$

$$\frac{1}{fT}\frac{\partial \hat{v}}{\partial \hat{t}} + \frac{U}{fL}\left[\hat{u}\frac{\partial \hat{v}}{\partial \hat{x}} + \hat{v}\frac{\partial \hat{v}}{\partial \hat{y}}\right] + \hat{u} = -\frac{g'\mathcal{N}}{fUL}\frac{\partial \hat{\eta}}{\partial \hat{y}}. \tag{1.18}$$

The mass continuity equation (1.14) is written

$$\eta_t + \mathbf{u}\cdot\nabla\eta + (D+\eta)\nabla\cdot\mathbf{u} = 0, \tag{1.19}$$

which on rescaling according to (1.16) gives

$$\frac{\mathcal{N}}{T}\frac{\partial \hat{\eta}}{\partial \hat{t}} + \frac{U\mathcal{N}}{L}\hat{u}\cdot\nabla\hat{\eta} + \frac{UD}{L}\left(1 + \frac{\mathcal{N}}{D}\eta\right)\hat{\nabla}\cdot\hat{\mathbf{u}} = 0, \tag{1.20}$$

which is divided through by D to give

$$\frac{\mathcal{N}}{D}\left[\frac{1}{T}\frac{\partial \hat{\eta}}{\partial \hat{t}} + \frac{U}{L}\hat{\mathbf{u}}\cdot\hat{\nabla}\hat{\eta}\right] + \frac{U}{L}\left(1 + \frac{\mathcal{N}}{D}\hat{\eta}\right)\hat{\nabla}\cdot\hat{\mathbf{u}} = 0. \tag{1.21}$$

We assume that time scales advectively, i.e. $T = L/U$, and (1.21) becomes

$$\frac{\mathcal{N}}{D}\left[\frac{\partial \hat{\eta}}{\partial \hat{t}} + \hat{\mathbf{u}}\cdot\hat{\nabla}\hat{\eta}\right] + \left(1 + \frac{\mathcal{N}}{D}\hat{\eta}\right)\hat{\nabla}\cdot\hat{\mathbf{u}} = 0. \tag{1.22}$$

We can also define the Rossby number, R_0, such that

$$R_0 = \frac{U}{fL} = \frac{1}{fT}. \tag{1.23}$$

$\mathcal{N}$ scales such that the pressure gradient term balances out the Coriolis term in the horizontal momentum equations (i.e. geostrophic balance to leading order, this being the dominant force balance in mesoscale ocean dynamics)

$$\frac{\mathcal{N}}{D} = \frac{fUL}{g'D} = \frac{U}{fL}\frac{f^2L^2}{g'D} = R_0\left(\frac{L}{L_d}\right)^2, \tag{1.24}$$

where L_d is the Rossby radius of deformation,

$$L_d = \frac{\sqrt{g'D}}{f}. \tag{1.25}$$

Let $F = (L/L_d)^2$ so (1.17-1.18) and (1.21) can be written as,

$$R_0\frac{\partial \hat{u}}{\partial \hat{t}} + R_0\left[\hat{u}\frac{\partial \hat{u}}{\partial \hat{x}} + \hat{v}\frac{\partial \hat{u}}{\partial \hat{y}}\right] - \hat{v} = -\frac{\partial \hat{\eta}}{\partial \hat{x}}, \tag{1.26}$$

$$R_0\frac{\partial \hat{v}}{\partial \hat{t}} + R_0\left[\hat{u}\frac{\partial \hat{v}}{\partial \hat{x}} + \hat{v}\frac{\partial \hat{v}}{\partial \hat{y}}\right] + \hat{u} = -\frac{\partial \hat{\eta}}{\partial \hat{y}}, \tag{1.27}$$

$$R_0F\frac{D\hat{\eta}}{D\hat{t}} + [1 + R_0F\hat{\eta}]\left[\frac{\partial \hat{u}}{\partial \hat{x}} + \frac{\partial \hat{v}}{\partial \hat{y}}\right] = 0. \tag{1.28}$$

Typically for ocean vortices, $F = \mathrm{O}(1)$ and R_0 lies in the range 0.1 to 0.3 and this is exploited by expanding $\hat{u}, \hat{v}$ and $\hat{\eta}$ as power series in R_0

$$\hat{u} = \sum_{i=0}^{\infty} R_0^i \hat{u}_i,\ \hat{v} = \sum_{i=0}^{\infty} R_0^i \hat{v}_i,\ \hat{\eta} = \sum_{i=0}^{\infty} R_0^i \hat{\eta}_i. \tag{1.29}$$

Substituting (1.29) into (1.17) and (1.28) gives the leading order momentum balanced,

$$\hat{v}_0 = \frac{\partial \hat{\eta}_0}{\partial \hat{x}},\ \ \hat{u}_0 = -\frac{\partial \hat{\eta}_0}{\partial \hat{y}}, \tag{1.30}$$

i.e. the geostrophic balance as expected.

To leading order, the mass continuity equation (1.28) gives the divergence of the first order velocity terms to be zero,

$$\frac{\partial \hat{u}_0}{\partial \hat{x}} + \frac{\partial \hat{v}_0}{\partial \hat{y}} = 0. \tag{1.31}$$

This is automatically satisfied by (1.30).

To $\mathrm{O}(R_0)$, the momentum equations give,

$$\frac{\partial \hat{u}_0}{\partial \hat{t}} + \hat{u}_0 \frac{\partial \hat{u}_0}{\partial \hat{x}} + \hat{v}_0 \frac{\partial \hat{u}_0}{\partial \hat{y}} - \hat{v}_1 = -\frac{\partial \hat{\eta}_1}{\partial \hat{x}}, \tag{1.32}$$

$$\frac{\partial \hat{v}_0}{\partial \hat{t}} + \hat{u}_0 \frac{\partial \hat{v}_0}{\partial \hat{x}} + \hat{v}_0 \frac{\partial \hat{v}_0}{\partial \hat{y}} + \hat{u}_1 = -\frac{\partial \hat{\eta}_1}{\partial \hat{y}}, \tag{1.33}$$

and by differentiating (1.32) and (1.33) with respect to $\hat{y}$ and $\hat{x}$ respectively, and taking the difference of the two, the following is obtained,

$$\frac{\partial \hat{\zeta}_0}{\partial \hat{t}} + \hat{u}_0 \frac{\partial \hat{\zeta}_0}{\partial \hat{x}} + \hat{v}_0 \frac{\partial \hat{\zeta}_0}{\partial \hat{y}} = -\left(\frac{\partial \hat{u}_1}{\partial \hat{x}} + \frac{\partial \hat{v}_1}{\partial \hat{y}} \right), \tag{1.34}$$

where the vorticity of the system is,

$$\hat{\zeta}_0 = \frac{\partial \hat{v}_0}{\partial \hat{x}} - \frac{\partial \hat{u}_0}{\partial \hat{y}_0}. \tag{1.35}$$

The $\mathrm{O}(R_0)$ of the mass continuity equation (1.28) gives,

$$F \frac{\partial \hat{\eta}_0}{\partial \hat{t}} + F \left[\hat{u}_0 \frac{\partial \hat{\eta}_0}{\partial \hat{x}} + \hat{v}_0 \frac{\partial \hat{\eta}_0}{\partial \hat{y}} \right] + \frac{\partial \hat{u}_1}{\partial \hat{x}} + \frac{\partial \hat{v}_1}{\partial \hat{y}} = 0, \tag{1.36}$$

which can then be substituted into (1.34) to give,

$$\frac{\partial \hat{\zeta}_0}{\partial \hat{t}} + \hat{u}_0 \frac{\partial \hat{\zeta}_0}{\partial \hat{x}} + \hat{v}_0 \frac{\partial \hat{\zeta}_0}{\partial \hat{y}} = F \left[\frac{\partial \hat{\eta}_0}{\partial \hat{t}} + \hat{u}_0 \frac{\partial \hat{\eta}_0}{\partial \hat{x}} + \hat{v}_0 \frac{\partial \hat{\eta}_0}{\partial \hat{y}} \right], \tag{1.37}$$

which can be written in terms of the horizontal operator, D/Dt, as

$$\frac{D}{D\hat{t}} \left[\hat{\zeta}_0 - F \hat{\eta}_0 \right] = 0. \tag{1.38}$$

The leading order velocity field, $\mathbf{u} = \hat{u}_0 \hat{\mathbf{i}} + \hat{v}_0 \hat{\mathbf{j}}$ can be derived from a streamfunction, ψ, such that,

$$\mathbf{u} = \hat{\mathbf{k}} \times \nabla \psi_0, \tag{1.39}$$

where $\hat{\mathbf{k}}$ is the unit vector in the vertical direction. From (1.30) and (1.39)

$$\hat{\psi}_0 = \hat{\eta}_0,\ \hat{\nabla}^2\hat{\psi}_0 = \hat{\zeta}_0. \tag{1.40}$$

Now, (1.38) can be expressed in terms of the streamfunction as

$$\frac{D}{D\hat{t}}\left[\hat{\nabla}^2\hat{\psi}_0 - F\hat{\psi}_0\right] = 0. \tag{1.41}$$

On re-dimensionalisation (1.41) becomes

$$\frac{D}{Dt}\left[\nabla^2\psi - \frac{1}{L_d^2}\psi\right] = 0, \tag{1.42}$$

and for convenience below we define the quantity q,

$$q = \nabla^2\psi - \frac{1}{L_d^2}\psi, \tag{1.43}$$

to be the reduced gravity quasigeostrophic potential vorticity and (1.42) expresses its conservation.

For the vortical motion studied in this thesis we will examine anomalies of quasigeostrophic potential vorticity (1.43). One immediate observation of (1.43) is noted: as $L_d \to \infty$ (i.e. infinite deformation radius or rigid-lid case), $q \to \nabla^2\psi$, i.e. the 'usual' vorticity in the two dimensional Euler equations.

1.3.1 The quasigeostrophic point vortex

The quasigeostrophic point vortex model is invaluable when considering theoretical two dimensional vortex dynamics. The point vortex is the result of a limiting process by which the vorticity distribution $q(x, y, t)$ is shrunk to a point. There is therefore infinite vorticity at a single point in the plane. Formally, the streamfunction for a quasigeostrophic point vortex of circulation κ is obtained from the inhomogeneous partial differential equation

$$q(x, y) = \nabla^2 \psi - \frac{1}{L_d^2}\psi = \kappa\delta(x - x_v)\delta(y - yv), \tag{1.44}$$

where (x_v, y_v) is the location of the vortex and $\delta(x - x_v)$ is the delta function.

In polar coordinates, $(\mathbf{r} = r\hat{\mathbf{r}})$, (1.44) may be re-written as,

$$\frac{\partial^2 \psi}{\partial r^2} + \frac{1}{r}\frac{\partial \psi}{\partial r} - \frac{1}{L_d^2}\psi = \kappa\delta(\mathbf{r} - \mathbf{r}_v), \tag{1.45}$$

where $\mathbf{r}_v$ is the location of the vortex in polar coordinates. Assuming, $\mathbf{r}_v = 0$, the streamfunction can be the written as the linear combination of modified Bessel functions i.e.

$$\psi(r) = \kappa \left(AK_0(r/L_d) + BI_0(r/L_d)\right). \tag{1.46}$$

For an isolated vortex we demand, $\psi(r) \to 0$ as $r \to \infty$, $B = 0$ since $I_0(r/L_d) \to \infty$ as $r \to \infty$.

We are left to calculate the constant A in the streamfunction,

$$\psi(r) = A\kappa K_0(r/L_d), \tag{1.47}$$

where,

$$\iint_{allspace} \left(\frac{\partial^2 \psi}{\partial r^2} + \frac{1}{r}\frac{\partial \psi}{\partial r} - \frac{1}{L_d^2}\psi\right) \mathrm{d}A = \kappa. \tag{1.48}$$

Here κ is the circulation associated with the point vortex.

Evaluating the integral in polar coordinates gives,

$$\int_0^{2\pi}\int_0^{\infty} \left(\frac{\partial^2 \psi}{\partial r^2} + \frac{1}{r}\frac{\partial \psi}{\partial r} - \frac{1}{L_d^2}\psi\right) r\,\mathrm{d}r\,\mathrm{d}\theta = \kappa, \tag{1.49}$$

or

$$\int_0^{\infty} \left(\frac{\partial^2 \psi}{\partial r^2} + \frac{1}{r}\frac{\partial \psi}{\partial r} - \frac{1}{L_d^2}\psi\right) r\,\mathrm{d}r = \frac{\kappa}{2\pi}, \tag{1.50}$$

as ψ is axisymmetric. Now $\psi(r)$ satisfies Helmholtz's equation, except possibly, near $r = 0$. Thus

$$\int_0^\delta \left(\frac{\partial^2 \psi}{\partial r^2} + \frac{1}{r}\frac{\partial \psi}{\partial r} - \frac{1}{L_d^2}\psi \right) r \,\mathrm{d}r = \frac{\kappa}{2\pi}, \tag{1.51}$$

where $\delta \ll 1$. Note from (1.47) $\psi \sim -A\kappa \ln r$ for $0 < r \leq \delta$, hence

$$\int_0^\delta r\psi \,\mathrm{d}r \to 0 \text{ as } \delta \to 0, \tag{1.52}$$

thus the third term in the integrand of (1.51) vanishes as $\delta \to 0$. Now replace $\psi = -A\kappa \ln r$ by $\psi = -A\kappa \ln(r + \epsilon)$ in the left hand side . Hence

$$\begin{aligned} \int_0^\delta (\psi_{rr} + \frac{1}{r}\psi_r) r \,\mathrm{d}r &= -A\kappa \int_0^\delta \left[-\frac{1}{(r+\epsilon)^2} + \frac{1}{r(r+\epsilon)} \right] r \,\mathrm{d}r, \\ &= -A\kappa \text{ as } \epsilon \to 0. \end{aligned} \tag{1.53}$$

Thus (1.50) gives $A = -1/2\pi$ and

$$\psi(r) = -\frac{\kappa}{2\pi} K_0(r/L_d). \tag{1.54}$$

In Cartesian coordinates, (1.54) can be written as,

$$\psi(x, y) = -\frac{\kappa}{2\pi} K_0 \left(\sqrt{(x - x_v)^2 + (y - y_v)^2}/L_d \right), \tag{1.55}$$

which is the point vortex solution of the quasigeostrophic equation.

The velocity field in polar coordinates is $\mathbf{u} = u_r \hat{\mathbf{r}} + u_\theta \hat{\boldsymbol{\theta}}$. From (1.55), these can be written as

$$u_r = 0,\ u_\theta = -\frac{\kappa}{2\pi L_d} K_1(r/L_d), \tag{1.56}$$

which represents an axisymmetric 'swirling' velocity u_θ about the vortex centre.

Importantly, as $r \to \infty$, u_θ decays exponentially, since $K_1(x) \sim \exp(-x)/\sqrt{x}$ as $x \to \infty$. In contrast, for the rigid-lid case ($L_d \to \infty$), the velocity field can be written as

$$u_r = 0,\, u_\theta = -\frac{\kappa}{2\pi r}, \tag{1.57}$$

and decays algebraically as $r \to \infty$. The different far-field behaviour of an Euler (i.e. rigid-lid) vortex compared to a quasigeostrophic vortex is central to interpreting many of the results of this research.

1.4 Thesis outline

This research is split up into two main problems, both having the common objective of determining the effects of the Rossby radius of deformation on vortex motion. In both problems, the quasigeostrophic potential vorticity equation is non-dimensionalised using intrinsic length scales related to the specific geometry of the problems.

The next three chapters consider the motion of a vortex near a gap in an infinitely long wall, i.e. two semi-infinite barriers separated by a finite gap. The key parameter is a, which, in this context, is the ratio of the Rossby radius of deformation to the width of the gap (see equation (2.3)). A particular focus is the trajectory taken by the vortex. A fundamental question is when does the vortex pass through the gap and when does it leap across?

In chapter 2, a is taken to be large and the vortex model used is that of a point vortex. For the rigid-lid case ($a \to \infty$) the complete solution has been previously found analytically using the Kirchoff-Routh path function. A numerical solution is found here for large, but finite, a by using a vortex sheet to model the effects of the gap. As a is large, the explicit rigid-lid solution is used as a basis to iteratively solve for finite a. When the vortex passes through the gap, there is a singularity present at the gap causing the method to fail. Hence a conjugate method is required. This method is outlined in Appendix A and replaces the barriers with two semi-infinite vortex sheets. The flow outside the vortical structures is again forced to be irrotational and solved numerically using conformal mapping techniques. This can again be applied iteratively for finite a.

For small a however, as the initial guess of the rigid-lid solution is no longer a good approximation, the method fails. Hence a new method is developed in chapter 3 for small a. Here, an integral equation is formulated whose solution determines the velocity field everywhere in the fluid enabling the vortex trajectory to be computed. The effect of varying the deformation radius on the vortex trajectories is investigated. The effect of background flows is also incorporated in this method by imposing a constant value of the streamfunction along each of the semi-infinite barriers. A variety of different vortex trajectories are found, depending on the nature and strength of the background flow.

In chapter 4, the point vortex is replaced by a region of finite area containing uniform vorticity – a vortex patch. Contour dynamics and contour surgery in combination with the integral method of chapter 3 are utilised to calculate the trajectories and behaviour of the vortex patches. For large a, it is noted that the velocity of circular patches scale with the area of the patch. However, for small a, a new method of normalisation is developed and implies that the value of a also influences the velocity of patch motion.

In chapter 5, the second problem of the motion of two steadily translating (antisymmetric) counter-rotating vortices is examined. This is equivalent to the motion of a vortex patch near a wall and generalises classic work on the Euler equations to the case of arbitrary deformation radius. The parameter a is now the ratio of Rossby radius of deformation and a measure of the distance of the patch from the line of symmetry or wall (see equation (5.8)). A relaxation method used in conjunction with contour dynamics is used to calculate the shape and the translational velocities of the patches. Using the normalisation technique introduced in chapter 4, the velocities of vortex patch pairs are compared to point vortex pairs located at the centroids of the vortex patches. A uniform flow, parallel to the wall that satisfies the quasigeostrophic vorticity equation is used to calculate a new family of solutions of vortex patches. Depending on the strength and direction of the background flow and the value of a, 'elliptical' vortex patches are generated. By adjusting the relaxation algorithm, the strength of a background flow to bring a vortex pair to rest is also calculated. Finally, conclusions and ideas for future work are presented in chapter 6.

Chapter 2

Vortex motion near a gap in a wall: Large Rossby radius case

2.1 Introduction

Long-lived eddies play a significant role in the transport and mixing of ocean properties such as momentum, heat and salt. Meddies (i.e. Mediterranean salt lenses typically measuring 50 km in diameter and several hundred metres in depth) carry anomalously salty water from the Mediterranean to the North Atlantic and have been tracked for up to several years (see Richardson et al. 2000). Such long-lived vortices will inevitably encounter topography in the form of mid-ocean ridges, coastlines and seamounts. It is of interest to determine how the interaction of vortices with such topographic features affects their transport characteristics.

Simmons and Nof (2002) investigated vortex interactions with gap-like geometries in relation to the equatorial currents and eddies in the western Atlantic and showed how fluid can be transported through a gap by eddies. High resolution numerical experiments have recently been carried out by Kirchner et al. (2010) examining the structure, propagation pathways and interactions of North Brazilian current rings with the narrow pathways between islands of the Lesser Antilles. The influence of the Kuroshio Current on westward propagating eddies near the Luzon Strait has been modelled by Sheu et al. (2010) using the Princeton Ocean Model. Laboratory experiments have also been conducted on a single self propagating vortex near two islands by Cenedese et al. (2005) showing that the interaction depends on the size of the vortex and the distance between the islands.

The abyssal ocean contains many disjointed ridges, punctuated by gaps. A variety of oceanic processes have been considered in the literature such as flows of the stratified abyssal ocean in the presence of a partially blocked meridional barrier by Pedlosky (1994) and the exchange flow between large-scale ocean basins through narrow gaps by Nof (1994). Pratt and Spall (2003) used a ‘porous’ barrier theory to model numerous gaps in mid-ocean ridges.

Idealised models which assume two dimensional flow of an inviscid fluid have been used to construct the Hamiltonian for a single point vortex near a gap, in an infinitely long and infinitesimally thin barrier in the rigid-lid case (i.e. infinite Rossby radius) by Johnson and McDonald (2004). The main result from their work showed that vortices that start far upstream of the gap at greater than half the gap width from the barrier leap across the gap. Vortices starting closer to the barrier pass through the gap. Subsequently, vortex motion near barriers with two gaps was studied by Johnson and McDonald (2005) and later extended to an arbitrary number of gaps by Crowdy and Marshall (2006).

Duran-Matute and Velasco Fuentes (2008) found analytical trajectories for a barotropic line vortex near a gap in a wall within a channel in the presence of a uniform current passing along the channel. Furthermore, numerical trajectories of finite-area patches were computed and compared to the results found through laboratory experiments conducted within a homogeneous rotating fluid, showing good agreement for vortices that pass through the gap completely, i.e. without splitting. These models are mathematically equivalent to single-layer quasigeostrophic dynamics in the limit of infinite Rossby radius of deformation (i.e. the rigid-lid limit). While these exact solutions are interesting and useful, in an oceanographic context it is natural to consider the more realistic case of having a finite Rossby radius of deformation.

The present chapter aims to generalise the work of Johnson and McDonald (2004) to include a finite, but large, Rossby radius for the point vortex. The key non-dimensional parameter is a, the ratio of the Rossby radius of deformation to the half-width of the gap. Quasigeostrophic dynamics in a single layer with reduced gravity is used to derive an integral equation whose solution gives the velocity field at the vortex, enabling its trajectory to be computed. For finite a, the integral equation must be solved numerically, unlike the case for the rigid-lid limit where complex variable methods can be employed (as shown by Johnson and McDonald (2004)).

An integral equation is found using Green's function techniques and solved iteratively. However, when the vortex passes close to the gap, numerical inaccuracies are encountered and a conjugate method is formulated, whereby the effects of the two semi-infinite barriers on either side of the gap are modelled by vortex sheets whose strength is determined by solving another integral equation. The two approaches are used in conjunction to calculate the velocity field everywhere. The analytical solution found by Johnson and McDonald (2004) is used to compare the solution for infinite a.

In Section 2.2, the vortex-barrier interaction problem is described. In Section 2.3 the integral equation is derived for the vortex sheet over the gap. The iterative solution of the integral equation is also detailed, including the de-singularisation of the integral equation (which is hyper-singular). In Section 2.4, the integral equation for the conjugate method is derived. The numerical solution for the rigid-lid case ($a \to \infty$) is also described, which is used to solve the finite a case iteratively.

The results for point vortices are discussed in Section 2.5 and compared to the analytical solutions found by Johnson and McDonald (2004). Conclusions are presented in Section 2.6 where the need for a new method for capable of handling smaller a is highlighted.

2.2 Point vortex near a gap in a wall

A single layer of reduced gravity fluid in a flat bottomed ocean of depth H is considered. In the quasigeostrophic limit, the potential vorticity q is conserved where,

$$q = \nabla^2\psi - \frac{1}{L_d^2}\psi. \tag{2.1}$$

Here ψ is the geostrophic streamfunction from which the velocity field can be recovered ($d\mathbf{x}/dt = \mathbf{k} \times \nabla\psi$), f is the constant Coriolis parameter and g' is the reduced gravity. The length scale, $L_d = \sqrt{g'H}/f$, is the Rossby radius of deformation. As $L_d \to \infty$, Eulerian dynamics is recovered.

The vortex is located near a gap in an infinitesimally thin, infinitely long wall. This is equivalent to two semi-infinite straight barriers on either side of a gap of width $2W$. The task is to compute the trajectory of the vortex with circulation κ and determine conditions when the vortex passes through this gap. A schematic of the system is shown in Fig. 2.1. The barriers are aligned with the $x-$axis and the origin of the (x, y) coordinate system coincides with the midpoint of the gap.

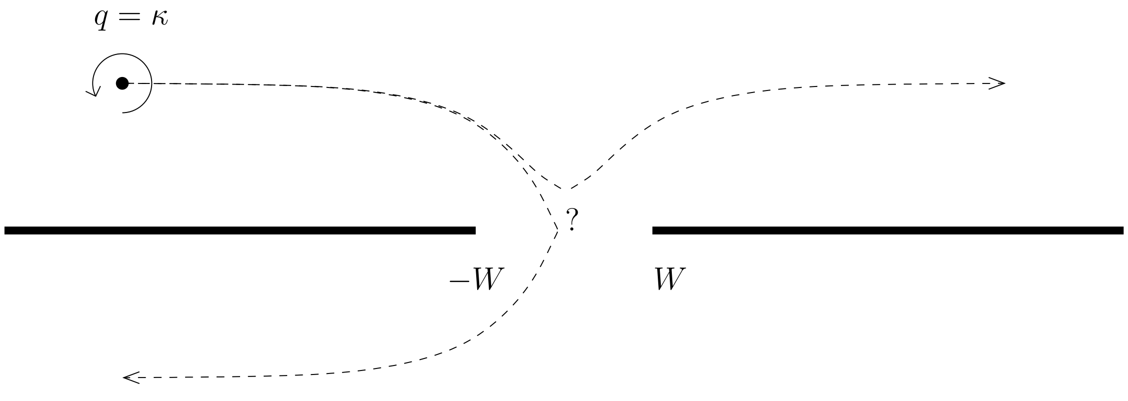

Figure 2.1: Possible trajectories of a single vortex of circulation κ near a gap in a wall.

With ψ scaled on $|\kappa|$, the potential vorticity q scales like $|\kappa|W^{-2}$, and for horizontal scale W (i.e. half the gap width). The non-dimensional potential vorticity q' can be written as

$$q' = \nabla^2\psi' - \frac{1}{a^2}\psi', \tag{2.2}$$

where

$$a = \sqrt{gD}/fW \tag{2.3}$$

measures the ratio of the deformation radius to the half gap width W. Henceforth, the dashes for non-dimensional quantities are omitted.

The equation for a quasigeostrophic point vortex (see chapter 1) is,

$$\nabla^2\psi_v - \frac{1}{a^2}\psi_v = \frac{\kappa}{2\pi}\delta(x - x_v)\delta(y - y_v), \tag{2.4}$$

where (x_v, y_v) is the location of the point vortex with strength κ. Everywhere else in the fluid, the Helmholtz equation (see chapter 1) is satisfied, i.e.,

$$\nabla^2\psi - \frac{1}{a^2}\psi = 0. \tag{2.5}$$

By assuming the presence of a vortex sheet over the gap, so that (2.5) is satisfied, allows the velocity induced at the point vortex to be calculated.

2.3 Vortex sheet over the gap

Consider the motion of an incompressible fluid in a domain $\mathcal{D}$ which can be decomposed into subdomains $\mathcal{D}_{1,2}$ separated by the boundary $\mathcal{G}$ (see Fig. 2.2).

$\mathcal{G}$ is the single "open" gap which allows the passage of fluid between subdomains. Let the streamfunction induced by vortices in $\mathcal{D}_1$ be ψ_1. There is no normal flow through the boundary, hence $\psi_1 = 0$ on the boundary of $\mathcal{D}_1$. Similarly for $\mathcal{D}_2$, the streamfunction is ψ_2 will also have no normal flow through the boundary, hence

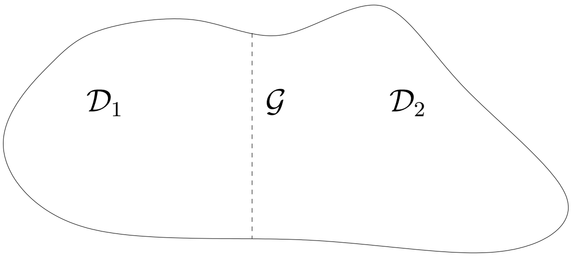

Figure 2.2: Subdomains $\mathcal{D}_{1,2}$ separated by gap $\mathcal{G}$.

$\psi_2 = 0$ on the boundary of $\mathcal{D}_2$. Let Ψ be the total streamfunction such that on the boundary of the domain $\mathcal{D} = \mathcal{D}_1 \cup \mathcal{D}_2$, $\Psi = 0$ and

$$\Psi = \psi_1 + \psi \text{ in } \mathcal{D}_1 \tag{2.6}$$

$$\Psi = \psi_2 + \psi \text{ in } \mathcal{D}_2. \tag{2.7}$$

Now Ψ is continuous across the gap and $\psi_{1,2}$ vanish there, ψ must also be continuous. The normal derivative $\partial\Psi/\partial n$ must also be continuous across $\mathcal{G}$, and

$$\left[\frac{\partial}{\partial n}(\Psi - \psi)\right] = \frac{\partial \psi_2}{\partial n} - \frac{\partial \psi_1}{\partial n} \tag{2.8}$$

where $[\cdot]$ denotes the jump in the enclosed quantity moving from $\mathcal{D}_1$ to $\mathcal{D}_2$ across $\mathcal{G}$. Hence,

$$\left[\frac{\partial \psi}{\partial n}\right] = -\frac{\partial \psi_2}{\partial n} + \frac{\partial \psi_1}{\partial n} = u_2 - u_1 \tag{2.9}$$

where u_2 is the tangential velocity induced along $\mathcal{G}$ by vortices in $\mathcal{D}_2$ with $\mathcal{G}$ being a rigid wall and u_1 is the equivalent tangential velocity for the vortices in $\mathcal{D}_1$. Thus (2.9) effectively gives the strength of the vortex sheet whose streamfunction is ψ.

In the rigid-lid limit ($a \to \infty$), advantage can be taken of the known point vortex behaviour of the Hamiltonian under conformal mapping (see Saffman (1992)). By mapping the single gap geometry to a half-space, Johnson and McDonald (2004) were able to obtain an explicit expression for the vortex Hamiltonian in the single-gap geometry. This in turn enabled the vortex trajectories to be determined exactly.

For a finite a, there is no such rule for the behaviour of the Hamiltonian under conformal mapping. Hence, an integral equation method is utilised, where the effect of the vortex sheet is computed.

2.3.1 Integral equation: Vortex sheet over the gap

The velocity field outside the vortex sheet has streamfunction ψ which satisfies

$$\begin{aligned} \nabla^2\psi - \frac{1}{a^2}\psi &= 0, && (2.10)\\ \frac{\partial\psi}{\partial y}(x,0) &= f(x) \text{ for all } |x|<1, y=0, && (2.11)\\ \psi(x,0) &= \Lambda(x) \text{ for all } |x|<1, y=0, && (2.12)\\ \psi(x,0) &= 0 \text{ for all } |x|>1, y=0. && (2.13) \end{aligned}$$

Note that $f(x)$ (the tangential velocity across the gap owing to the presence of vortices) is known (i.e. it is given by (2.9)), but $\Lambda(x)$ is unknown.

Let

$$\begin{aligned} G_a(x,y,x_0,y_0) = &-\frac{1}{2\pi}K_0\left(\sqrt{(x-x_0)^2+(y-y_0)^2}/a\right) \\ &+\frac{1}{2\pi}K_0\left(\sqrt{(x-x_0)^2+(y+y_0)^2}/a\right), \end{aligned} \tag{2.14}$$

where $G_a(x,y,x_0,y_0)$ is a Green's function satisfying

$$\begin{aligned} \nabla^2 G_a - \frac{1}{a^2}G_a &= \delta(x-x_0)\delta(y-y_0), && (2.15)\\ G_a &= 0 \text{ on the } x \text{ axis}, && (2.16) \end{aligned}$$

and K_0 is the modified Bessel's function of the second kind of order zero.

Now, using Green's Theorem

$$\int\int_S \left(\psi\nabla^2 G_a - G_a\nabla^2\psi\right)\,\mathrm{d}x\,\mathrm{d}y = \int_{-\infty}^{\infty}\left(\psi\frac{\partial G_a}{\partial y} - G_a\frac{\partial\psi}{\partial y}\right)\,\mathrm{d}x, \tag{2.17}$$

where S denotes the entire upper-half plane, $y \geq 0$ above the $x-$axis.

Using (2.10) and (2.15), the left hand side of (2.17) may be simplified:

$$\int\int_S \left(\psi\nabla^2 G_a - G_a\nabla^2\psi\right)\,\mathrm{d}x\,\mathrm{d}y = \psi(x_0, y_0). \tag{2.18}$$

As G_a vanishes on the x-axis, the second term on the right hand side in (2.17) must also vanish:

$$\oint_b \frac{\partial\psi}{\partial y}(x) G_a(x, 0, x_0, y_0)\,\mathrm{d}x = 0. \tag{2.19}$$

As the streamfunction derivative with respect to y vanishes along the wall, the integral over the x-axis reduces to an integral over the gap width. Hence, using (2.18), (2.19) and (2.12) an equation for the streamfunction is derived:

$$\psi(x_0, y_0) = \int_{-1}^{1} \Lambda(x)\frac{\partial G_a}{\partial y}(x, 0, x_0, y_0)\,\mathrm{d}x. \tag{2.20}$$

On differentiation of (2.20) with respect to y_0 and x_0 yields

$$u(x_0, y_0) = -\int_{-1}^{1} \Lambda(x)\frac{\partial^2 G_a}{\partial y\partial y_0}(x, 0, x_0, y_0)\,\mathrm{d}x, \tag{2.21}$$

$$v(x_0, y_0) = \int_{-1}^{1} \Lambda(x)\frac{\partial^2 G_a}{\partial y\partial x_0}(x, 0, x_0, y_0)\,\mathrm{d}x. \tag{2.22}$$

Hence, given $\Lambda(x)$ the velocity field induced by the vortex sheet can be computed everywhere, and in particular at the vortex itself enabling the vortex trajectory to be obtained. Hence, the task is to find $\Lambda(x)$.

If we now differentiate (2.20) with respect to y_0 and set $y_0 = 0$ we have using (2.11) for $-1 < x_0 < 1$,

$$f(x_0) = \int_{-1}^{1} \Lambda(x)\frac{\partial^2 G_a}{\partial y\partial y_0}(x, 0, x_0, 0)\,\mathrm{d}x. \tag{2.23}$$

Since $f(x_0)$ is known, (2.23) is an integral equation for the unknown $\Lambda(x)$.

2.3.2 Solution of the integral equation: Gap method

Let $\mathcal{L}_a(x-x_0) = \frac{\partial^2}{\partial y \partial y_0} G_a(x, 0, x_0, 0)$. Hence, from (2.14)

$$\mathcal{L}_a(x-x_0) = -\frac{K_1\left(|x-x_0|/a\right)}{\pi |x-x_0| a}. \tag{2.24}$$

Now (2.23) is a hypersingular integral equation, i.e. the integrand (in this case equation (2.24)), has a singularity which goes to infinity like $(x-x_0)^{-2}$ as $x \to x_0$, since $K_1(|x-x_0|/a)$ behaves like $a/|x-x_0|^{-1}$ as $x \to x_0$. A simple 'de-singularisation' method of adding and subtracting another hypersingular term with the same behaviour is used here. Consider

$$G_\infty = \frac{1}{2\pi} \log \left(\sqrt{\frac{(x-x_0)^2 + (y-y_0)^2}{(x-x_0)^2 + (y+y_0)^2}} \right). \tag{2.25}$$

which is the Green's function for (2.15-2.16) in the rigid-lid (i.e. $a \to \infty$) case. Hence

$$\mathcal{L}_\infty(x-x_0) = \frac{\partial^2}{\partial y \partial y_0} G_\infty(x, 0, x_0, 0) = -\frac{1}{\pi (x-x_0)^2}, \tag{2.26}$$

which has the same singular behaviour of (2.24) as $x \to x_0$. Now, (2.23) can be written as

$$f(x_0) = -\int_{-1}^{1} \Lambda(x)(\mathcal{L}_\infty(x-x_0) - \mathcal{L}_a(x-x_0))\,\mathrm{d}x + \int_{-1}^{1} \Lambda(x)\mathcal{L}_\infty(x-x_0)\,\mathrm{d}x \tag{2.27}$$

or

$$\int_{-1}^{1} \Lambda(x)\mathcal{L}_\infty(x-x_0)\,\mathrm{d}x = f(x_0) + \int_{-1}^{1} \Lambda(x)(\mathcal{L}_\infty(x-x_0) - \mathcal{L}_a(x-x_0))\,\mathrm{d}x, \tag{2.28}$$

where the integral term on the right hand side is non-singular.

Equation (2.28) can be solved by an iterative scheme:

$$\begin{aligned}\int_{-1}^{1} \Lambda^{(n+1)}(x)\mathcal{L}_\infty(x-x_0)\,\mathrm{d}x &= f(x_0) + \int_{-1}^{1} \Lambda^{(n)}(x)(\mathcal{L}_\infty(x-x_0) - \mathcal{L}_a(x-x_0))\,\mathrm{d}x \\ &= f^{(n)}(x_0), \end{aligned} \tag{2.29}$$

where terms with superscripts (n) are known and used to calculate the terms with superscripts $(n+1)$. All the integrations on the right hand side can be calculated numerically as the hypersingularities are subtracted from each other. There is a logarithmic singularity in $\mathcal{L}_a(x-x_0)$ at $x = x_0$ as well, which is treated specially by integrating about the singularity using a variation of Simpson's rule, which is derived and detailed in the next Section 2.3.3.

It remains to solve

$$\int_{-1}^{1} \Lambda^{(n+1)}(x)\mathcal{L}_\infty(x-x_0)\,\mathrm{d}x = f^{(n)}(x_0). \tag{2.30}$$

This solution is known from the rigid-lid problem where $f^{(n)}(x_0)$ is half the vortex sheet strength and $\Lambda^{(n+1)}(x)$ is the streamfunction along the gap. Johnson and McDonald (2004) have a direct method of computing this solution using Fourier transforms. In the present case the solution is

$$\Lambda^{(n+1)}(x) = \Im \sum_{k=1}^{\infty} \frac{b_k}{2k}\zeta^k \tag{2.31}$$

where $\zeta = x + \mathrm{i}\sqrt{(1-x^2)}$ and b_k are the real and equal sine coefficients of the Fourier series of $f^{(n)}(x_0)$ for $-1 \leq x_0 \leq 1$. After each iteration, the value of $\Lambda^{(n+1)}(x)$ is substituted into (2.29) to calculate $f^{(n+1)}(x_0)$, which is used to compute the next iteration of $\Lambda^{(n+2)}(x)$. The iterations continue until there is a maximum difference of 10^{-6} between successive iterated values of $\Lambda^{(n)}(x)$. Then $\Lambda(x)$ can be substituted into (2.21) and (2.22) to compute the velocity field everywhere. The integrand still has a logarithmic singularity and this is dealt with in the next subsection.

2.3.3 Integrating over the logarithmic singularity

The logarithmic singularity is present in the integrand term of equation (2.30)

$$\Lambda(x)\left[\mathcal{L}_\infty(x-x_1)-\mathcal{L}_a(x-x_1)\right], \tag{2.32}$$

at $x = x_1$ owing to the term $\mathcal{L}_a(x-x_1)$. However, the logarithmic function is analytically integrable over the singularity and its contribution to $f^n(x_1)$ in (2.30) can be calculated by interpolating the non-logarithmic part of the integrand as a quadratic polynomial and then integrating analytically.

Over the logarithmic singularity, the integral required is

$$\int_{x_1-h}^{x_1+h} \Lambda(x)\left[\mathcal{L}_\infty(x-x_1)-\mathcal{L}_a(x-x_1)\right]\,\mathrm{d}x, \tag{2.33}$$

where x_1 denotes the location of the singularity, and $h > 0$ is some sufficiently small number.

Now, the leading order behaviour of the integrand can be represented as the product of a polynomial and the logarithmic function $\ln(x-x_1)$,

$$\Lambda(x)\left[\mathcal{L}_\infty(x-x_1)-\mathcal{L}_a(x-x_1)\right] = (a_0+a_1x+a_2x^2)\ln(x-x_1), \tag{2.34}$$

where the polynomial, $a_0+a_1x+a_2x^2$, can be calculated by quadratic interpolation using the coefficients of the logarithmic function at three points, x_1-h, x_1 and x_1+h. Let the points on either side of the singularity be

$$x_0 = x_1 - h, \tag{2.35}$$

$$x_2 = x_1 + h. \tag{2.36}$$

The logarithmic singularity is solely present in the difference of the kernel functions i.e.

$$D(x - x_1) = \mathcal{L}_\infty(x - x_1) - \mathcal{L}_a(x - x_1). \tag{2.37}$$

The function, $D(x - x_1)$ is expanded about $x = x_1$ up to $\mathrm{O}((x - x_1)^3)$,

$$\begin{aligned} D(x - x_1) \simeq & \frac{-1 + 2\gamma - 2\ln(2a) + 2\ln(x - x_1)}{4\pi a^2} \\ & + \frac{-5 + 4\gamma - 4\ln(2a) + 4\ln(x - x_1)}{64\pi a^4}(x - x_1)^2 + \mathrm{O}((x - x_0)^3), \end{aligned} \tag{2.38}$$

where γ is the Euler-Mascheroni constant:

$$\gamma = \lim_{n\to\infty}\left(\sum_{k=1}^{n}\frac{1}{k} - \ln n\right). \tag{2.39}$$

Hence, the coefficients of the leading order logarithmic term, $\ln(x - x_1)$, can be calculated at the points, $x_{0,1,2}$ using (2.38),

$$c_0 = \Lambda(x_0)\left(\frac{1}{2\pi a^2} + \frac{(x_0 - x_1)^2}{16\pi a^4}\right), \tag{2.40}$$

$$c_1 = \frac{\Lambda(x_1)}{2\pi a^2}, \tag{2.41}$$

$$c_2 = \Lambda(x_2)\left(\frac{1}{2\pi a^2} + \frac{(x_2 - x_1)^2}{16\pi a^4}\right). \tag{2.42}$$

Using the polynomial interpolation in (2.34) , the quadratic coefficients $a_{0,1,2}$ can be calculated numerically using the values of the coefficients $c_{0,1,2}$,

$$a_0 = c_0, \tag{2.43}$$

$$a_1 = \frac{c_0 - c_2}{2h}, \tag{2.44}$$

$$a_2 = \frac{c_0 - 2c_1 + c_2}{2h^2}. \tag{2.45}$$

Analytically, the product of a polynomial and the logarithmic function can be integrated. Hence the integral can be expressed solely in terms of h, the difference between successive points:

$$\int_{x_0}^{x_2} (a_0 + a_1 x + a_2 x^2) \ln(x - x_1)\, \mathrm{d}x = -\, 2h(a_0 + \frac{a_2}{9}h^2 + a_1 x_1 + a_2 x_1^2) \qquad (2.46)$$
$$+ 2h \ln(h)(a_0 + \frac{a_2 h^2}{3} + a_1 x_1 + a_2 x_1^2).$$

Now all integrations on the right hand side of (2.29) can be solved numerically to compute the trajectory of the point vortex. However, when the vortex is close to the gap i.e. $y_0 \to 0$, the integrals to determine the velocities in (2.21) and (2.22) have singularities (again owing to the hypersingular behaviour of $\partial^2 G_a/\partial y \partial y_0$ as $y_0 \to 0$). Hence, a conjugate method is required when the vortex passes through the gap. This is done by assuming the vortex sheets are over the barriers and is discussed in Section 2.4.

2.4 Vortex sheets over the barriers

In this section an alternative method of solution is proposed, in which vortex sheets are aligned with the barriers instead of along the gap. This, as we shall see, has the advantage of remaining accurate when the vortex is close to the gap.

2.4.1 Integral equation: Vortex sheet over the barriers

Using the same Green's function techniques as in Section 2.3.1, an integral equation is derived, where the integration is along the barriers. Effectively, the presence of the barriers is represented by vortex sheets along the two semi-infinite barriers with strength such that the total normal flow across the barriers vanishes. Let $g(x) = \Psi(x, 0)$ be the streamfunction evaluated on the semi-infinite barriers, i.e.

$$g(x) = \Psi(x, 0),\ |x| > 1. \qquad (2.47)$$

For a single point vortex at (x_v, y_v), $\Psi = \Psi_{PV}$ and we have

$$g(x) = \Psi_{PV}(x, 0, x_v, y_v),\ |x| > 1. \tag{2.48}$$

Consider $\psi(x, y)$, as introduced in (2.5), the flow induced by the presence of the point vortex. We need to solve the boundary value problem

$$\nabla^2\psi - \frac{1}{a^2}\psi = 0, \tag{2.49}$$

$$\psi(x, 0) = -g(x),\ |x| > 1, \tag{2.50}$$

$$\text{where } \psi(r) \to 0 \text{ as } r \to \infty,\ \text{ where } r = \sqrt{x^2 + y^2}, \tag{2.51}$$

$$\text{and } g(x) \to 0 \text{ as } |x| \to \infty. \tag{2.52}$$

Note condition (2.50) implies that the barriers are streamlines, i.e. $\psi + \Psi_{PV} = 0$ on $|x > 1|$ and so the normal velocity vanishes on the barriers.

Let

$$H_a(x, y, x_0, y_0) = -\frac{1}{2\pi}K_0\left(\sqrt{(x - x_0)^2 + (y - y_0)^2}/a\right), \tag{2.53}$$

be the infinite space Green's function for the Helmholtz equation (2.49). Then,

$$\nabla^2 H_a - \frac{1}{a^2}H_a = \delta(x - x_0)\delta(y - y_0). \tag{2.54}$$

Now, integrating over all space D (see Fig. 2.3) and using (2.51), Green's theorem gives

$$\iint_D \left(\psi\nabla^2 H_a - H_a\nabla^2\psi\right)\,\mathrm{d}x\,\mathrm{d}y = \int_b \left(\psi\frac{\partial H_a}{\partial y} - H_a\frac{\partial \psi}{\partial y}\right)\,\mathrm{d}x, \tag{2.55}$$

where (2.51) has been used and the right hand side is the line integral around b the four surfaces of the semi-infinite barriers, i.e. extending from $(-\infty, -1]$ and $[1, \infty)$ above the barriers ($y = 0^+$) and $(-\infty, -1]$ and $[1, \infty)$ below the barriers ($y = 0^-$).

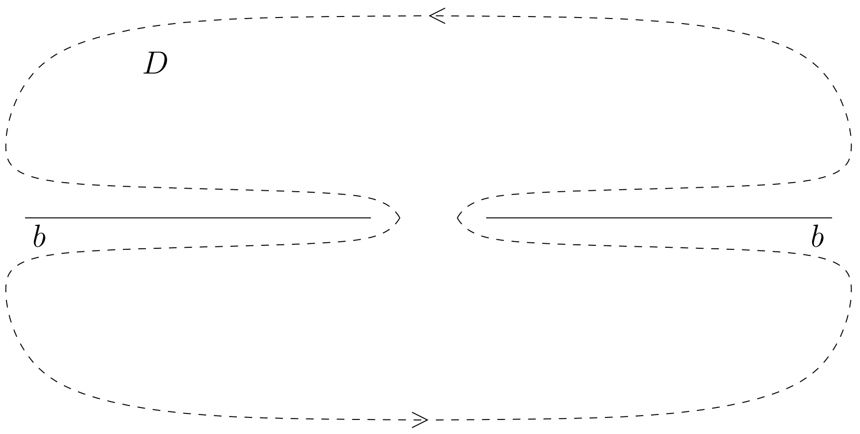

Figure 2.3: The integral over all space, D can be represented as an integral around the boundary of D as shown by the dashed lines. The arrow indicates the direction around which the boundary integral is taken.

Since $\psi(x)$ is continuous across $y = 0$,

$$\int_b \psi(x) \frac{\partial H_a}{\partial y}(x, 0, x_0, y_0)\,\mathrm{d}x = 0. \tag{2.56}$$

Hence, using (2.49), (2.54) and (2.56), (2.55) can be simplified to give,

$$\psi(x_0, y_0) = -\int_b \lambda(x) H_a(x, 0, x_0, y_0)\,\mathrm{d}x, \tag{2.57}$$

where $\lambda(x) = \partial\psi/\partial y$ is the strength of the vortex sheet on $|x| > 1, y = 0$.

Differentiation of (2.57) with respect to y_0 and x_0 gives the velocity at (x_0, y_0):

$$u(x_0, y_0) = -\int_b \lambda(x) \frac{\partial H_a}{\partial y_0}(x, 0, x_0, y_0)\,\mathrm{d}x, \tag{2.58}$$

$$v(x_0, y_0) = \int_b \lambda(x) \frac{\partial H_a}{\partial x_0}(x, 0, x_0, y_0)\,\mathrm{d}x. \tag{2.59}$$

It remains to find $\lambda(x)$. On the barrier as $y_0 \to 0$ (2.57) gives

$$\begin{aligned} g(x_0) &= \int_b \lambda(x) H_a(x, 0, x_0, 0)\,\mathrm{d}x, \\ &= 2\int_1^\infty \lambda(x) H_a(x, 0, x_0, 0)\,\mathrm{d}x + 2\int_{-\infty}^{-1} \lambda(x) H_a(x, 0, x_0, 0)\,\mathrm{d}x. \end{aligned} \tag{2.60}$$

which, since $g(x_0)$ is known, is an integral equation for the unknown $\lambda(x)$. Once $\lambda(x)$ is determined, (2.58) and (2.59) then give the velocity field at any arbitrary point (x_0, y_0).

2.4.2 Vortex sheets over the barrier: Rigid-lid solution

Let the vortex induce a velocity field $\tilde{u} - \mathrm{i}\tilde{v}$ on the barriers. Our task is to find a complex potential w such that on the barriers $y = 0$, $|x| \geq 1$

$$\Im(\mathrm{d}w) = \Im\left[(u - \mathrm{i}v)\mathrm{d}z\right] = -\Im\left[(\tilde{u} - \mathrm{i}\tilde{v})\mathrm{d}z\right], \tag{2.61}$$

that is the total normal velocity vanishes on the barriers.

Consider the following pair of conformal maps and their inverses (see Fig. 2.4):

$$\begin{aligned} z &= \frac{1}{2}\left(\zeta + \zeta^{-1}\right),\ \zeta = z + \sqrt{z^2 - 1}; \\ \zeta &= \mathrm{i}\left(\frac{1+\tau}{1-\tau}\right),\ \tau = \frac{\zeta - \mathrm{i}}{\zeta + \mathrm{i}}; \end{aligned} \tag{2.62}$$

which map the $z-$plane to the interior of the unit $\tau-$disk, with the boundary of the $\tau-$disk being the image of the barriers. Note the square root in (2.62) has positive imaginary part, so that the region of interest in the $\zeta-$plane is the upper-half plane.

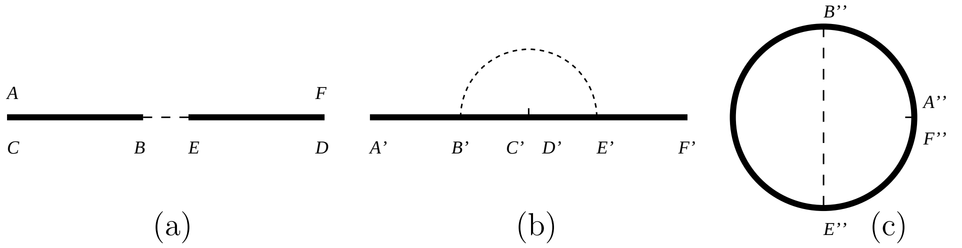

(a) (b) (c)

Figure 2.4: (a) The z-plane. (b) The ζ-plane. (c) The τ-plane. The dotted lines represent the location of the gap and the solid lines represent the two semi-infinite barriers. Note that the upper-half plane in (b) maps to the interior of the disc in (c).

On $\tau = e^{\mathrm{i}\phi}$, $-\pi < \phi \leq \pi$,

$$\begin{aligned}
\Im\left[\frac{\mathrm{d}w}{\mathrm{d}\phi}\right] &= -\Im\left[(\tilde{u}-\mathrm{i}\tilde{v})\frac{\mathrm{d}z}{\mathrm{d}\phi}\right] \\
&= -\Im\left[\mathrm{i}e^{\mathrm{i}\phi}(\tilde{u}-\mathrm{i}\tilde{v})\frac{\mathrm{d}z}{\mathrm{d}\zeta}\frac{\mathrm{d}\zeta}{\mathrm{d}\tau}\right], \\
&= n(\phi), \qquad (2.63)
\end{aligned}$$

where $n(\phi)$ is a known function.

The general solution for w inside the unit $\tau-$disk is,

$$w = \sum_{k=1}^{\infty} a_k \tau^k, \qquad (2.64)$$

where $a_k \in \mathbb{C}$ and $\tau = \rho e^{\mathrm{i}\phi}$, $0 \leq \rho \leq 1$. Thus (2.63) and (2.64) give

$$\Im\left[\sum_{k=1}^{\infty} a_k k \tau^{k-1} \frac{\mathrm{d}\tau}{\mathrm{d}\phi}\right] = n(\phi), \qquad (2.65)$$

or,

$$\Re\left[\sum_{k=1}^{\infty} a_k k \tau^{k-1} e^{\mathrm{i}k\phi}\right] = n(\phi), \qquad (2.66)$$

which is a Fourier-Series problem on $\pi < \phi \leq \pi$ for the unknown a_k. Hence,

$$k a_k = \frac{1}{\pi}\int_{-\pi}^{\pi} n(\phi) e^{-\mathrm{i}k\phi}\,\mathrm{d}\phi,\ k = 1, 2, \ldots. \qquad (2.67)$$

Now that $a_k, k = 1, 2, \ldots$ are known, the velocity field $u - \mathrm{i}v$ can be determined for arbitrary z,

$$u - \mathrm{i}v = \frac{\mathrm{d}w}{\mathrm{d}z} = \sum_{k=1}^{\infty} a_k k \tau^{k-1} \frac{\mathrm{d}\tau}{\mathrm{d}\zeta}\frac{\mathrm{d}\zeta}{\mathrm{d}z}, \qquad (2.68)$$

and hence the vortex can be advected by evaluating $u - \mathrm{i}v$ using (2.68) at the vortex location. In practice the infinite sum in (2.68) is truncated at $k = N$ for some large $N = 2^8$. Results were also compared against larger values of $N = 2^10$ and gave good agreement.

We distribute the points uniformly around the $\tau-$circle i.e. $\tau_j = j2\pi/M$, $j = 0, 1, \ldots, M-1$ which in turn gives a (non-uniform) distribution of points on the barrier.

2.4.3 Solution of the integral equation: Barrier method

The rigid-lid solution can be used to iteratively find $\lambda(x)$ along the barriers in the same way as the gap method. However, the x_0 derivative of (2.57) is first taken,

$$n(x_0) = \frac{\partial \psi(x_0, 0)}{\partial x_0} = -\int_b \lambda(x) \frac{\partial H_a}{\partial x_0}(x, 0, x_0, 0)\,\mathrm{d}x, \tag{2.69}$$

where $n(x_0)$ is the normal velocity to the barrier.

Define

$$\mathcal{K}_a = \frac{\partial H_a}{\partial x_0}(x, 0, x_0, 0), \tag{2.70}$$

so that,

$$\mathcal{K}_a(x - x_0) = -\frac{K_1\left(|x - x_0|/a\right)}{2\pi a}, \tag{2.71}$$

and for the infinite a case,

$$\mathcal{K}_\infty = -\frac{1}{2\pi\left(x - x_0\right)}. \tag{2.72}$$

The integral equation (2.69) is de-singularised as in (2.27):

$$n(x_0) = -\int_b \lambda(x)(\mathcal{K}_\infty(x - x_0) - \mathcal{K}_a(x - x_0))\,\mathrm{d}x + \int_b \lambda(x)\mathcal{K}_\infty(x - x_0)\,\mathrm{d}x \tag{2.73}$$

which is re-written as

$$\int_b \lambda(x)\mathcal{K}_\infty(x - x_0)\,\mathrm{d}x = f(x_0) + \int_b \lambda(x)(\mathcal{K}_\infty(x - x_0) - \mathcal{K}_a(x - x_0))\,\mathrm{d}x. \tag{2.74}$$

All integrals on the right hand side can be evaluated numerically.

Again iteration is used to solve for the left hand side, using all the known values on the right hand side:

$$\begin{aligned}\int_b \lambda^{(m+1)}(x)\mathcal{K}_\infty(x-x_0)\,\mathrm{d}x &= n(x_0) + \int_b \lambda^{(m)}(x)(\mathcal{K}_\infty(x-x_0) - \mathcal{K}_a(x-x_0))\,\mathrm{d}x \\ &= n^{(m)}(x_0), \end{aligned} \tag{2.75}$$

for $\lambda^{(m+1)}(x)$ given $n^{(m)}(x_0)$.

It remains to solve

$$\int_b \lambda^{(m+1)}(x)\mathcal{K}_\infty(x-x_0)\,\mathrm{d}x = n^{(m)}(x_0). \tag{2.76}$$

However this is precisely the rigid-lid problem with $n^{(m)}(x_0)$ is the normal velocity on the barrier and $\lambda^{(m+1)}(x)$ is the derivative of the streamfunction, with respect to x along the barrier. Using the method detailed in Section 2.4.2 the solution is

$$\begin{aligned}\lambda^{(m+1)}(x) &= \Re\frac{dw}{dz} \\ &= \Re\sum_{k=1}^{\infty} k a_k \tau^k \frac{d\tau}{dz}\end{aligned} \tag{2.77}$$

from (2.68), where $\tau = e^{\mathrm{i}\phi}$, a_k are the complex coefficients of the Fourier series of $n^{(m)}(x_0)$. Hence $\lambda(x)$ can be substituted in to (2.58) and (2.59) the velocity field everywhere.

2.5 Results

2.5.1 A test problem

When the vortex is far from the gap, the integral equation (2.20) is solved to find the streamfunction $\Lambda(x)$ along the gap. This is done numerically by discretizing the gap using $p = 2^8$ points at the values of $x_i = \cos(\theta_i)$, where $\theta_i = \pi i/p$, $i = 1, \ldots, p$. As a test case, the location of the vortex was taken at $x_v = 0$, $y_v = 1$ and the streamfunction computed along the gap for three different values of a. First, for the rigid-lid case (numerically, taking $a = 10^8$ to simulate an infinite a). Here, the 'extra' contribution to the velocity, i.e. $(\mathcal{L}_\infty(x - x_0) - \mathcal{L}_a(x - x_0))$, is negligible hence, only one iteration is required. Similarly, for $a = 100$, the 'extra' contribution is still small but two iterations are required to accurately obtain the streamfunction.

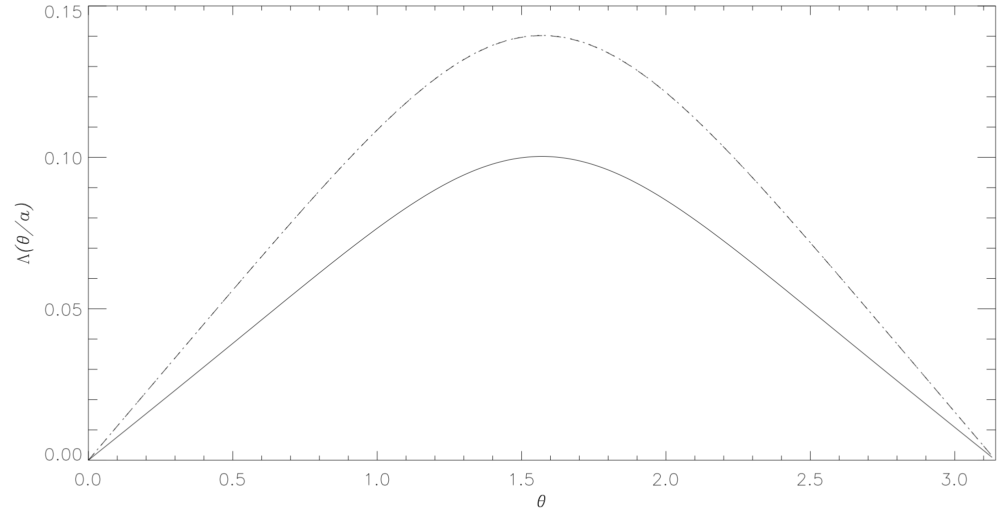

Figure 2.5: The streamfunction along the gap, Λ, is plotted as a function of θ for the rigid-lid case (dotted), $a = 100$ (dashed) and $a = 2$ (solid)

Note that for large $a = 100$, there is little difference between the streamfunction calculated numerically, and the exact rigid-lid streamfunction. However, for $a = 2$, the 'extra' contribution is greater and four iterations are required to calculate the final streamfunction. The difference between $a = 2$ and the rigid-lid case and is quite notable in Fig. 2.5. The impact of the deformation radius can be seen as the exponential decay of the $K_0(r/a)$ streamfunction causes a smaller magnitude of the streamfunction along the gap induced by the point vortex.

Similarly in Fig. 2.6, the barrier is discretized using a sequence of maps (refer to (2.62) and Fig. 2.4 for details). A high resolution of $p = 2^{11}$ is used so that have a greater number of points along the barrier,

$$x_i = -\frac{1}{2}(\cot(\phi_i) + \tan(\phi_i)), \tag{2.78}$$

$$\mathrm{d}x_i = \frac{1}{4}(\mathrm{cosec}^2(\phi_i) - \sec^2(\phi_i)), \tag{2.79}$$

where $\phi_i = 2\pi i/p$.

The vortex was located close to the gap at $x_v = 0$, $y_v = 0.04$. The difference for the cases between the rigid-lid case and $a = 2$ can be seen in Fig. 2.6-2.7.

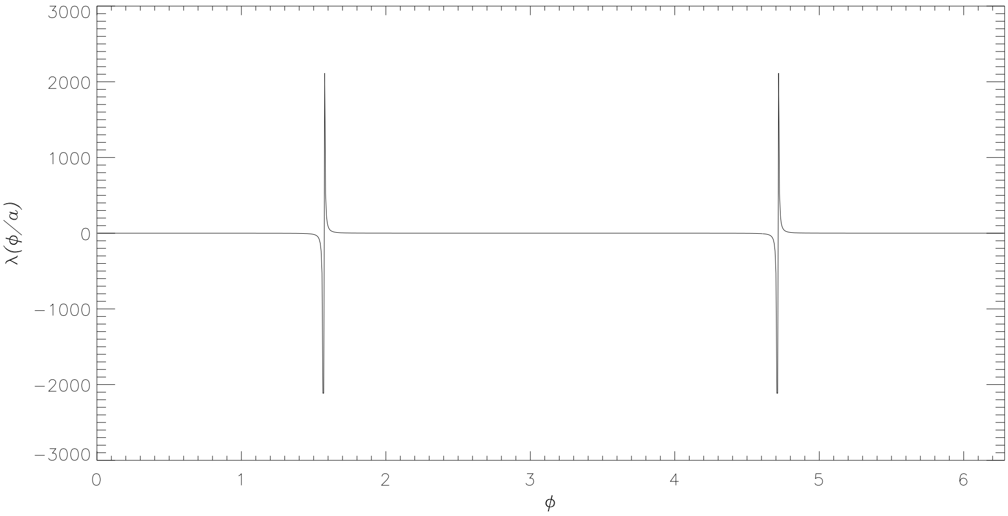

Figure 2.6: The streamfunction derivative along the semi-infinite barriers, λ, is plotted as a function of ϕ for the rigid-lid case. Here $a = 10^8$.

The spikes in the streamfunction are present near the barrier tips i.e. at $x = 1$. This is because for small distances from the barrier tip the solution of the Helmholtz equation should give a velocity field which tends to that governed by Laplace's equation for which it is well known that such a velocity field has an inverse square root singularity. However, due to the change of variable (see (2.78) and (2.79)), the contribution of the weight vanishes at the tips of the barriers (where $\phi_i = \pi/4$ for the negative barrier tip and $\phi_i = 3\pi/4$ for the positive barrier tip). The $y-$axis values show that for $a = 2$, the values along the boundary are very weak. This also highlights the quicker decay as a is reduced. The effect of the vortex sheet is that

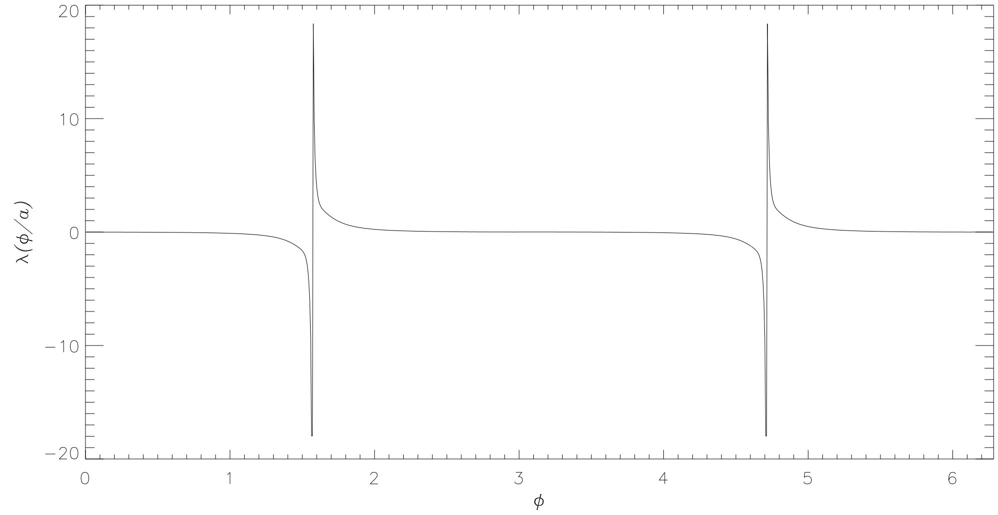

Figure 2.7: Same as in Fig. 2.6 but with $a = 2$.

its strength decreases as a decreases.

2.5.2 Point vortex trajectories

When far from the gap, the gap method is used to calculate $\Lambda(x)$, which is then substituted into (2.21) and (2.22) to calculate the velocity field at the vortex location and then the vortex is advected using the time dependent fourth order Runge-Kutta integration routine. However, the method requires that the horizontal velocity $u(x_v, y_v)$ caused by the vortex sheet over the gap cancels out the horizontal velocity $u_{im}(x_v, y_v) = \frac{K_1(2y_c/a)}{2\pi a}$ induced by the image of the vortex on the opposite side of the wall. Numerically, these do not cancel out exactly, causing a loss of accuracy near the gap. Hence, when close to the gap ($|x_v| < 1$ and $|y_v| < 0.05$), the barrier method is used to calculate the streamfunction derivative, $\lambda(x)$ which is then substituted into (2.58) and (2.59) and the point vortex is advected in the same way. When the vortex is travelling fast, close to the barrier ($y_v \leq 0.1$), the time step, $\Delta t = 0.05$ and otherwise, $\Delta t = 0.1$.

First, the analytical solution for the rigid-lid case can be used as a comparison for the limit as $a \to \infty$. In Fig. 2.8 the analytical trajectories are plotted over the numerically computed trajectories to show there is a good agreement.

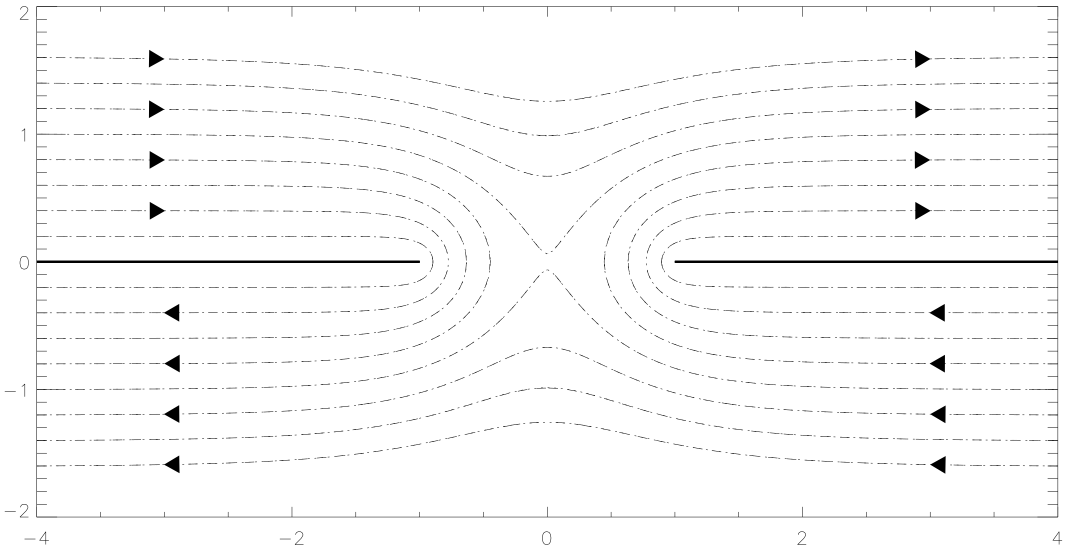

Figure 2.8: The numerical trajectories (dashed) for $a = \infty$ of a point vortex starting from $x_v = -4$, $y_v = 0.2n$, $n = 1, \dots, 8$ and the exact analytical trajectories (dotted) that pass through the initial location of the numerical trajectories.

In Fig. 2.9, with $a = 100$, the vortex paths are similar to that of the rigid-lid ($a \to \infty$) case, however, the velocities are different, with point vortices decreasing in speed. This is due to the rapid decay of the Bessel function, $K_1(r/a)$ for large r.

In Fig. 2.10, $a = 2$. As can be seen, the paths travel straighter taking longer to start dipping towards the gap. This is because the point vortex takes longer to feel the effects of the gap, with the vortex behaving as though it were near an infinite wall. When close to the barrier, the influence of the nearer barrier is like a single semi-infinite barrier. Although the rest of the paths look similar, the critical trajectory (the separatrix that divides the vortices that leap across the gap and the vortices that pass through them) has changed. It is found that vortices go through the gap more readily.

Although the results for this look good for $a > 1$, for $a < 1$ the results are inaccurate and implausible. In Fig. 2.11, with $a = 0.5$ a vortex is started at $x_v = -2$, $y_v = 0.2$ and passes through the barrier which is, of course, non-physical. The reason for this may be related to the fact that in the infinite a case the decay

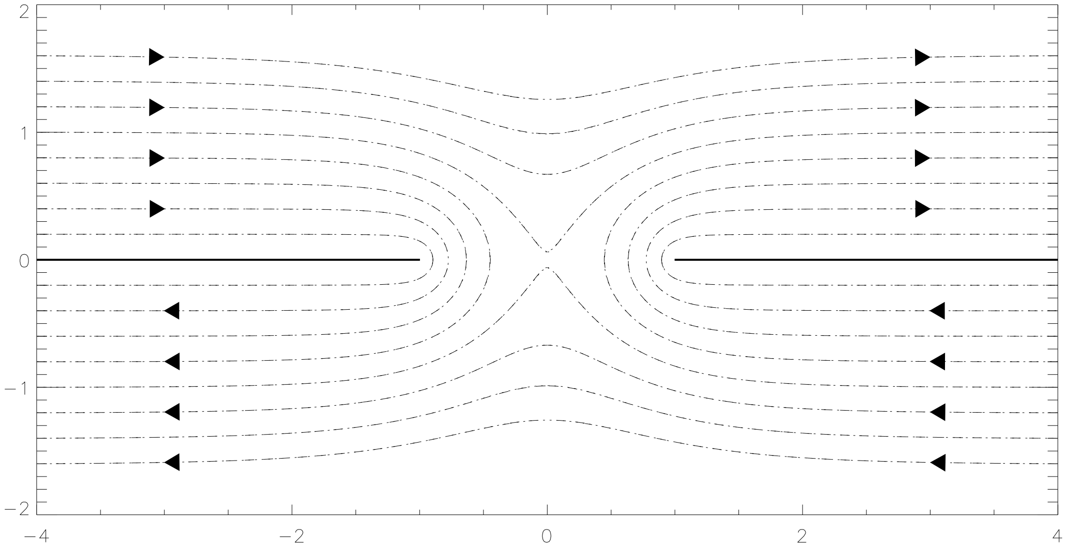

Figure 2.9: Same as in Fig. 2.8 but with $a = 100$.

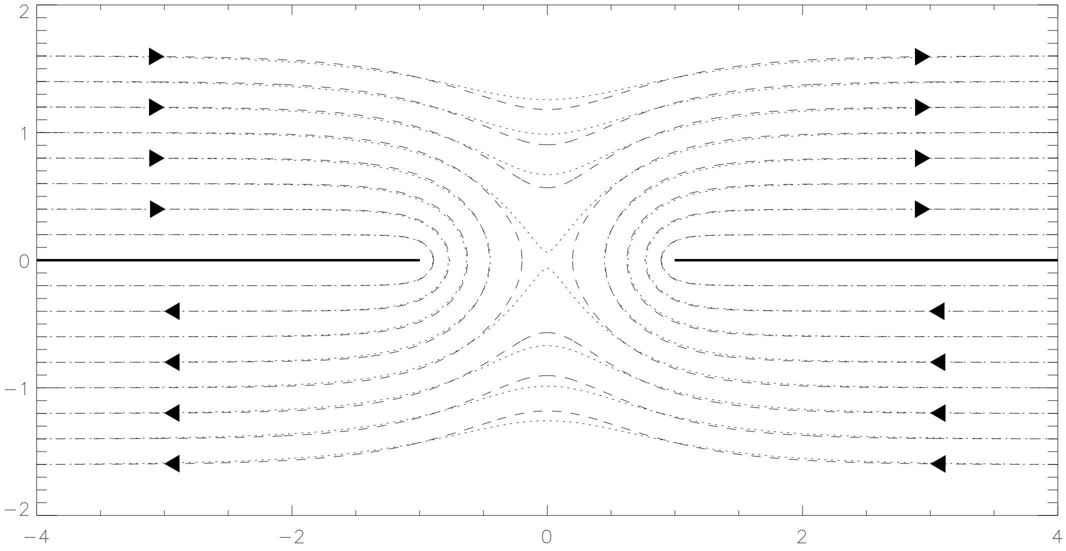

Figure 2.10: Same as in Fig. 2.9 but with $a = 2$

of the velocity along the barriers is algebraic but for finite a the increasingly rapid exponential decay means the method is no longer valid. A new method is formulated and discussed in the next chapter which solves the integral equation (2.57) in a different way, which allows trajectories to be found for finite $a \leq 3$.

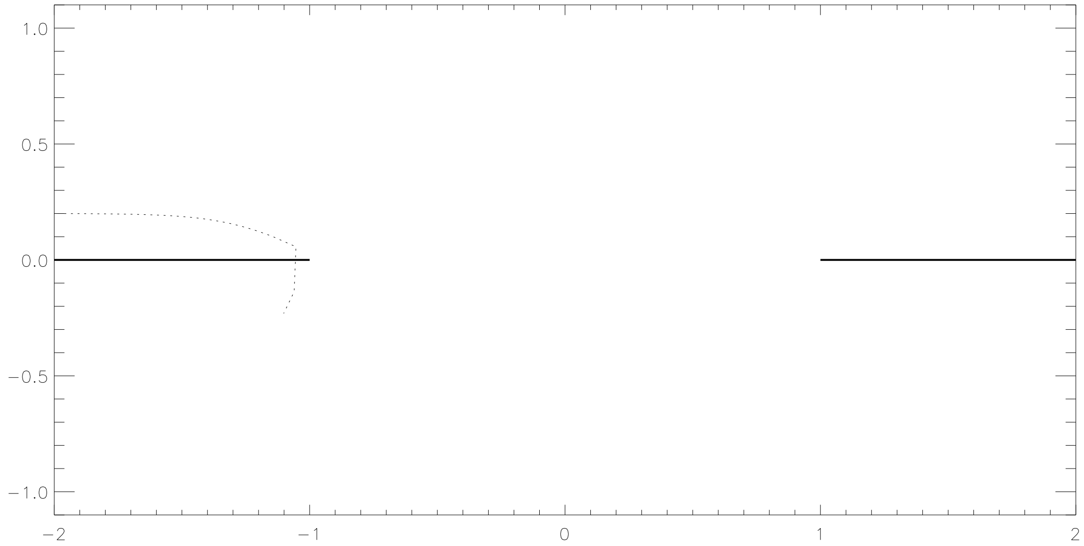

Figure 2.11: A single vortex is tracked from $x_v = -2$, $y_v = 0.2$. The vortex seems it is going through the barrier, which is impossible.

2.6 Conclusions

The effects of a large finite Rossby deformation radius on a point vortex near a gap in a wall has been investigated. To compute the point vortex trajectories, first we assume that there is a vortex sheet over the gap between the two semi-infinite barriers as there is a jump in tangential velocity across the gap. The streamfunction owing to this vortex sheet must be such that the Helmholtz equation is satisfied everywhere and that the streamfunction along the semi-infinite barriers is zero. Using Green's theorem, a hyper-singular integral equation is found that when solved yields the streamfunction associated with the vortex sheet.

The equation is de-singularised by subtracting the rigid-lid Green's function and solving the equation iteratively using the exact solution for the rigid-lid case found by Johnson and McDonald (2004) and thus, the streamfunction that satisfies the Helmholtz equation can be found. The integral over the logarithmic singularity present in the integrand is dealt with using quadratic polynomial interpolation and the analytical solution of the integral over the logarithmic function. However, when the vortex passes through the gap, there is a singularity encountered in the velocity field equations.

Hence a conjugate method, with two vortex sheets over the semi-infinite barriers is used when passing through the gap. The integral equation is found in the same way and de-singularised as before. The rigid-lid solution is again used as the basis for solving the integral equation.

The numerical results for very large a show good comparison with the analytical trajectories found by Johnson and McDonald (2004). The energy along the path can be calculated and remains approximately constant as expected.

Decreasing a increases the tendency of a vortex to go through the gap as it takes longer to notice the presence of the other barrier. However, this method is slow and fails for small a as the initial guess is based on the infinite a (rigid-lid) case. Hence a new method, for small a is formulated and discussed in the next chapter.

Chapter 3

Vortex motion near a gap in a wall: Small Rossby radius case

The iterative method described in Chapter 2 is effective when dealing with large a, however, there are inaccuracies when $a \leq \mathrm{O}(1)$. This chapter details a new method for solving the integral equation. First, the problem is split into even and odd vortex pairs so that the integral equation can be expressed as two integrals over a single barrier in Section 3.1. The method of solving the integral equations is detailed in Section 3.2. There is a region of overlap in $a-$space between the iterative solution and solution by the new method (herein referred to as the matrix method) and the solutions are compared in Section 3.3.1. Vortex trajectories for $a < 1$ are investigated in Section 3.3.2. The integral equation method is then adapted to include a variety of background flows through the gap in Section 3.4. A summary is presented in Section 3.5.

3.1 Integral equation: Even and odd vortex pairs

The integral equation along the barriers is (2.60) in Section 2.4. The unknown $\lambda(x)$ is the strength of the vortex sheet and it must satisfy

$$\begin{aligned} g(x_0) &= \int_b \lambda(x) H_a(x,0,x_0,0)\,\mathrm{d}x, \\ &= 2\int_1^{\infty} \lambda(x) H_a(x,0,x_0,0)\,\mathrm{d}x + 2\int_{-\infty}^{-1} \lambda(x) H_a(x,0,x_0,0)\,\mathrm{d}x. \end{aligned} \tag{3.1}$$

In this chapter, (3.1) is solved by discretizing the $x-$coordinate along the barriers and solving the subsequent system of linear equations by matrix inversion. Note later when we treat a vortex patch (see Chapter 4), the streamfunction $g(x_0)$ along the barriers is not known, so the derivative with respect to x_0 of (3.1) is used instead, this being equivalent to the normal velocity, which is straightforward to determine for vortex patches.

Thus, $n(x)$, the normal velocity induced along the barriers by the vortex patches, is used by differentiating (3.1) with respect to x_0, i.e.,

$$\begin{aligned} \frac{\partial g}{\partial x_0}(x_0) &= n(x_0) \\ &= \int_b \lambda(x) \frac{\partial H_a}{\partial x_0}(x,0,x_0,0)\,\mathrm{d}x, \\ &= 2\int_1^{\infty} \lambda(x) \frac{\partial H_a}{\partial x_0}(x,0,x_0,0)\,\mathrm{d}x + 2\int_{-\infty}^{-1} \lambda(x) \frac{\partial H_a}{\partial x_0}(x,0,x_0,0)\,\mathrm{d}x. \end{aligned} \tag{3.2}$$

Now, the normal velocity component at the barriers can be split into the sum of an even and odd part as follows:

$$\begin{aligned} n(x_0) &= \frac{n(x_0)+n(-x_0)}{2} + \frac{n(x_0)-n(-x_0)}{2} \\ &= n_e(x_0) + n_o(x_0). \end{aligned} \tag{3.3}$$

For the case of a point vortex at (x_v, y_v), the even and odd contributions to the

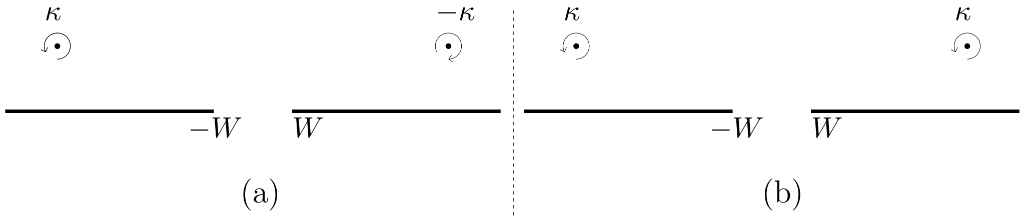

Figure 3.1: Even (a) and odd (b) vortex pairing. The even and odd-ness refers to the normal velocity along the barriers.

normal velocity component at the barrier can be explicitly written as,

$$\begin{aligned} n_e(x_0) =& (x_0 - x_v)\frac{\kappa K_1\left(\sqrt{(x_0-x_v)^2+y_v^2}\right)}{2\pi\sqrt{(x_0-x_v)^2+y_v^2}} \\ &- (x_0 + x_v)\frac{\kappa K_1\left(\sqrt{(x_0+x_v)^2+y_v^2}\right)}{2\pi\sqrt{(x_0+x_v)^2+y_v^2}}, \end{aligned} \tag{3.4}$$

and

$$\begin{aligned} n_o(x_0) =& (x_0 - x_v)\frac{\kappa K_1\left(\sqrt{(x_0-x_v)^2+y_v^2}\right)}{2\pi\sqrt{(x_0-x_v)^2+y_v^2}} \\ &+ (x_0 + x_v)\frac{\kappa K_1\left(\sqrt{(x_0+x_v)^2+y_v^2}\right)}{2\pi\sqrt{(x_0+x_v)^2+y_v^2}}. \end{aligned} \tag{3.5}$$

The pairing of the vortices giving rise to $n_e(x_0)$ and $n_o(x_0)$ is shown in Fig. 3.1.

For the even case, let the strength of the vortex sheet induced along the barriers by the vortex be $\lambda_1(x)$ and use the notation used previously in Chapter 2 for convenience,

$$\mathcal{K}_a(x - x_0) = \frac{\partial H_a}{\partial x_0}(x, 0, x_0, 0). \tag{3.6}$$

Hence, from (3.2),

$$n_e(x_0) = 2\int_{-\infty}^{-1} \lambda_1(x)\mathcal{K}_a(x - x_0)\,\mathrm{d}x + 2\int_{1}^{\infty} \lambda_1(x)\mathcal{K}_a(x - x_0)\,\mathrm{d}x. \tag{3.7}$$

By substituting $x = -x$ and changing the limits accordingly,

$$\begin{aligned} n_e(x_0) &= -2\int_{\infty}^{1} \lambda_1(-x)\mathcal{K}_a(-x+x_0)\,\mathrm{d}x - 2\int_{-1}^{-\infty} \lambda_1(-x)\mathcal{K}_a(-x+x_0)\,\mathrm{d}x \\ &= 2\int_{-\infty}^{-1} \lambda_1(-x)\mathcal{K}_a(-x+x_0)\,\mathrm{d}x + 2\int_{1}^{\infty} \lambda_1(-x)\mathcal{K}_a(-x+x_0)\,\mathrm{d}x, \end{aligned} \tag{3.8}$$

Since $\mathcal{K}_a(-x+x_0) = -\mathcal{K}_a(x-x_0)$,

$$n_e(x_0) = -2\int_{-\infty}^{-1} \lambda_1(-x)\mathcal{K}_a(x-x_0)\,\mathrm{d}x - 2\int_{1}^{\infty} \lambda_1(-x)\mathcal{K}_a(x-x_0)\,\mathrm{d}x, \tag{3.9}$$

which together with (3.8) implies,

$$\lambda_1(x) = -\lambda_1(-x), \tag{3.10}$$

i.e. $\lambda_1(x)$ is odd in x.

Using the change of variable, $x = -x$, the integral over the negative barrier can be expressed with positive limits,

$$2\int_{-\infty}^{-1} \lambda_1(x)\mathcal{K}_a(x-x_0)\,\mathrm{d}x = 2\int_{1}^{\infty} \lambda_1(x)\mathcal{K}_a(x+x_0)\,\mathrm{d}x. \tag{3.11}$$

Hence, the even part of the velocity can be expressed as the integral over positive limits:

$$\begin{aligned} n_e(x_0) &= 2\int_{1}^{\infty} \lambda_1(x)\mathcal{K}_a(x+x_0)\,\mathrm{d}x + 2\int_{1}^{\infty} \lambda_1(x)\mathcal{K}_a(x-x_0)\,\mathrm{d}x \\ &= 2\int_{1}^{\infty} \lambda_1(x)(\mathcal{K}_a(x-x_0) + \mathcal{K}_a(x+x_0))\,\mathrm{d}x. \end{aligned} \tag{3.12}$$

Similarly, for the odd vortex pair, let the normal velocity induced at the barriers be $\lambda_2(x)$, and it can be shown that

$$n_o(x_0) = 2\int_{1}^{\infty} \lambda_2(x)(\mathcal{K}_a(x-x_0) - \mathcal{K}_a(x+x_0))\,\mathrm{d}x. \tag{3.13}$$

3.2 Numerical solution of the integral equation

Integral equations (3.12) and (3.13) are singular since

$$\mathcal{K}_a(x \pm x_0) = \frac{A}{x \pm x_0} + \mathrm{O}(1), \text{ as } x \to \mp x_0, \tag{3.14}$$

where A is a constant. Thus the integrals in (3.12) and (3.13) need to be interpreted in a Cauchy principal value sense. The solutions $\lambda_1(x)$ and $\lambda_2(x)$ are also expected to have inverse-square-root singularities at the barrier tip. That is,

$$\lambda_{1,2}(x) \sim \frac{B}{\sqrt{x-1}} \text{ as } x \to 1, \tag{3.15}$$

where B is a constant. This is because for small distances from the barrier tip the solution of the Helmholtz equation should give a velocity field which tends to that governed by Laplace's equation, for which it is well known that such a velocity field has an inverse-square-root singularity.

Let

$$\mathcal{E}(x, x_0) = \mathcal{K}_a(x - x_0) + \mathcal{K}_a(x + x_0), \tag{3.16}$$

and approximate (3.12) as

$$n_e(x_0) = 2\int_1^{1+\epsilon} \lambda_1(x)\mathcal{E}(x, x_0)\,\mathrm{d}x + 2\int_{1+\epsilon}^{L} \lambda_1(x)\mathcal{E}(x, x_0)\,\mathrm{d}x, \tag{3.17}$$

where $L \gg 1$ is the truncation length of the barrier and $0 < \epsilon \ll 1$. The first integral in (3.17) encompasses the inverse square root singularity of $\lambda_1(x)$ and, provided x_0 is not close to $x = 1$ (i.e. the vortex is not near the barrier tip), it is integrable and behaves like $\sqrt{\epsilon}$ as $\epsilon \to 0$. Thus to a good approximation, we take $\epsilon = 0$ and (3.17) becomes

$$n_e(x_0) \simeq 2\int_1^{L} \lambda_1(x)\mathcal{E}(x, x_0)\,\mathrm{d}x. \tag{3.18}$$

The integral in (3.18) is discretized into N equally-spaced points,

$$x_i = 1 + (i-1)h,\ i = 1, \ldots, N, \tag{3.19}$$

where $h = (L-1)/(N-1)$. Let

$$x_0^j = x_j + \frac{h}{2},\ j = 1, \ldots, N, \tag{3.20}$$

be the mid-points of the $[x_i, x_{i+1}]$ intervals values along the barrier (see Fig. 3.2).

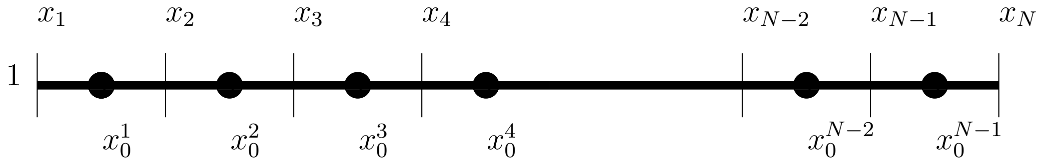

Figure 3.2: The x_0 values are used to integrate and the singularity is positioned at x_0^j.

Vanden-Broeck and Smith (2010) used this method of discretization with the singularity placed half-way between two consecutive integration points, since it implies the singularity may be effectively ignored.

$$\int_1^L \mathcal{E}(x, x_0)\lambda_1(x)\,\mathrm{d}x \simeq \sum_{i=1}^{N} \lambda_1(x_i)\mathcal{E}(x_i, x_0^j)w_i, \tag{3.21}$$

where w_i are the usual trapezoidal weights:

$$w_i = \begin{cases} \frac{h}{2} & i = 1, N \\ h & \text{otherwise.} \end{cases} \tag{3.22}$$

That is, by considering x_0^j as the midpoints, the presence of the $(x - x_0^j)$ singularity is accounted for (see Appendix A).

Hence the integral equation (3.12) can be approximated by the NxN linear system,

$$\sum_{i=1}^{N} \mathcal{E}(x_i, x_0^j)\lambda_1(x_i)w_i \simeq n_e(x_0^j),\ j = 1, \ldots, N, \tag{3.23}$$

where the unknowns $\lambda_1(x_i)$ $i = 1, \ldots, N$ are found by numerically inverting (using NAG library routine F07AEF) the known $N \times N$ coefficient matrix $\mathcal{E}(x_i, x_0^j)$ $i, j = 1, \ldots, N$. Similarly the solution $\lambda_2(x)$ to (3.13) can be found.

Once the $\lambda_{1,2}(x_i), i = 1, \ldots, N$ are known, the velocity field at any point (x_0, y_0). First note $\lambda(x) = \lambda_1(x) + \lambda_2(x)$ and substituting in (2.58) and (2.59) gives,

$$u(x_0, y_0) = -\int_b \lambda(x)\frac{\partial H_a}{\partial y_0}(x, 0, x_0, y_0)\,\mathrm{d}x, \tag{3.24}$$

$$v(x_0, y_0) = \int_b \lambda(x)\frac{\partial H_a}{\partial x_0}(x, 0, x_0, y_0)\,\mathrm{d}x. \tag{3.25}$$

These integrals can be evaluated using truncation and the trapezium rule. The length of the barrier is taken to $13a$ where the velocity field induced by the point vortex is less than 10^{-6}. A high number of points are therefore required to compute the matrix. A value of $N = 2^{11}$ was taken.

3.3 Vortex trajectories

3.3.1 Comparison with iterative method

To test the matrix method we first compare it to the iterative method when $a \geq 1$. There is a good comparison between trajectories as can be seen in Figs. 3.3–3.5 where the numerical trajectories are found using the matrix method (dotted lines) and the iterative method (dashed) for $a = 10, 2$ and 1. Thus we can be confident that both the numerical approaches produce accurate results for this range of a. The matrix method though, is not reliant on iteration using the exact $a \to \infty$ solution. Thus we can apply it to the case $a < 1$ which failed to converge using the iterative method. This we do in the next subsection.

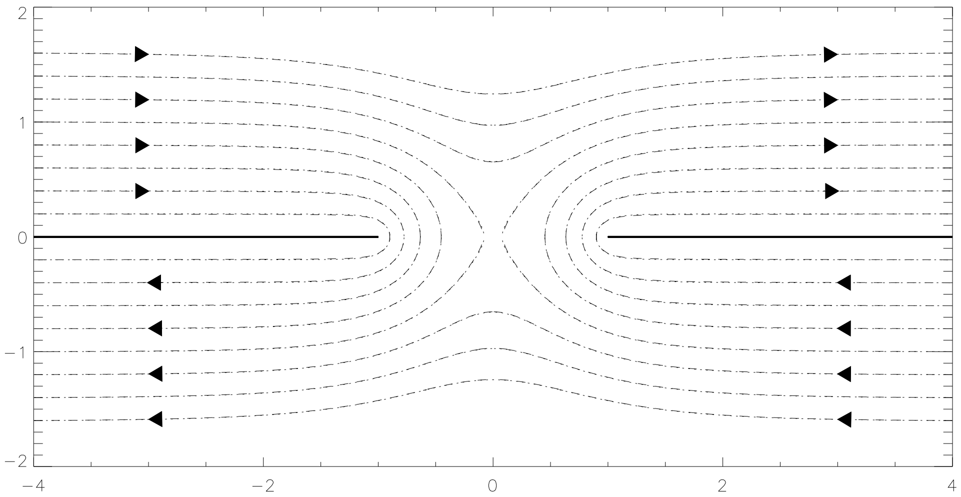

Figure 3.3: Numerical trajectories for the matrix method (dotted) and iterative method (dashed) with $a = 10$. Arrowheads indicate direction of motion of positive vortices.

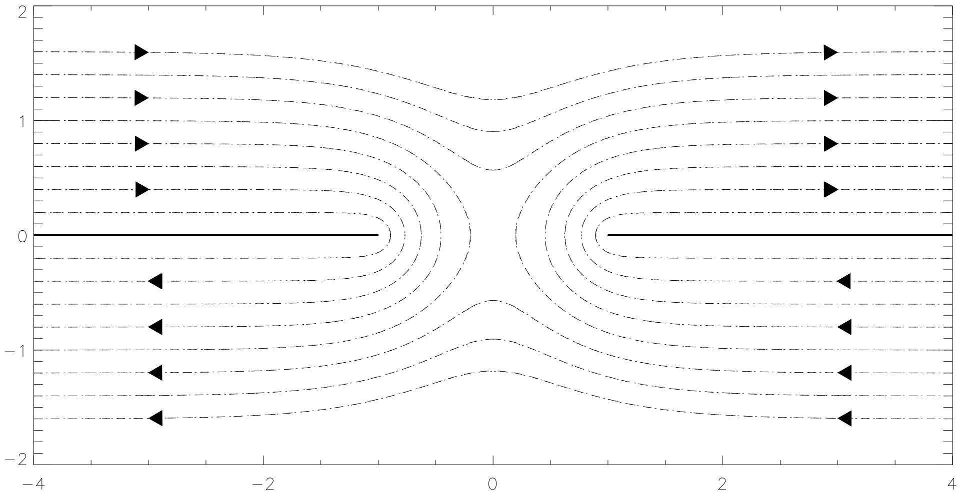

Figure 3.4: Same as in Fig. 3.3 but $a = 2$.

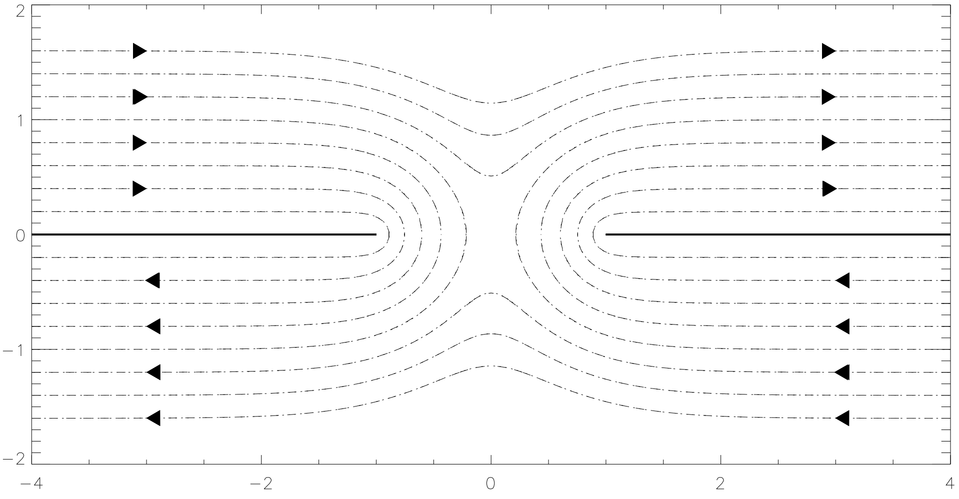

Figure 3.5: Same as in Fig. 3.4 but $a = 1$.

3.3.2 Numerical trajectories for small a and the separatrix

In Fig. 3.6, the trajectories for $a = 0.5$ (dotted) and $a = 1$ (dashed) are plotted together. It is clear that, although the trajectories look similar, there are differences

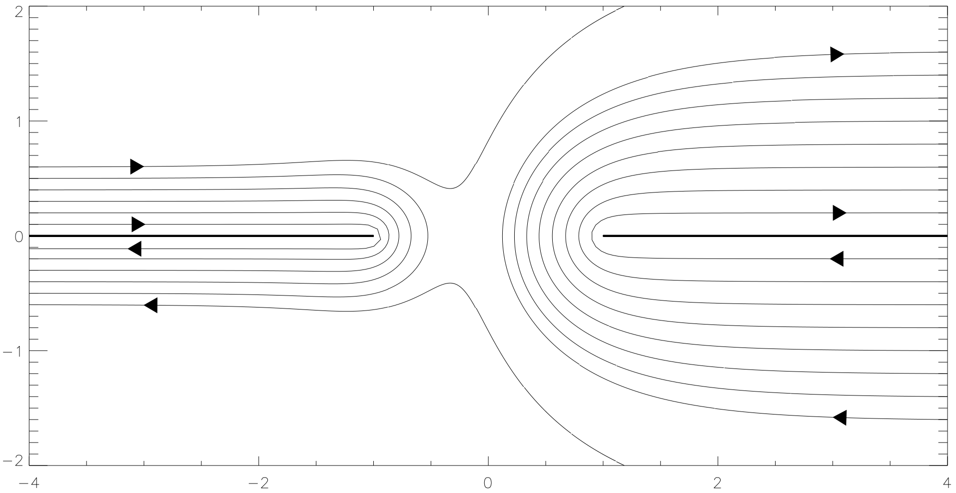

Figure 3.6: Numerical trajectories using the matrix method for the $a = 1$ (dashed) and the $a = 0.5$ (dotted).

when close to the gap, with $a = 1$ trajectories turning into the gap sooner than the $a = 0.5$ trajectories. For larger a the effect of the gap is felt earlier owing to the increased range of influence of the gap. However, when further away, say when the point vortex is initially at $(-4, 1.2)$, the trajectory for $a = 0.5$ takes longer for the trajectory to start dipping but still cuts the $y-$axis lower than for $a = 1$. This is because the vortex with $a = 0.5$ feels the effect of the second barrier less strongly when over the gap.

The numerical method can be used to quantify the effect the Rossby radii has on the separatrix i.e. the critical trajectory which divides those vortices which pass through the gap from those that leap across. A point vortex located close to the origin at $(10^{-6}, 10^{-6})$ is advected until the vortex passes the line, $|x| = 5$, where the motion becomes effectively that of a point vortex near a wall. Let this distance y be denoted as $y_{sep}(1/a)$. For the rigid-lid case, $y_{sep}(0) = 1$. The quantity $y_{sep}(1/a)$ has been computed for various values of a and plotted as a function against $1/a$ in Fig. 3.7 which clearly shows that y_{sep} is further from the $x-$axis as a decreases, i.e. a^{-1} increases. That is, there is an enhanced ability for vortices to pass through the gap as a decreases. However the effect is relatively minor, there being less than 10% change in y_{sep} over the range of a tested. This effect is due to the exponential decay of K_1 as a decreases; so the opposite barrier has a decreasing influence on the vortex as a decreases.

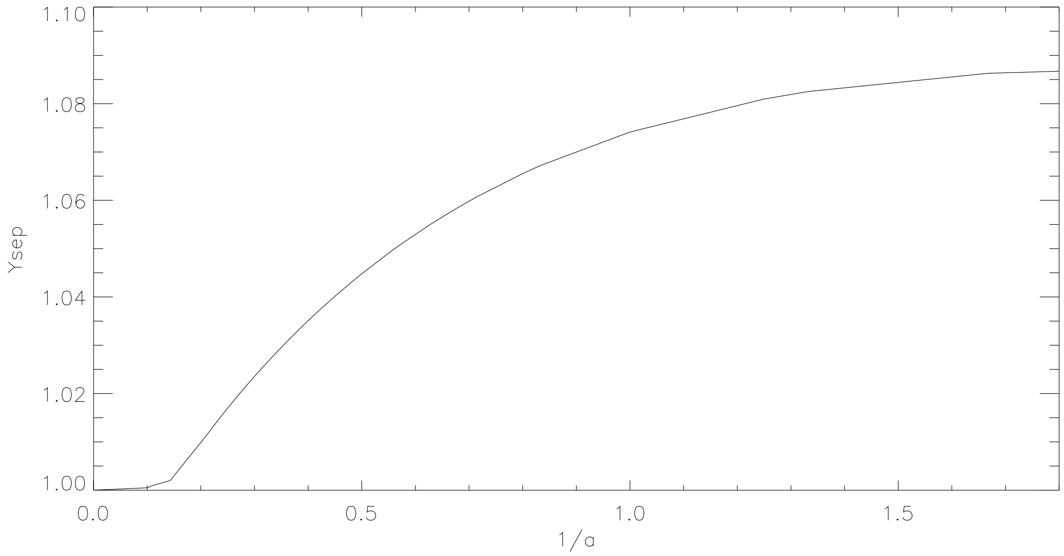

Figure 3.7: Value of y_{sep} against $1/a$. The tendency for vortices to pass through the gap is increased with decreasing a.

3.4 Background flows

The advection of vortices by ambient currents and background flows will influence their trajectories. Two background flows are considered here.

3.4.1 Uniform symmetric flow through the gap

For uniform flow (velocity field symmetric about $x = 0$) through the gap with streamfunction ψ_s, we can derive an integral equation identical to (3.1) with the streamfunction along the boundary given by,

$$\psi_s(x, 0) = \frac{\mathcal{F}}{2\pi}\operatorname{sgn}(x),\ |x| > 1, \tag{3.26}$$

where $\mathcal{F}$ is the flux through the gap and the subscript s denotes symmetric. Exploiting the fact that $\psi_s(x, 0)$ is odd yields the following integral equation,

$$\frac{\mathcal{F}}{2\pi} = 2\int_1^\infty \lambda_s(x)(H_a(x, 0, x_0, 0) - H_a(x, 0, -x_0, 0))\,\mathrm{d}x, \tag{3.27}$$

where $\lambda_s(x)$ is the strength of the vortex sheet along the barriers. Once $\lambda_s(x)$ is known then the streamfunction at any point (x_0, y_0) is found from

$$\psi_s(x_0, y_0) = -\int_b \lambda_s(x)H_a(x, 0, x_0, y_0)\,\mathrm{d}x. \tag{3.28}$$

The integral equation is solved in the same way as in the previous section. Using the computed $\lambda_s(x)$, streamlines with constant streamfunction, $\psi_s(x, y)$ are plotted for $a = 0.5, 1, 2$ and 10 in Figs. 3.8-3.11 with $\mathcal{F} = 1$. The values of $\psi_s = (1-n/10)/2\pi$ where $n = 0, \ldots, 20$ where $\psi_s = \pm 1/2\pi$ is the value of the contour along the barriers on the positive and negative barrier respectively and the centre line has $\psi_s = 0$. Notice as a increases, the distance between the contours increases. Small a implies that the background flow is strong, almost jet like, along the barriers but decreases in magnitude quickly further away from the gap. As a increases, the background flow has a stronger effect further away from the gap, i.e. it decays less rapidly. Again this behaviour is expected since with increasing a, the Green's function K_0 decays less rapidly. The flow in Fig. 3.11 is very close to that of classic potential flow through a finite width gap.

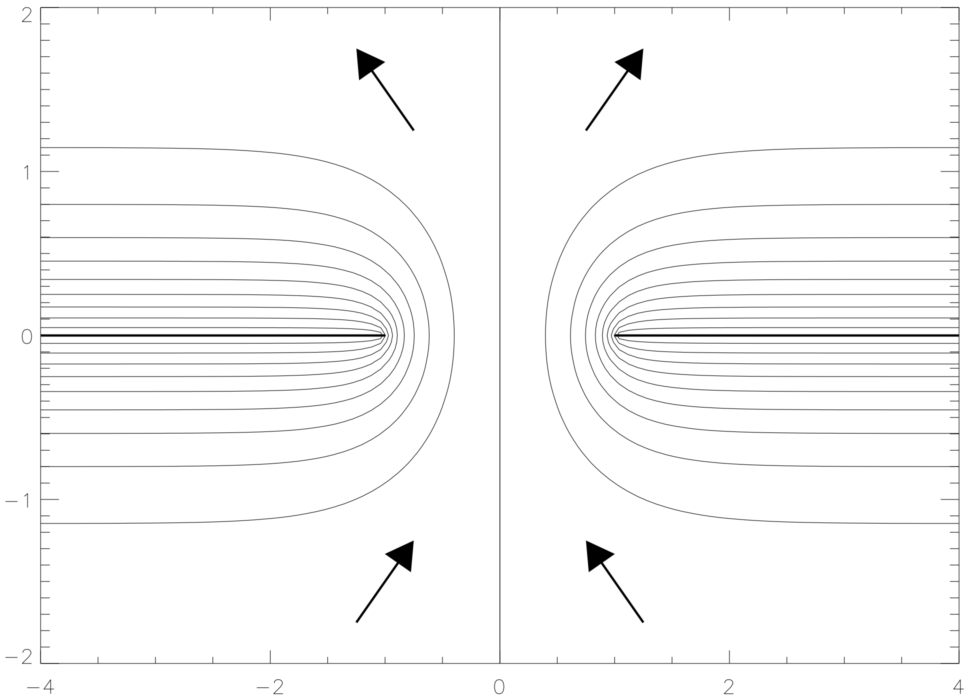

Figure 3.8: Streamlines of ψ_s plotted for $a = 0.5$. Contours are drawn at equal intervals with $\psi_s = \pm 1/2\pi$ on the barriers. Large arrows indicate direction of flow.

If a point vortex is present, once $\lambda_s(x)$ is obtained, the velocity field at the point vortex location can be computed using,

$$u(x_0, y_0) = \int_b \lambda_s(x) \frac{\partial H_a}{\partial y_0}(x, 0, x_0, y_0)\,\mathrm{d}x, \tag{3.29}$$

$$v(x_0, y_0) = -\int_b \lambda_s(x) \frac{\partial H_a}{\partial x_0}(x, 0, x_0, y_0)\,\mathrm{d}x. \tag{3.30}$$

It is then added to the computed velocity field with zero background flow. The discretization of the barriers is kept the same.

In Fig. 3.12, numerical trajectories of point vortices are plotted for $a = 0.5$

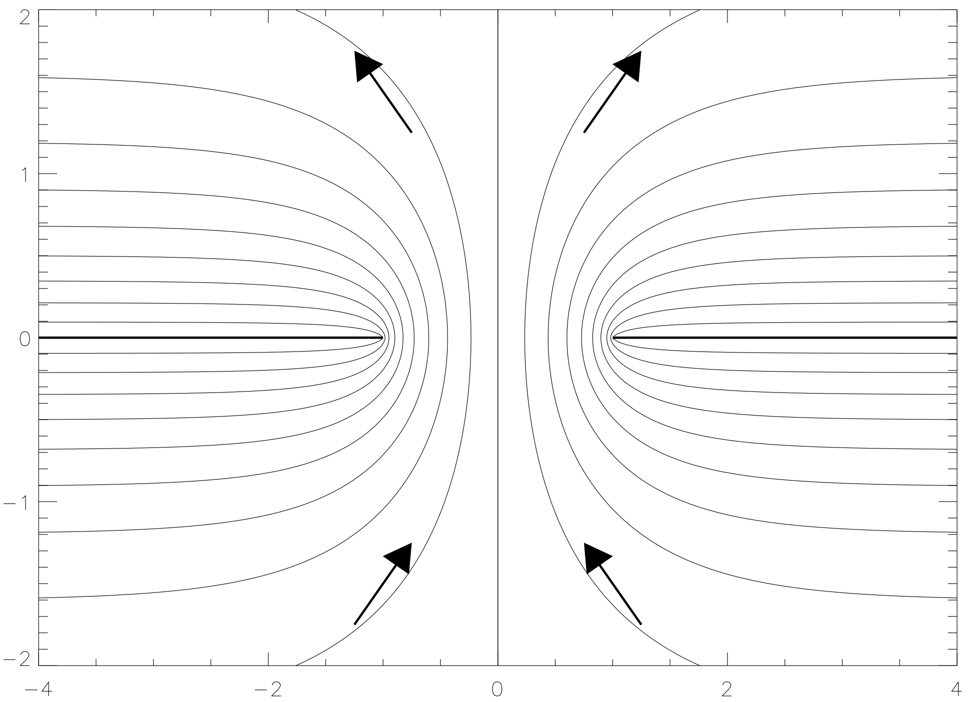

Figure 3.9: Same as Fig. 3.8 but $a = 1$.

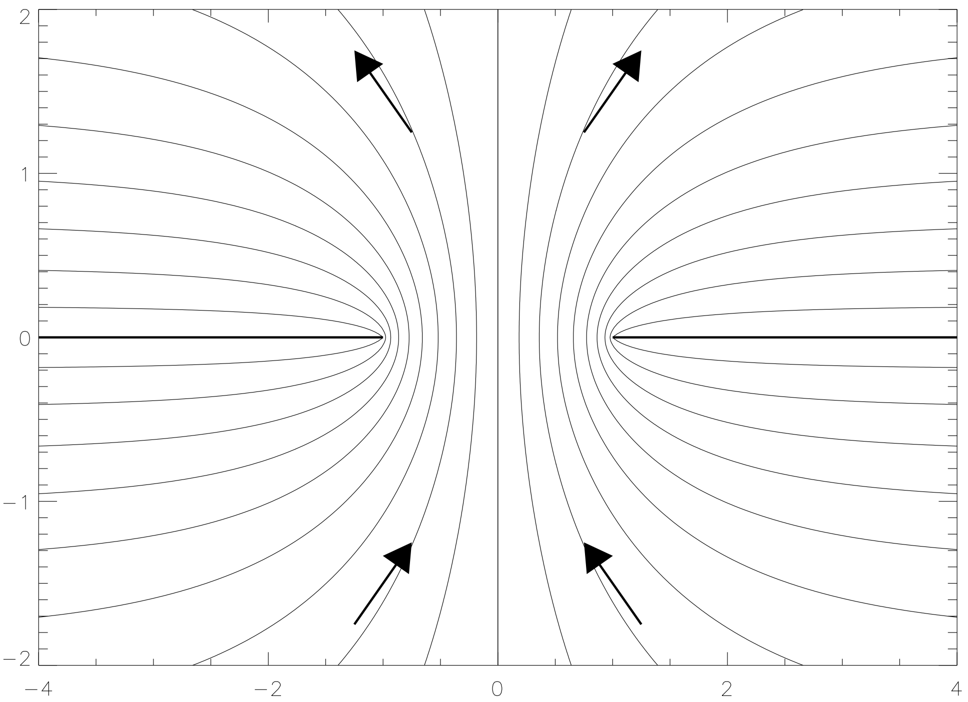

Figure 3.10: Same as Fig. 3.9 but $a = 2$.

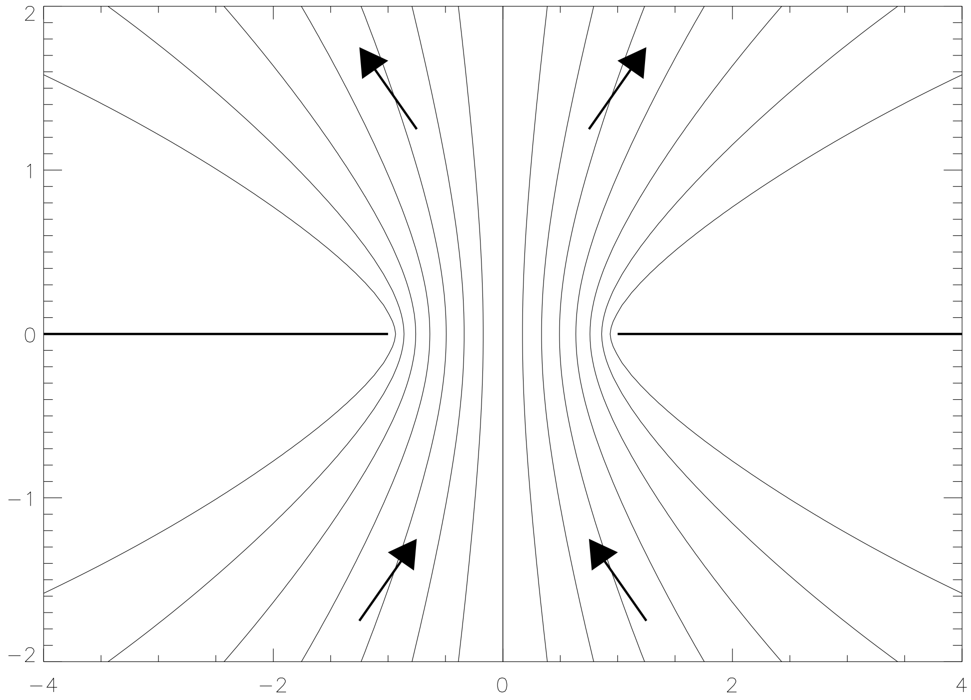

Figure 3.11: Same as Fig. 3.10 but $a = 10$.

and $\mathcal{F} = -1$. For $x < 0, y > 0$, the velocity induced on the vortex owing to the background flow and its self-advection along the wall are in the same direction, hence, vortices starting further away from the wall will pass through the gap more readily. For $x > 0, y < 0$, the background and vortex self-advection velocities are in opposite directions. Hence vortices are pushed back away from the gap by the background flow and need to be very close to the wall in order to generate sufficient speed from self-advection to overcome the background flux through the gap. The background flow is felt so strongly for $a = 0.5$ that it propels a vortex starting from $(4, 2)$ in the direction contrary to its regular propagation and forces it through the gap. Vortices starting at negative x are advected in the same direction as they would from regular propagation but due to the background flow, more vortices are allowed to pass through the gap. Note, in contrast with no background flow, no vortices are able to leap across the gap in the presence of a background flow.

For $a = 1$ in Fig. 3.13, the case is similar with vortices being forced towards the gap with $a = 1$. As stated before in regard to the streamlines, as a increases, the

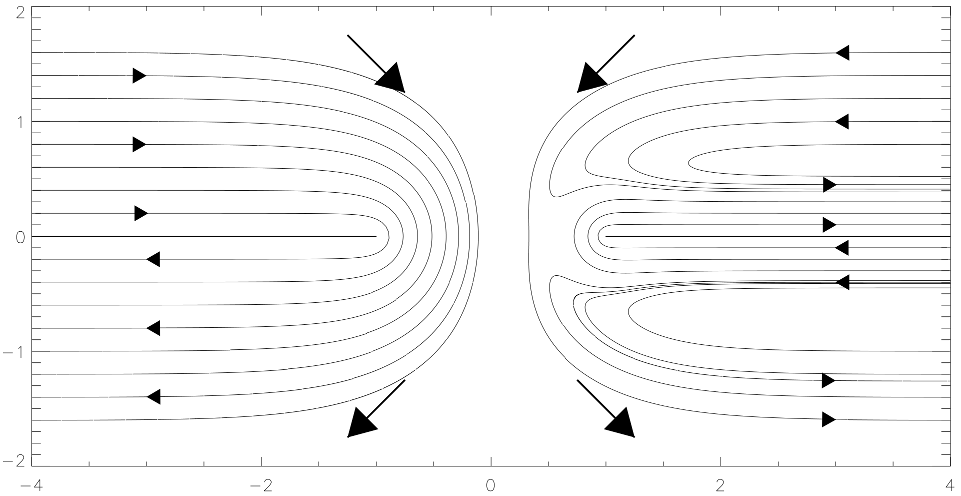

Figure 3.12: Vortex trajectories with $a = 0.5$ in the presence of a symmetric background flow, $\mathcal{F} = -1$. Large arrows indicate the direction of the background flow and small arrowheads indicate the direction of positive point vortices.

effect of the background flow decreases and a vortex starting from $(4, -0.6)$ crosses the gap. This trend is further exemplified by Fig. 3.14 where $a = 2$. The vortex path of the vortex starting from $(4, -0.6)$ crosses the gap closer to the gap, contrary to the direction of the background flow.

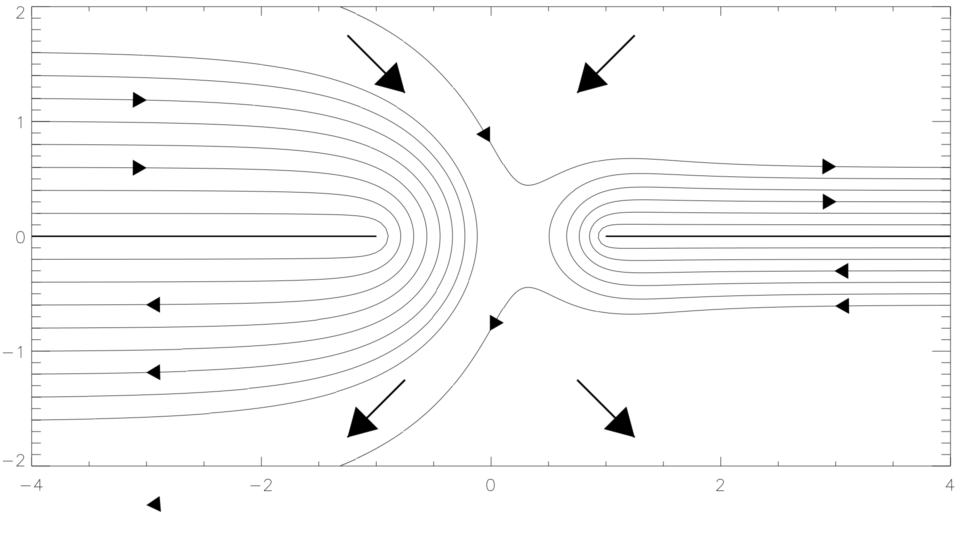

Figure 3.13: Same as in Fig. 3.12 but with $a = 1$.

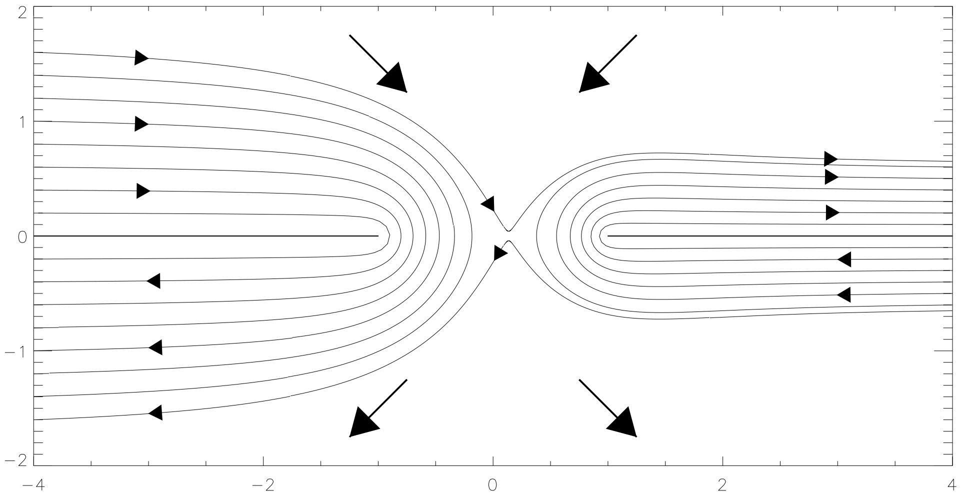

Figure 3.14: Same as in Fig. 3.13 but with $a = 2$.

3.4.2 Uniform anti-symmetric flow through the gap

Another non-trivial flow can be found by letting $\psi_a(x,0) = \mathcal{F}/2\pi, |x| > 1$, and insisting that away from the barriers, $\psi_a \to 0$ as $r \to \infty$. Note that the subscript a denotes anti-symmetric. This corresponds to zero net flux through the gap, i.e. the through-gap velocity is anti-symmetric about $x = 0$. This results in the following integral equation, for the vortex sheet strength $\lambda_a(x) = \partial\psi_a/\partial y$ on $|x| > 1, y = 0$,

$$\frac{\mathcal{F}}{2\pi} = 2\int_1^\infty \lambda_a(x)(H_a(x,0,x_0,0) + H_a(x,0,-x_0,0))\,\mathrm{d}x. \tag{3.31}$$

Interestingly, the anti-symmetric case is quite different for finite a from the rigid-lid ($a \to \infty$) case: as $a \to \infty, \psi_a \to \mathcal{F}/2\pi$ everywhere and the flow becomes stagnant. In principle any linear combination of ψ_a and ψ_s can be used to generate a non-trivial background flow. As in the previous section, the streamlines are plotted in Figs. 3.15- 3.18 for $a = 0.5, 1, 2$ and 10 respectively. The values of $\psi_s = (0.05 + n/10)/2\pi$ where $n = 0, \ldots, 9$ where $\psi_s = 1/2\pi$, where $\mathcal{F} = 1$ on both barriers. Note that in all the streamlines are contained within the domain for $a = 0.5$ but only the first three streamlines are present for $a = 10$. This is again due to the decrease decay of K_0 as a increases. The streamlines grow further apart as a increases.

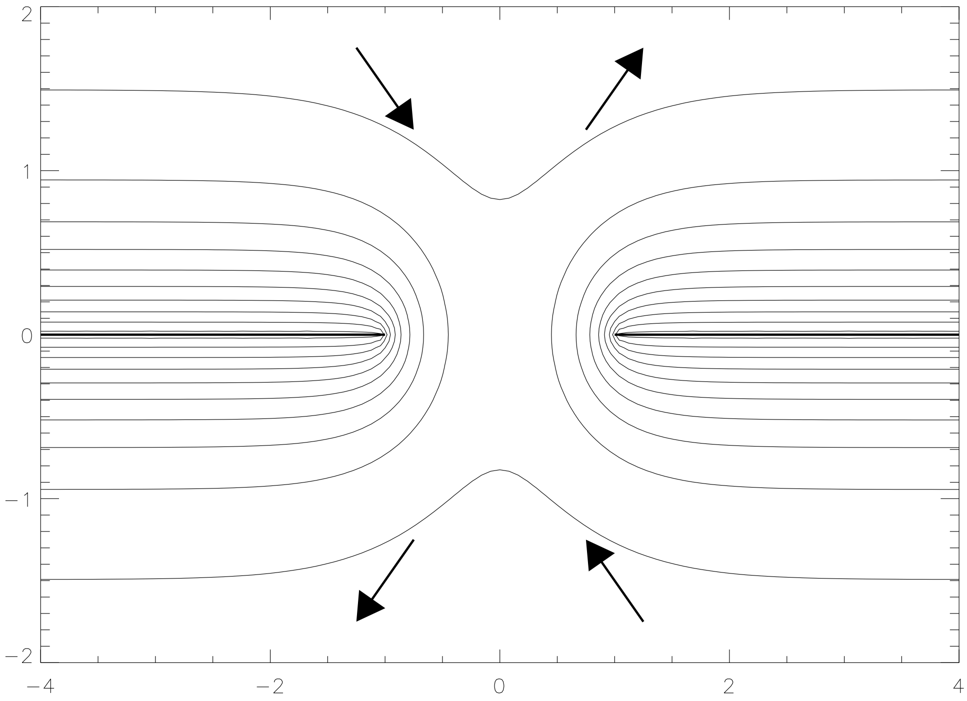

Figure 3.15: Streamlines of ψ_a plotted for $a = 0.5$. Large arrows indicate direction of the flow.

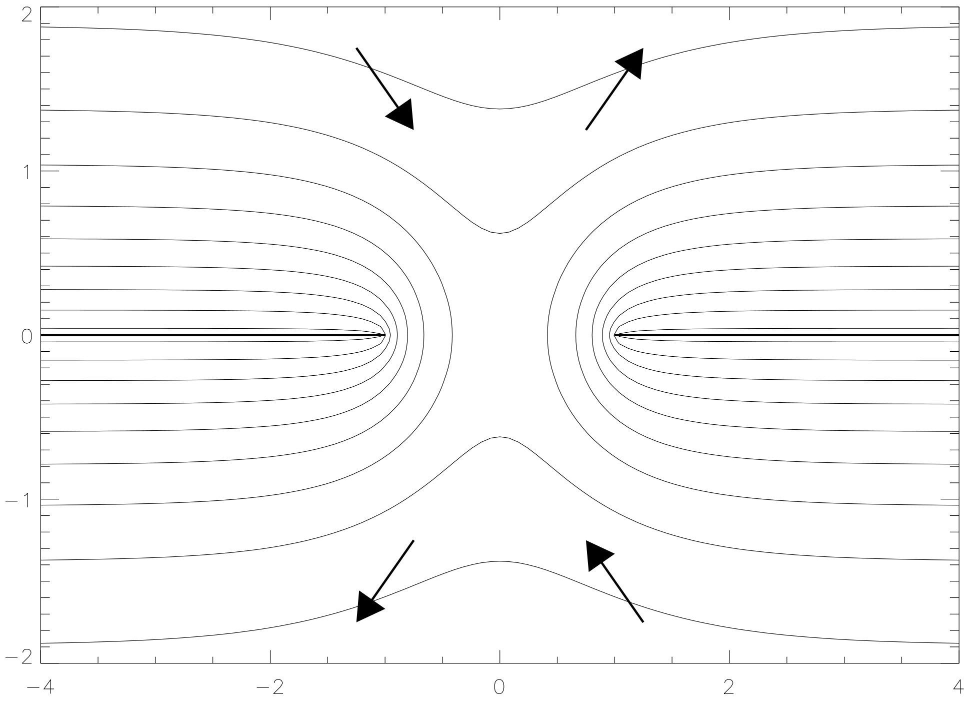

Figure 3.16: Same as Fig. 3.15 but $a = 1$.

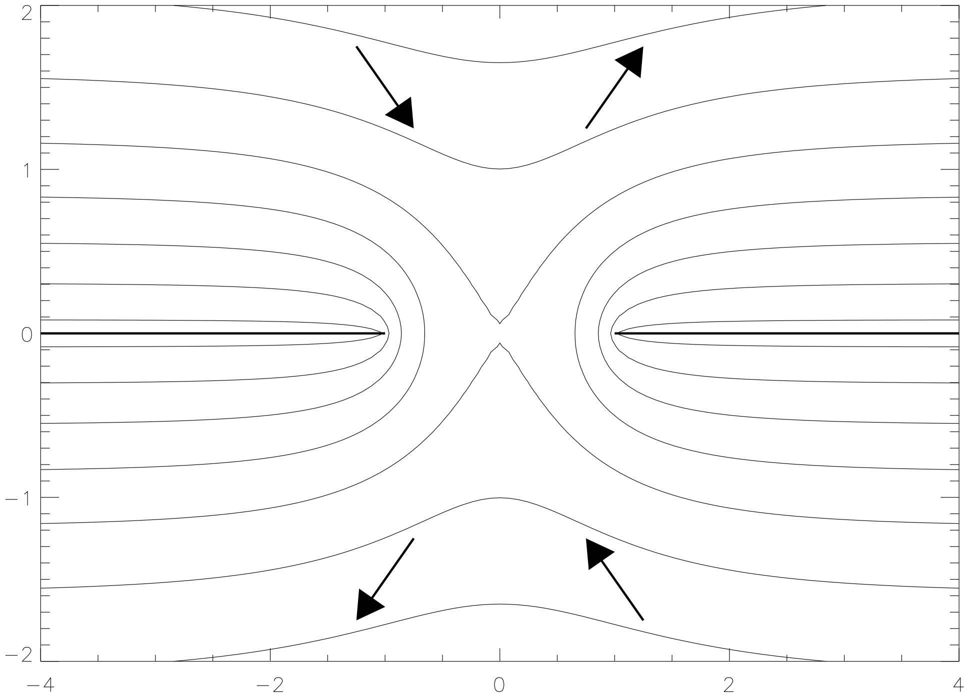

Figure 3.17: Same as Fig. 3.16 but $a = 2$. Note that the three smallest values of ψ_s are not represented as the contours are outside the region plotted.

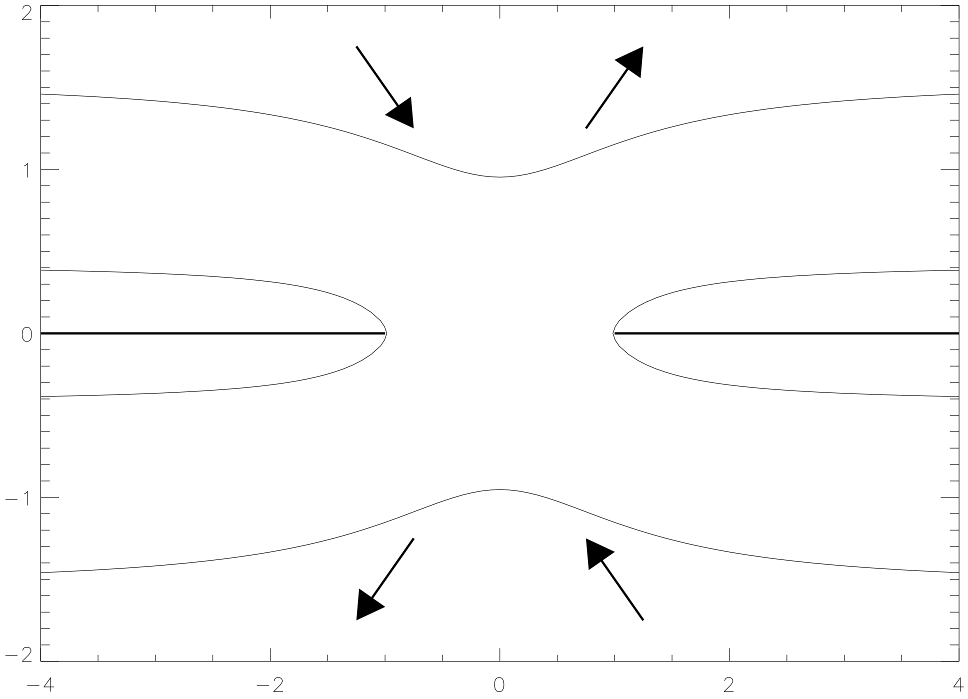

Figure 3.18: Same as Fig. 3.17 but $a = 10$. Fewer contours are present as the distance between contours increases greatly. $\psi_a = 0.85, 0.95, 1$ are the only values visible on the grid. The flow is relatively weak.

In the presence of anti-symmetric background flows there exist a variety of vortex behaviours depending on the flow strength $\mathcal{F}$. For example, there exist closed trajectories where vortices remain locally trapped (see Fig. 3.19). For $\mathcal{F} = -0.6$ (Fig. 3.19(a)), there are four primary regions within the flow: the hour glass shape which contains a region of trapped vortex paths. There are also three stagnation points on the y-axis including one which is unstable at the origin. For large $|x|$ some vortices approach the gap but are turned back, travelling back towards their initial position owing to the background flow. Note that vortices sufficiently far from the barrier also propagate against the direction of self advection owing to the background flow.

Gradually increasing the magnitude of the strength $\mathcal{F}$ squashes the hour glass so that its height (y-direction) decreases and its width (x-direction) increases as the two stable (elliptic) stagnation points on the $y-$axis coalesce. In Fig. 3.19(b) ($\mathcal{F} = -1$), the hour glass contains closed paths (with their semi-major axes lying on the y-axis). Interestingly the centre of the gap has gone from an unstable hyperbolic point Fig. 3.19(a) to an elliptic point Fig. 3.19(b). In Fig. 3.19(c), with stronger background flow ($\mathcal{F} = -1.4$), the centre of the gap is again hyperbolic and there are now two stable stagnation points on the $x-$axis. In Fig. 3.19(d), the strongest background flow ($\mathcal{F} = -1.6$), the hour glass is further squashed and the stagnation points are pushed further out towards the tips of the barriers.

When the background flow is cooperative, ($\mathcal{F} > 0$), a larger number of vortices pass through the gap. Fig. 3.20 shows that for vortices starting $x \to -\infty, y > 0$, y_{sep} increases with an increase in anti-symmetric flow strength.

The effect of changing a also influences the vortex path trajectories. As the effect of the background flow is felt less strongly as a increases, the magnitude of $\mathcal{F}$ must be increased to get results similar to those for small a.

In Fig. 3.21(a), $\mathcal{F} = -0.5$, the vortex trajectories starting far from the wall and away from the gap are advected in the opposite direction to regular (i.e. zero

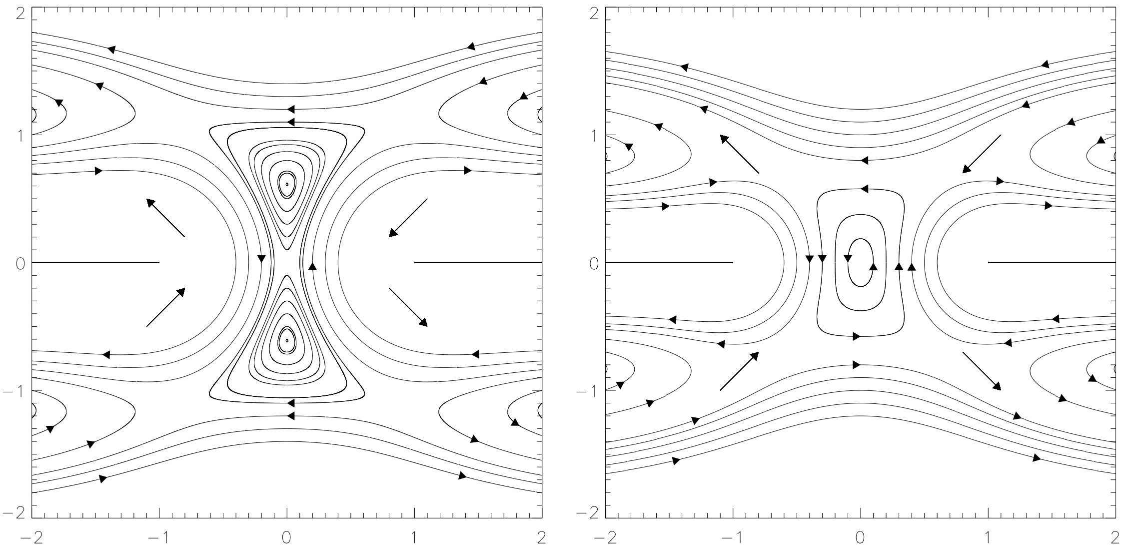

(a) $\mathcal{F} = -0.6$ (b) $\mathcal{F} = -1.$

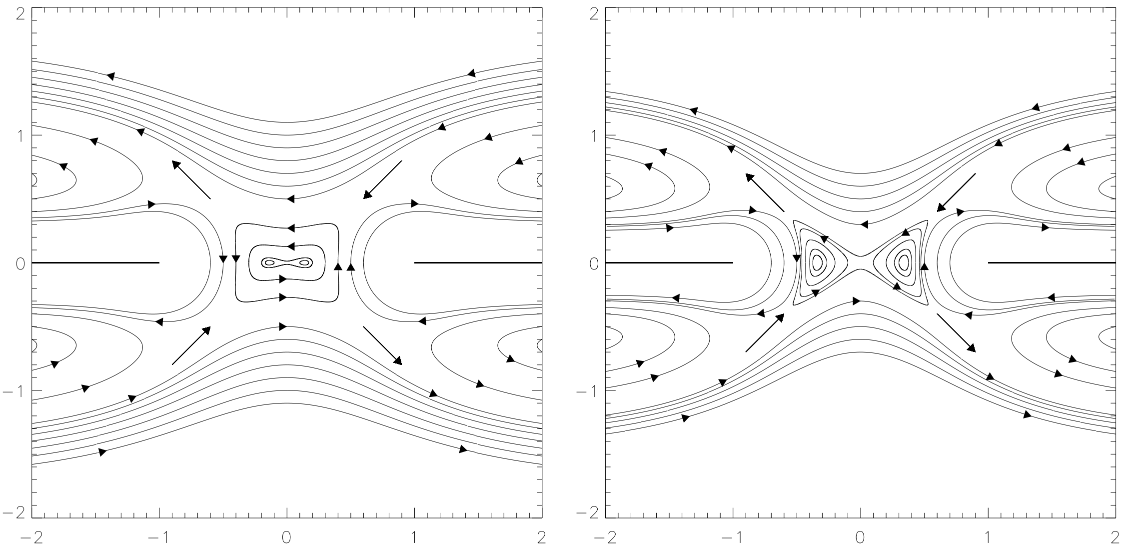

(c) $\mathcal{F} = -1.4$ (d) $\mathcal{F} = -1.6$

Figure 3.19: Vortex trajectories ($\Gamma = 1$) over a range of anti-symmetric flows. The strength of the flows in each figure is $-\mathcal{F} = 0.6, 1, 1.4, 1.6$ in (a,b,c,d) respectively. The large straight arrows indicate the direction of the the background velocity field. Arrow-heads on the trajectories indicate the direction of vortex propagation.

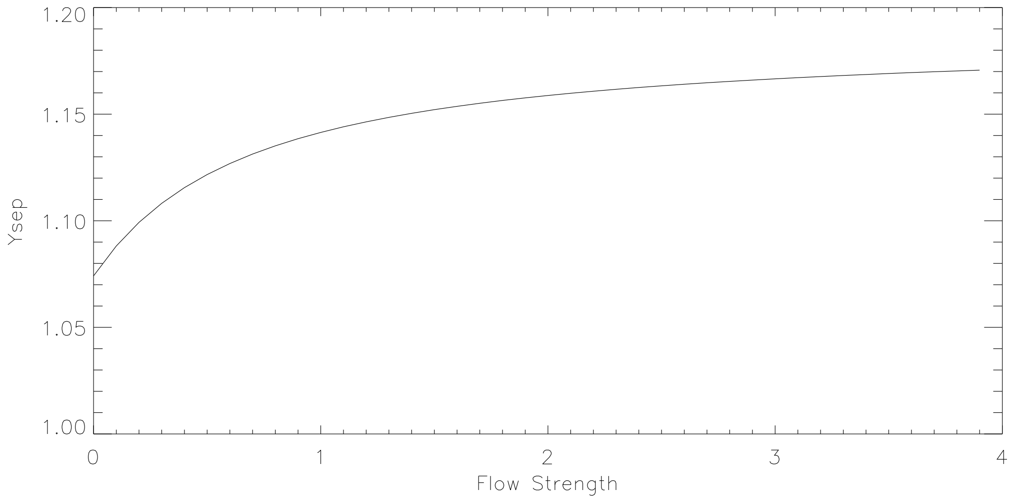

Figure 3.20: Value of y_{sep} as a function of the strength $\mathcal{F}$ of anti-symmetric flow for $a = 1$.

background flow) vortex motion. This is because the background flow strength is felt relatively strongly. Vortices close to the wall do cross the gap as the vortex self-advection is stronger. There are two stagnation points present along the gap within the trapped vortex paths. In Fig. 3.21(b), $\mathcal{F} = -0.5$ but the vortex paths are similar to the zero background flow case.

Fig. 3.22, $\mathcal{F} = -2$ with $a = 1$ in (a) and $a = 2$ in (b). Again, the effect on the vortex trajectories is stronger for the smaller a with vortices going against their self-propagation direction in Fig. 3.22(a), however, the effect of the trajectories for $a = 2$ in Fig. 3.22(b) is similar to that of Fig. 3.19(a).

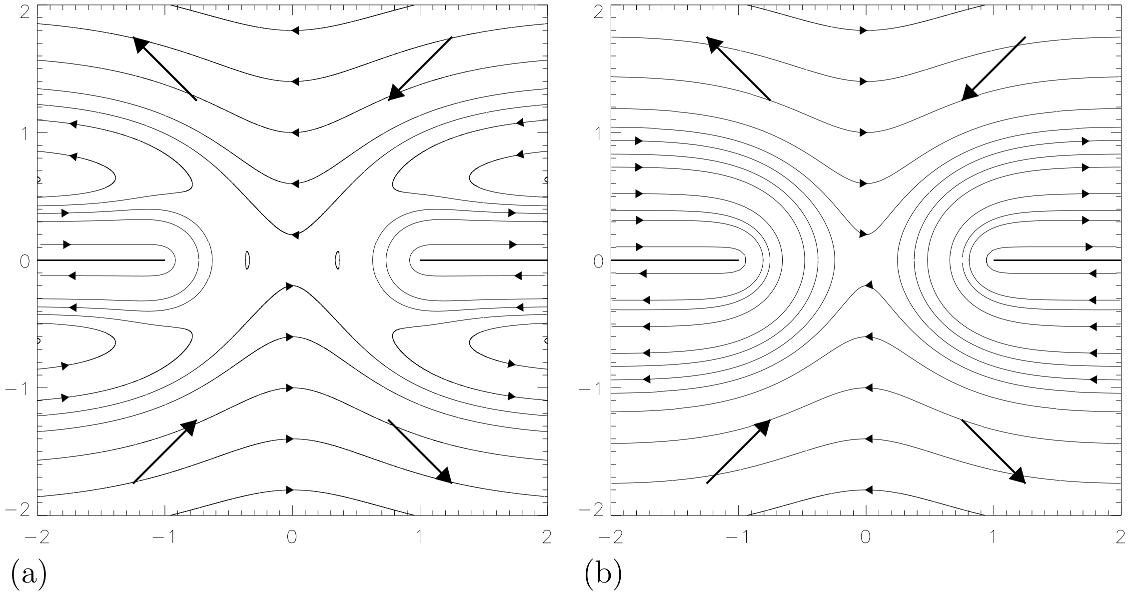

Figure 3.21: $\mathcal{F} = -0.5$. (a) Vortices are propelled in the opposite direction to their normal propagation near the gap for $a = 0.5$. (b) Vortex behaviour is similar to that seen in the absence of background flow for $a = 2$.

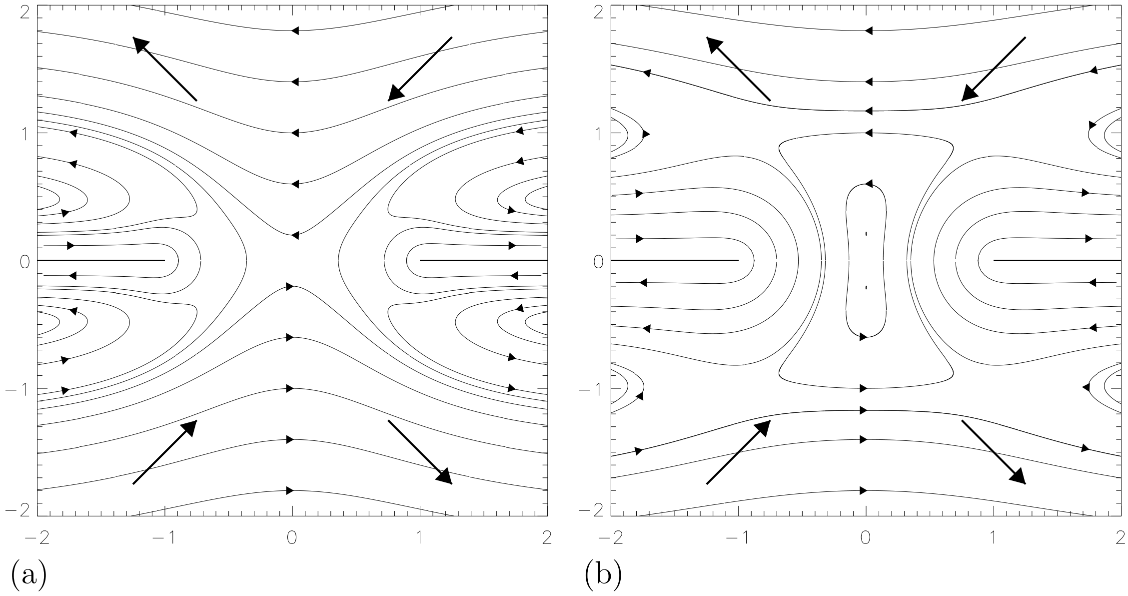

Figure 3.22: $\mathcal{F} = -2$. (a) Vortices are propelled by the background flow in the opposite direction to their propagation near the gap for $a = 1$. (b) Vortex behaviour is similar to that seen in Fig. 3.19(a) for $a = 2$.

3.5 Summary

An integral equation (using vortex sheets aligned with the semi-infinite barriers) has been solved by approximating it as a system of linear equations and solving using matrix inversion techniques. The method does not rely on iterating about the $a = \infty$ exact solution and is hence valid for $a < \mathrm{O}(1)$.

This method yields vortex trajectories which show good agreement (with the iterative method) over a range of $a \geq 1$. The separatrix (that divides leaping-across and gap-penetrating trajectories) is also computed by starting the point vortex near the gap and advecting the vortex backwards in time until the vortex moves parallel to the wall (i.e. behaving as it would near a wall without a gap). The results show clearly that decreasing a increases the tendency of the vortex to the pass through the gap.

The inclusion of background flows was done using the same numerical method. Uniform symmetric and anti-symmetric background flows were considered, giving interesting results. For the uniform symmetric case, if the background flow was such that it opposed the point vortex velocity with zero background flow, it decreased the number of vortices able to pass through the gap, with the converse being true for a cooperative background flow. The anti-symmetric background flow (which has no analogy in the rigid-lid limit) was also of interest due to the presence of trapped vortex paths when the background flow locally opposed the natural direction of the point vortex's self-advection. When the background flow is in the same direction as the point vortex path, this increases the number of vortices that are able to pass through the gap.

In the next chapter, this numerical method is incorporated into the contour dynamics code so that the effects of the Rossby radius of deformation on the motion of finite-area patches near a gap can be examined.

Chapter 4

Finite area patch vortex motion near a gap in a wall

Contour dynamics enables the motion of a finite-area patch of vorticity to be calculated efficiently by advecting the boundary of the vortex patch. The contour dynamics algorithm, in conjunction with contour surgery (as developed by Dritschel 1989) which allows for the breaking and joining of contours, is modified to include the gap geometry.

The normal velocity along the barriers owing to a piece-wise constant distribution of vorticity (i.e. the vortex "patches") is calculated using the contour dynamics algorithm. In the same way that we treated point vortices, the normal velocity is split into even and odd parts. The barrier is discretized over the interval $1 \leqslant x \leqslant 13a$, which is the same as the point vortex case (see Section 3.2). The resulting even and odd velocity fields along the barrier help us to solve the resultant integral equations for the respective streamfunction derivatives ($\lambda_{1,2}(x)$). We do this by using the same method described in Chapter 3 for the point vortex case. Once obtained, the velocity owing to the vortex sheets (aligned along the barriers) is calculated at each node on the contour. This velocity, along with the self-induced patch velocity (computed in a standard way by contour dynamics) is then used to advect the nodes on the vortex patch boundary. This is achieved using a fourth-order Runge-Kutta routine with a time step $\Delta t = 0.1$.

4.1 Vortex patch normalisation

This section derives a new way of normalising finite-area vortex patches. The normalisation factor incorporates the parameter a and is defined so that point vortices can be made to travel at the same velocity as a circular vortex patch of an arbitrary size.

First, we derive a preliminary result for the general solution of the Helmholtz equation,

$$\nabla^2\psi - \frac{1}{a^2}\psi = 0, \tag{4.1}$$

with arbitrary boundary conditions on the circle, $r = R$. The solution can be written for $r < R$ as

$$\psi = \sum_{n=0}^{\infty}(\alpha_n \cos n\theta + \beta_n \sin n\theta) I_n(r/a). \tag{4.2}$$

The area-average value of ψ inside a circular vortex patch is, using (4.2), proportional to α_0, the value of ψ at the centre of the patch:

$$\langle\psi\rangle = \frac{1}{\pi R^2}\int_0^R \int_0^{2\pi} \psi r \,\mathrm{d}r\,\mathrm{d}\theta = 2\frac{\alpha_0}{R^2}\int_0^R I_0(r/a) r\,\mathrm{d}r = \alpha_0 \mathcal{S} \tag{4.3}$$

where

$$\mathcal{S} = \frac{2a}{R} I_1(R/a). \tag{4.4}$$

Note $\mathcal{S}$ increases monotonically from unity (the rigid-lid or $a \to \infty$ limit) with increasing R/a.

The x coordinate of the potential vorticity centroid of a finite area patch can be written for a non-constant potential vorticity $q(x, y)$ as $x_c = \int xq/\mathcal{Q}$ where $\mathcal{Q} = \int q$ is the total potential vorticity inside the vortex patch, and all integrals are evaluated over the area of the patch. Conservation of potential vorticity q shows that $\mathcal{Q}$ is a constant of the motion and hence,

$$\mathcal{Q}\dot{x}_c = \iint x\dot{q} = -\iint x \cdot \nabla(\mathbf{u}q) = \iint q\mathbf{u} \cdot \nabla x - \nabla \cdot (x\mathbf{u}q)\,. \tag{4.5}$$

The divergence term is reduced to a line integral around the boundary of the patch, which for a finite patch, vanishes. The first term remains which is just the area integral of the x component of the velocity, u, multiplied by q. This is written as $u = u_v + u_e$ where u_v is the irrotational velocity induced on the patch in isolation (i.e. from the infinite domain Green's function) and u_e is the rotational velocity induced from external sources such as images in boundaries, vortex sheets or superposed irrotational background flows. The usual manipulations of the conservation of impulse show (Saffman 1992) that u_v makes no contribution to the integral and therefore,

$$\dot{x}_c = \iint u_e q/\mathcal{Q}, \tag{4.6}$$

which, for a patch of constant potential vorticity $q = q_0$, becomes

$$\dot{x}_c = \langle u_e \rangle, \tag{4.7}$$

that is, the simple patch-area average velocity of u_e. As u_e is the derivative of some streamfunction ψ and so satisfies Helmholtz's equation over the patch, by (4.3) we have,

$$\dot{x}_c = \mathcal{S}u_e(x_c, y_c). \tag{4.8}$$

The analogous results hold for the y coordinate of the centroid y_c and thus the velocity of the patch centroid is $\mathcal{S}(u_e, v_e) = \mathcal{S}\mathbf{u}_e(x_c, y_c)$, i.e. the same velocity field as felt by a point vortex at (x_c, y_c) but multiplied by the factor $\mathcal{S}$. Note also that the external fields, independent of the potential vorticity anomaly, must also be scaled via the parameter $\mathcal{S}$.

The velocity $\mathbf{u_e}$ is still required. For a uniform potential vorticity, q_0, inside the vortex patch the jump in vorticity is

$$\nabla^2\psi - \frac{1}{a^2}\psi = \begin{cases} q_0 & r < R, \\ 0 & r > R. \end{cases} \tag{4.9}$$

Equation (4.9) has solution, with ψ constant and having continuous derivative along the patch boundary,

$$\psi/q_0 = \begin{cases} -a^2 - aRK_0'(R/a)I_0(r/a) & r < R \\ -aRI_0'(R/a)K_0(r/a) & r > R, \end{cases} \tag{4.10}$$

where the dashes indicate derivatives.

The field outside the patch ($r > R$) can be written,

$$\psi = \mathcal{S}(\mathcal{Q}/2\pi)K_0(r/a). \tag{4.11}$$

4.2 Normalisation results

Recall, (4.8), that the external field plus any imposed external field then induces a velocity field on a patch that scales with $\mathcal{S}$ so that the patch moves with velocity $\mathcal{S}\mathbf{u}_e(x_c, y_c)$. Hence, a point vortex can be made to move at the same speed near, say, a boundary as a circular patch of arbitrary radius R provided the circulation of the point vortex $\Gamma_n = S^2\mathcal{Q}$. As the rigid-lid approximation is approached, $a \to \infty$, $\Gamma_n \to \mathcal{Q}$, hence scaling directly with the circulation of the vortex. It is important to note that this 'usual' scaling with the vortex circulation only holds in the $a \to \infty$ limit, and that, more generally, the patch circulation must be scaled by $\mathcal{S}^2\mathcal{Q}$.

Fig. 4.1 shows results for the motion of individual patches with different areas

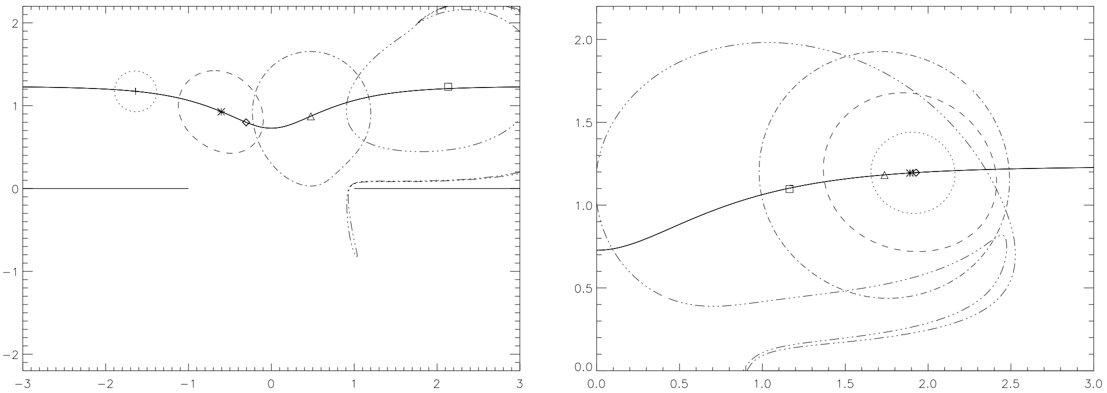

(a) (b)

Figure 4.1: The effect of various vortex patch normalisations. (a) Snapshot at $t = 28.8$ for the motion of a point vortex ($\Diamond$) and circular vortex patches of radius, $R = 0.25, 0.5, 0.75, 1$ with centroids denoted by $(+, *, \triangle, \Box)$, respectively. Here $a = 10, q = 1$ and patch centroids are initially located at $(-2, 1.2)$. Circulation of the point vortex is $\Gamma = 1$. The solid line indicates the trajectory of a point vortex. (b) same as in (a) but zoomed in to focus on the centroids and with q scaled by the patch size so that $\Gamma = q\pi R^2 = 1$ for all patches.

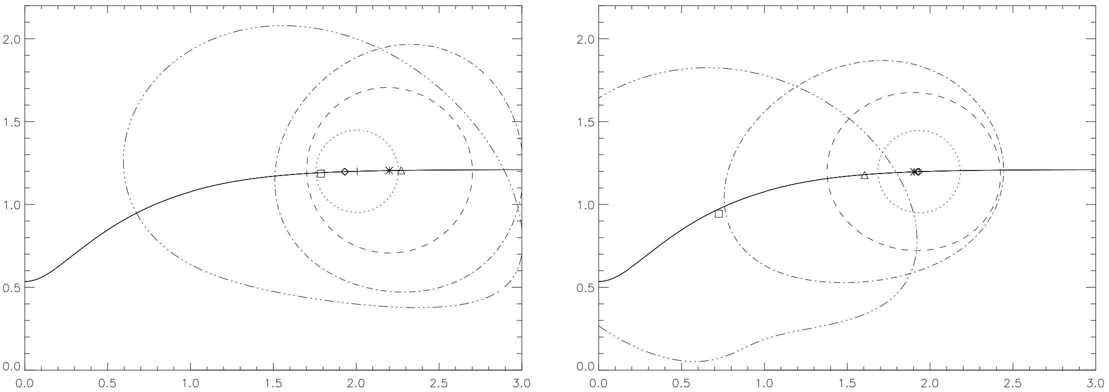

(a) (b)

Figure 4.2: (a) Same as in Fig. 4.1(b) but with $a = 1$ and snapshot taken at $t = 350$. Note the non-systematic spacing of the patch centroids. (b) Same as in (a) but with vorticity, q, scaled so that $S^2\mathcal{Q} = 1$. Here vortices which remain close to circular travel at the same speed as a point vortex with strength $\Gamma = 1$.

moving near a gap in the absence of a background flow field with $a = 10$. As can be seen in Fig. 4.1(a), with non-normalised flows with $q = 1$, the larger patches travel faster than smaller patches. Note that patches of area $\pi R^2 < 1$ with $R = 0.25$ and $R = 0.5$ travel slower than a point vortex of strength $\Gamma = 1$ whereas patches with area $\pi R^2 > 1$ with $R = 0.75$ and $R = 1$ travel faster. The largest patch deforms significantly due to the presence of the downstream barrier and begins to shed vorticity causing its centroid to deviate from the equivalent point vortex trajectory. For $a = 10$, each patch's velocity can be normalised with the circulation of the patches, as seen in Fig. 4.1(b) . The largest patch does slow down considerably due to its interaction with the barrier causing it to become non-circular.

For $a = 1$, using the 'usual' circulation based scaling, shows that the difference of the patch speed from the point vortex speed is significant (see Fig. 4.2(a)). In particular this difference is not systematic as R varies, with $R = 0.75$, having the greatest translation speed. Instead, Fig 4.2(b) has its vorticity q scaled such that $\mathcal{S}^2\mathcal{Q} = 1$ for all patches. This new scaling shows that there is a systematic variation of patch speed from the point vortex speed as R varies, i.e. the smaller the radius of the patch, the closer the speed to the point vortex. For patches which remain close to circular throughout their evolution there is very good agreement in both their trajectories and speed.

4.2.1 Vortex patch motion: Background flows

Similarly, the effect of background flows can be scaled so that vortex patches of varying size follow the point vortex trajectories with the same speed. In Fig. 4.3 the uniform symmetric flux through the gap advects the vortex patches in the positive y direction. Here $a = 1$ and the background flow has been scaled by the factor $\mathcal{S}$.

For a positive vorticity patch with the flux reversed, the background flow forces the patch closer to the gap– see Fig. 4.4. Owing to the significant deformation of the larger patches there is some observable but small change in patch speed in

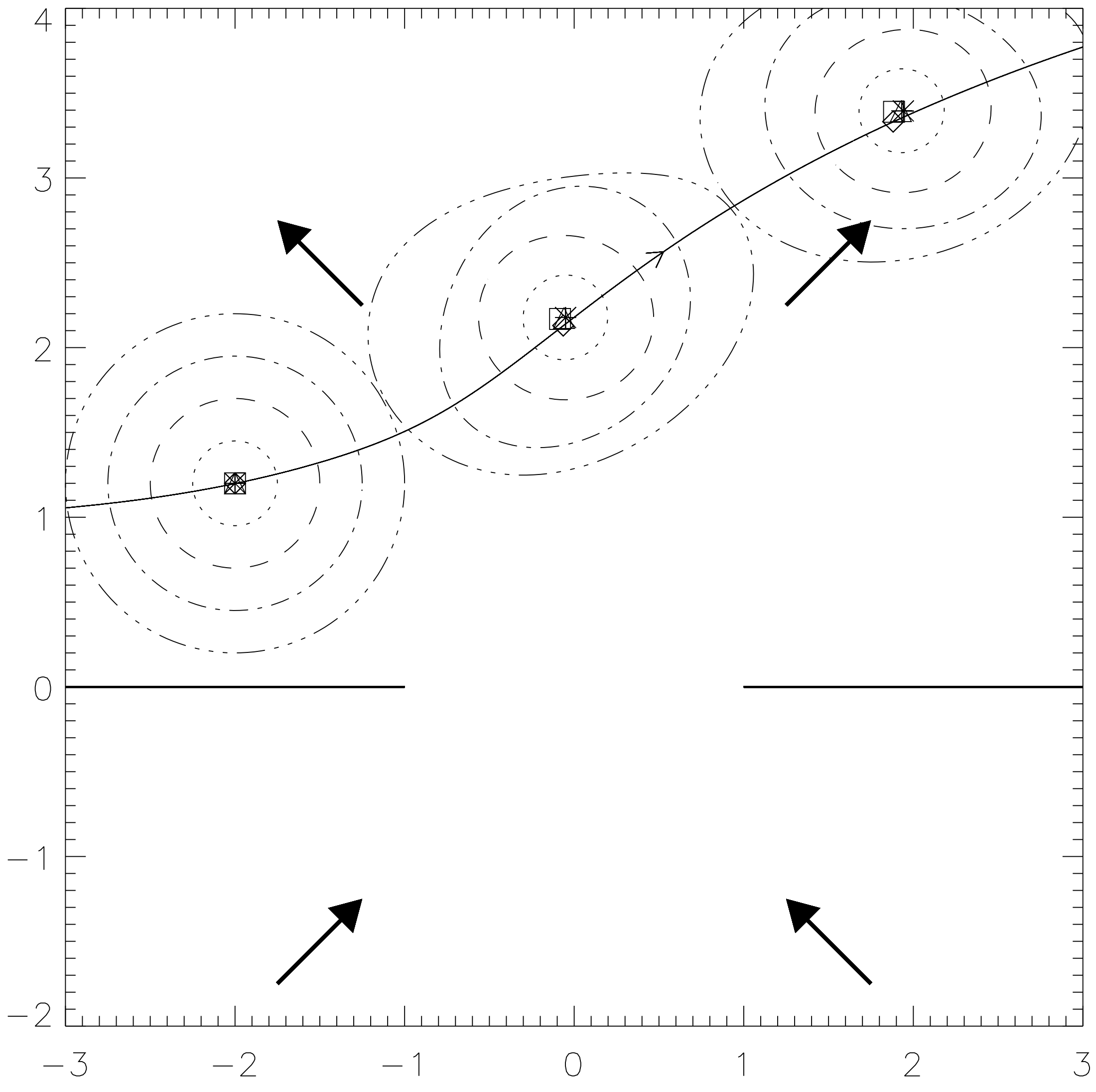

Figure 4.3: Motion of patches of varying size in a normalised uniform symmetric flow through the gap with $\mathcal{F} = 1/\mathcal{S}$. Large arrows indicate the direction of the normalised background flow. Initially, the centroid location of the normalised patches and the point vortex is $(-2, 1)$, with the centroids denoted in the same way as in Fig. 4.1. Snapshots taken at $t = 0, 61.6, 140$ and $a = 1$. Centroids are indicated by $(+, *, \triangle, \square)$ symbols.

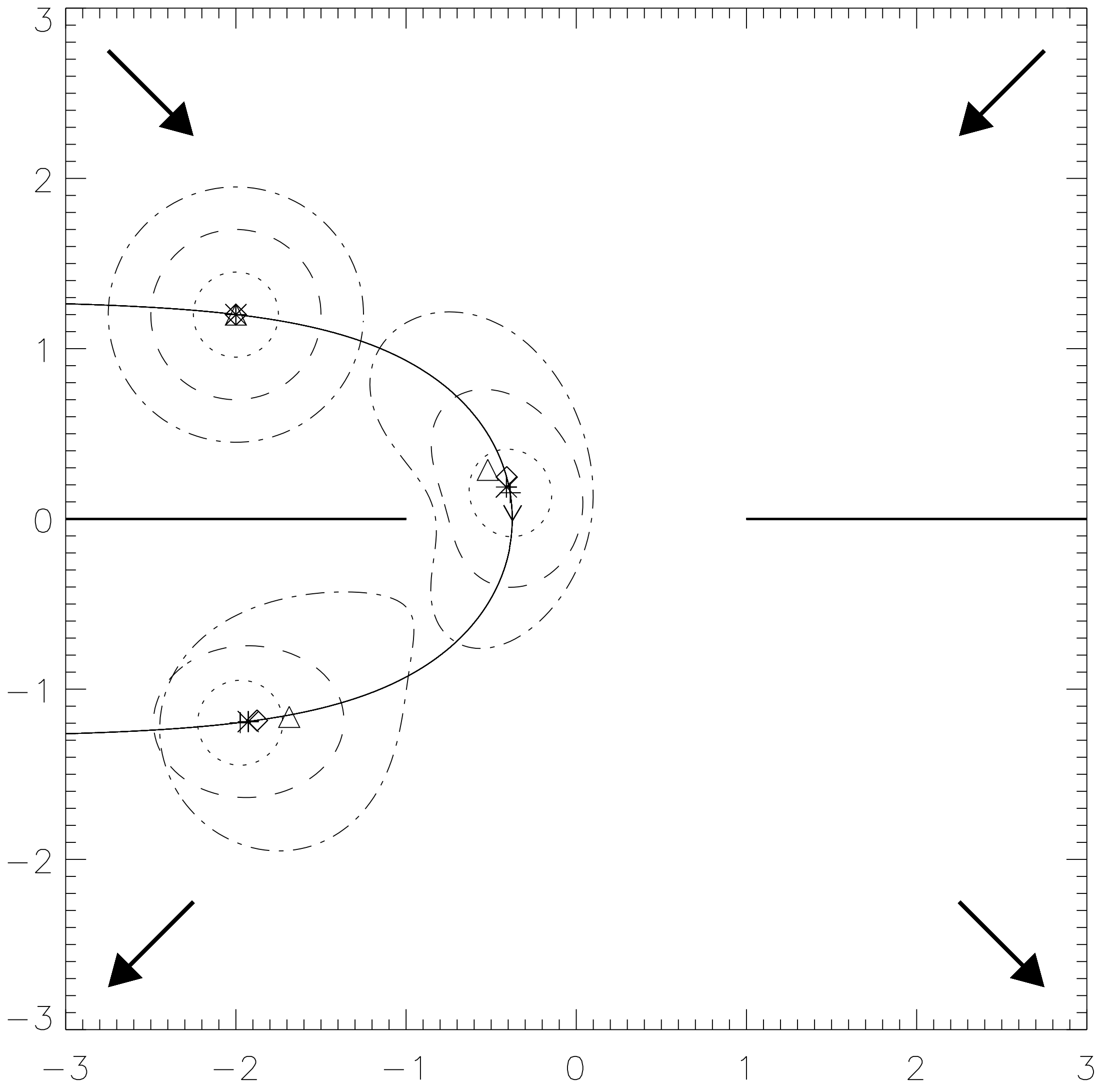

Figure 4.4: Same as Fig. 4.3 but with $\mathcal{F} = -1/\mathcal{S}$. The large arrows indicate the direction of the background flow. Snapshots taken at $t = 0, 40.8, 80$.

comparison to that of a point vortex.

Unlike for a point vortex, the anti-symmetric flux through the gap can result in large deformation of the patch. For example Fig. 4.5 shows a vortex patch approaching the centre of the gap where the background flow is strongly sheared causing the vortex to split.

Using the trapped point vortex paths from the previous chapter, the motion of the centroid is also trapped in the same region for different sized vortex patches, as can be seen in Fig. 4.6. The point vortex path is dotted and vortex patches are advected with initial centroid location $(0, .2)$. Here, as the vortex patches stay roughly similar, the centroid of the patches moves at the same speed although there are some changes to the largest vortex patch, it also follows the numerical trajectory of the point vortex as it is still roughly circular.

4.3 Summary

The method of contour dynamics has been adapted for gap geometry with a finite Rossby radius. Furthermore a normalisation is developed such that a point vortex can travel at the same speed and trajectory as a circular vortex patch of arbitrary radius as a function of a. The inclusion of background flows has also been considered and the results show good agreement between equivalent point vortex and patches provided the patches remain circular.

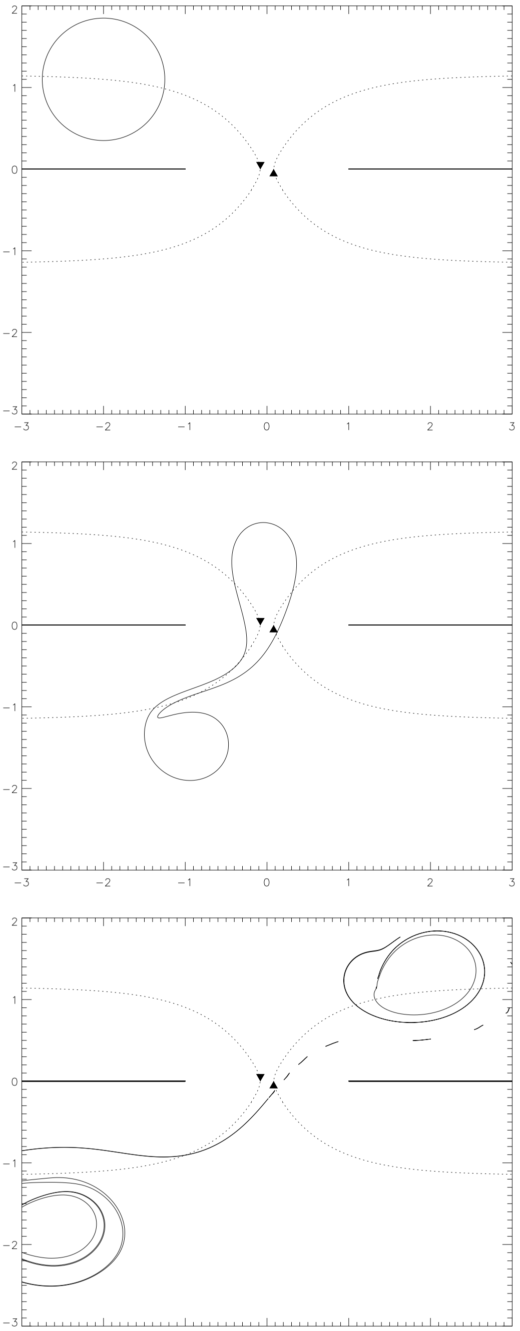

Figure 4.5: Motion of a patch (initially circular with radius $R = .75$) in an anti-symmetric background flow through the gap of strength, $\mathcal{F} = 2/\mathcal{S}$ for $a = 1$. The strong shear forces the patch to split when close to the centre of the gap. Note the solid line shows the point vortex trajectory starting at the same location as the patch. Snapshots taken at $t = 0, 70, 108.5$.

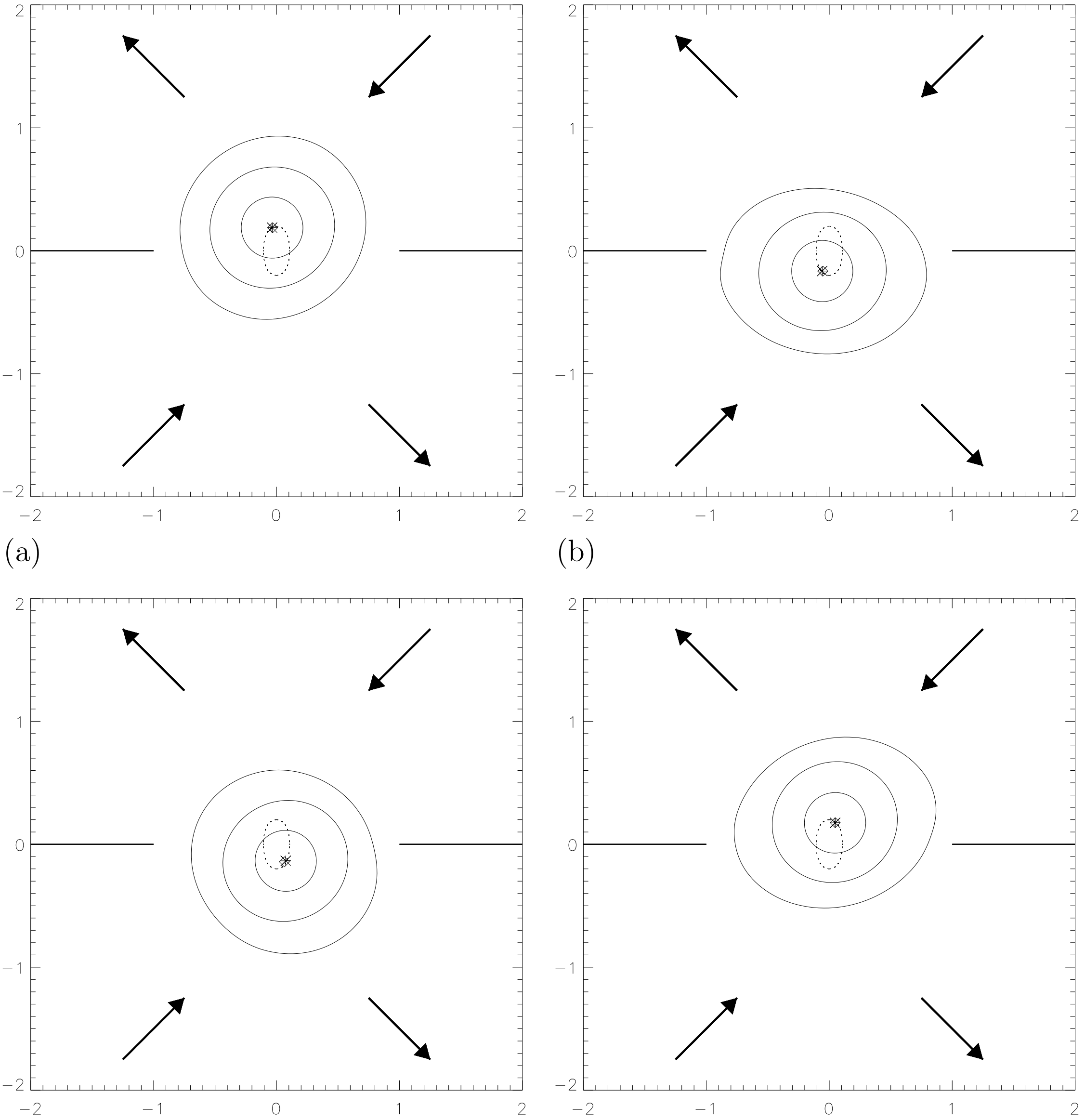

(a) (b)

(c) (d)

Figure 4.6: Motion of a patch (initially circular with radius $R = 0.25, 0.5, 0.75$) with an anti-symmetric background flow through the gap of strength, $\mathcal{F} = -1/\mathcal{S}$ for $a = 1$. The arrows indicate the direction of the background flow. The background flow opposes the natural direction of propagation of the vortex and hence becomes trapped as is the case with the point vortex. The dotted line shows the point vortex trajectory starting at the same initial location as the patch. Snapshots taken at $t = 80, 320, 480, 680$.

Chapter 5

Rossby radius effects on steadily translating vortex pairs

5.1 Introduction

Distributions of vorticity that preserve their shape when propagating near boundaries, in variable topography or in the presence of other vortical structures have been a subject of interest in the literature. These equilibrium distributions represent exact solutions to the two dimensional barotropic quasigeostrophic equations (the rigid-lid limit of which is equivalent to the Euler equations). The vorticity distribution is said to be a V-state if there exists a frame of reference where the vortical structure is invariant. Such structures are frequently stable and thus represent persistent long-lived solutions of the equations of motion and, therefore, merit study. Configurations of point vortices yield some simple examples. A pair of counter-rotating point vortices of strengths $\pm\kappa$ respectively, separated by a distance h in a rigid-lid ($a \to \infty$) fluid travel at constant velocity $\kappa/2\pi h$ in the direction normal to the line segment between the two vortices. Conversely, vortices with equal strength, κ, rotate about the centre of the line segment connecting them with constant angular velocity $\kappa/\pi h^2$. Furthermore, a pair of co-rotating vortices will move in concentric circles.

The three point vortex problem (again in the rigid-lid limit, $L_d \to \infty$) has been well researched in the past, (see Aref 2003). For fixed equilibrium (i.e. each vortex is stationary), the condition required is that the three vortices must be collinear and such that

$$(\mathbf{x}_2 - \mathbf{x}_1) = \frac{\kappa_2}{\kappa_3}(\mathbf{x}_1 - \mathbf{x}_3), \tag{5.1}$$

and

$$\kappa_3 = -\frac{\kappa_1\kappa_2}{\kappa_2 + \kappa_1}, \tag{5.2}$$

where $\mathbf{x}_{1,2,3}$ are the locations of the three vortices and $\kappa_{1,2,3}$ are the respective vortex strengths. If the vortices have equal strength, and are located on the vertices of an equilateral triangle, there is relative equilibrium, in which each vortex has the same angular velocity about the centroid of the triangle. In fact, Kelvin (1878) and Thompson (1883) showed that for any regular polygon with identical vortices located on vertices, relative equilibrium exists in which the whole structure rotates with constant angular velocity $\kappa(N-1)/4\pi r^2$, where r is the radius of the circle on which the vertices lie. Perturbing the system by moving the n^{th} vortex, Saffman (1992) showed that for $N < 7$, the system is linearly stable but for for $N \geq 7$, the system is unstable.

An infinite row of equidistant point vortices of equal strength, κ are also stationary. If the point vortices (with $L_d \to \infty$) are located on the $x-$axis at $x = md$, where $m = 0, \pm 1, \pm 2, \ldots$, it has been shown by Lamb (1932) that the complex potential for such a system is $w = \mathrm{i}\kappa/2\pi \log(\cos(\pi z/d))$. Thus, at the point vortex at $x = md$, the velocity field, $u - \mathrm{i}v = dw/dz$, can be shown to be exactly zero, i.e. all vortices are stationary. Lamb also showed that for small disturbances the system is unstable. The double row problem, also considered by Lamb (1932), in which a second row of oppositely signed vortices is aligned parallel to the first row is also an equilibrium configuration. In this case, the whole system advances with constant velocity, $U = \kappa/2d \coth \pi c/d$, where c is the distance between rows and d is the distance between successive vortices within a row. This system was also shown to be unstable for small disturbances.

The double row of staggered line vortices, such that the vortices in each row are opposite the centre of two successive vortices in the other row, was studied by von Kármán and Rubach (1913) and is of particular interest since the configuration models the trail of vortices shed in the wake of a cylindrical body advancing through a fluid. Lamb (1932) showed that the double row staggered line vortex configuration propagates with velocity $V = \kappa \tanh(\pi c/d)/2d$, where c is the normal distance between the two rows and d is the distance within a row. This configuration was shown to be stable to small disturbances. The addition of a lateral rigid boundary, such as a wall, equidistant from the medial line was discussed by Rosenhead (1929). It was found that within a channel (i.e. two parallel walls), the staggered double row was stable but only given a precise configuration relating the distance between vortices and the channel walls. The symmetrical double row configuration within channel geometry was shown to be unstable always.

Near obstacles, point vortex equilibria also exists. For example, the motion of a vortex of strength κ, located at an initial distance r_v from the centre of a cylinder with radius r_c is found to rotate around the cylinder at the same distance with a constant angular velocity of $\kappa r_c^2/2\pi r_v(r_v^2 - r_c^2)$.

Other models of vortical structures have been used to find relative equilibria in the rigid-lid limit. The steadily translating Lamb dipole (also known as a modon) is a circular vortex within which there is continuously varying vorticity. In three dimensions the work of Fraenkel (1970) and Norbury (1972) showed the theoretical existence of a one-parameter family of vortex rings of continuously varying vorticity. The family consisted of vortex structures ranging from the potential (free) vortex to Hill's spherical vortex as the mean core radius of the vortex increased. Norbury (1975) further showed that for the two dimensional case, such vortex pairs exist if the vorticity function is a locally continuous function of the streamfunction, i.e. $\nabla^2\psi = f(\psi)$. The von Kármán vortex street has also been studied by Saffman and Schatzman ((1982*a*),(1982*b*)) using an inviscid model of finite core vortices to investigate the effect of finite core size on the relation between aspect ratio (length/width) and vortex strength.

A series of recent papers by Crowdy (e.g. Crowdy 1999,2002) construct exact vortex equilibria which comprise point vortices in combination with patches of uniform vortices. These equilibria, which either rotate steadily or are completely stationary, are characterised by having zero net circulation.

For the case of uniform (constant) vorticity pairs (with opposite signed vorticity), Deem and Zabusky (1978) numerically found a family of steadily translating solutions, which they called 'translating V-states'. Equivalently these solutions represent a family of patches propagating parallel to an infinite wall. Indeed this was one of the first uses of the numerical method we now know as contour dynamics. The properties associated with these vortex structures and a description of their shape was obtained by Pierrehumbert (1980) using a relaxation algorithm. He calculated the family of V-states as a function of $\theta = r/x_c$, where r is the equivalent radius (i.e. area divided by half the perimeter) of each vortex and $2x_c$ is the distance between the centroids of the vortices. For small θ, the vortices remain nearly circular and propagate at the same speed as that of a pair of point vortices with equivalent circulation. As the size of the vortex increases, the vortex patches become considerably more deformed. The limiting case of two touching vortices (or, in the wall analogy, the vortex touches the wall) was examined numerically by Sadovski (1972) and later by Saffman and Tanveer (1982). Steady co-rotating pairs of vortex patches were also studied by Saffman and Szeto (1980), who solved the contour dynamics equations numerically.

McDonald (2004) investigated a new translating quasigeostrophic V-state, incorporating topography. Here, the motion of a pair of co-rotating point vortices near an escarpment was modelled. The relative vorticity distribution resulting from fluid crossing the escarpment causes a steady state to occur, in which the point vortices pair up with the constant vorticity patch and propagate parallel to the escarpment. The linear solution for small wave amplitudes was found analytically. The non-linear case was solved using contour dynamics with a unique equilibrium solution found. This was demonstrated to be unstable.

All the above studies are focused on the rigid-lid ($a \to \infty$) case. Yet, it is of interest from a geophysical perspective to investigate steady-state distributions of vorticity for arbitrary Rossby radius of deformation as these are likely to be persistent structures observable in the ocean and atmosphere.

This chapter determines the effect of varying the Rossby radius of deformation, on steadily translating counter-rotating vortex pairs (or, equivalently, a single patch near a wall) each having constant vorticity. Quasigeostrophic dynamics in a single layer of reduced gravity inviscid, incompressible fluid are assumed. The method of contour dynamics (Dritschel 1989) is used to calculate the velocities induced by the patches. A relaxation algorithm based on that of Pierrehumbert (1980) is then used to calculate the shape of structures.

The translational velocities of the vortex patch pairs are compared to the translational velocities of point vortex pairs with equivalent circulation,

$$\Gamma_{PV} = [\frac{2a}{R} I_1(R/a)]^2 \pi R^2, \tag{5.3}$$

located at the centroid of the patch, where R is the mean radius of the patch. There is good agreement for a range of patch sizes. When the patches are sufficiently small, decreasing the Rossby radius makes the steadily translating shapes more circular. However, when close to the wall, the effect of decreasing the Rossby radii results in patches deforming greatly, forming long slug-like shapes. These are shown to be stable using the time-dependent contour dynamics code (Dritschel 1989).

Background flows can also be imposed on the system resulting in a family of vortical shapes, ranging from the slug-like to the tear-drop in shape. The two background flows considered here are the positive and negative uniform flow parallel to the line of symmetry of the pair (or, equivalently, parallel to the wall). Again, point vortex pairs in a background flow can be made to travel at the same velocity as circular patches when the background flow strength is, $C = \frac{2a}{R} I_1(R/a)$. Pierrehumbert's (1980) algorithm is also modified to find the exact strength of background flow required to render a vortex patch stationary. Furthermore, these shapes are tested for stability by running them in a time-dependent contour dynamics code.

5.2 The barotropic quasigeostrophic equation

A single layer of reduced gravity fluid in a flat bottomed ocean of depth H is considered. In the quasigeostrophic limit, the potential vorticity q is conserved, i.e.

$$\frac{Dq}{Dt} = 0, \tag{5.4}$$

where,

$$q = \nabla^2 \psi - \frac{1}{L_d^2} \psi, \tag{5.5}$$

and L_d is the deformation radius.

The streamfunction, $\psi(x, y)$ is such that,

$$\mathbf{u} = \mathbf{k} \times \nabla \psi, \tag{5.6}$$

where the velocity field of the fluid is given by $\mathbf{u} = u\mathbf{i} + v\mathbf{j}$.

For steady motion the boundary of the vortex patches must be such that the streamfunction along the boundary has a constant value i.e. the patch boundary is a streamline. Equilibria are sought which travel at a constant speed perpendicular to the line segment between the centres of the counter-rotating vortex patches. The

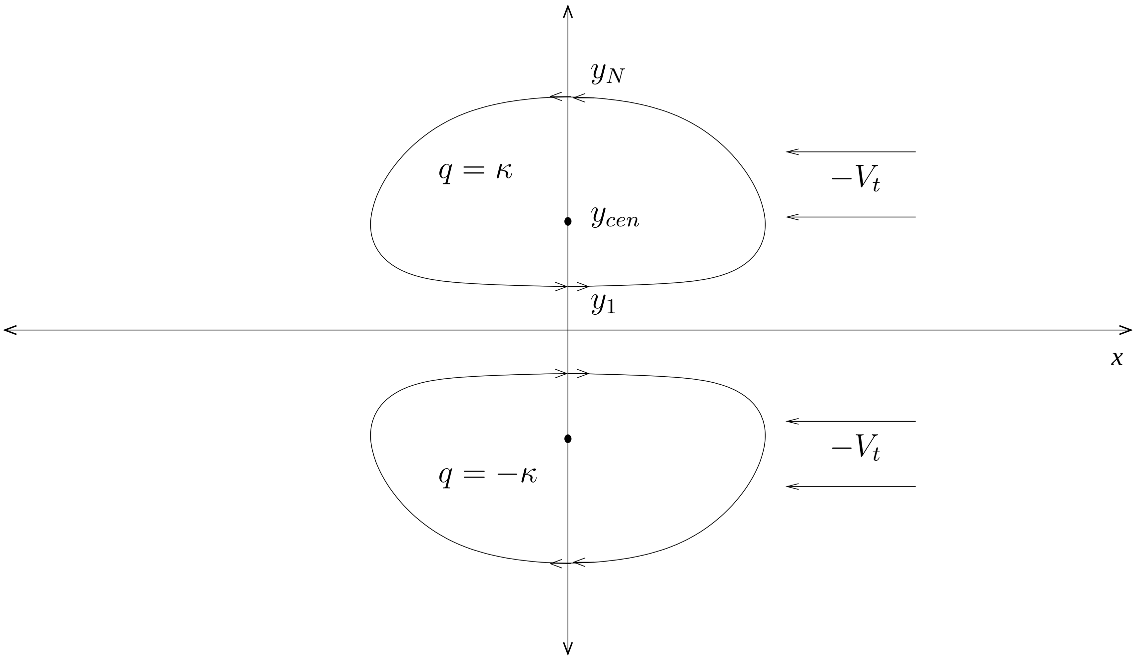

Figure 5.1: The counter-rotating vortex pair. The pair travels parallel to the $x-$axis. Arrows indicate the sense of circulation associated with each patch. V_t is the speed of the pair. Equivalently, the pair is stationary when a uniform flow of velocity $-V_t$ at infinity is imposed.

vortex pairs have mirror symmetry about the $x-$axis, each having equal and opposite vorticity (see Fig. 5.1).

As the velocity in the $y-$direction induced by the positive and negative vortices cancel each other out along the $x-$axis, there is a constant streamfunction along it, which can be set to zero. The system is therefore equivalent to a single vortex patch whose nearest edge is at a distance of y_1 from a wall along the $x-$axis. Exploiting this symmetry, all the plots herein will feature only the top vortex patch with the bottom vortex patch being referred as the image vortex.

The potential vorticity equation (5.5) is non-dimensionalised by choosing y_N as the length scale and $|\kappa|$ for the streamfunction, thus the point of the patch furthest from the wall is $y = 1$. Consequently y_1 must lie in the interval $0 < y_1 < 1$. The non-dimensional potential vorticity q' can thus be written as

$$q' = \nabla^2 \psi' - \frac{1}{a^2}\psi', \tag{5.7}$$

where

$$a = L_d / y_N. \tag{5.8}$$

For convenience the primed notation is removed.

5.3 Numerical method

5.3.1 Vortex patch discretization

The initial guess for the boundary of the vortex patch is taken to be a circle, symmetric about the $y-$axis. The half boundary is discretized into N points with the first and last points fixed, i.e.,

$$(x_1, y_1) = (0, y_1); (x_N, y_N) = (0, y_N), \tag{5.9}$$

where, $y_N = 1$ and y_1 are fixed. Let $(x_c, y_c) = (0, \frac{y_N + y_1}{2})$ be the centre of the circle.

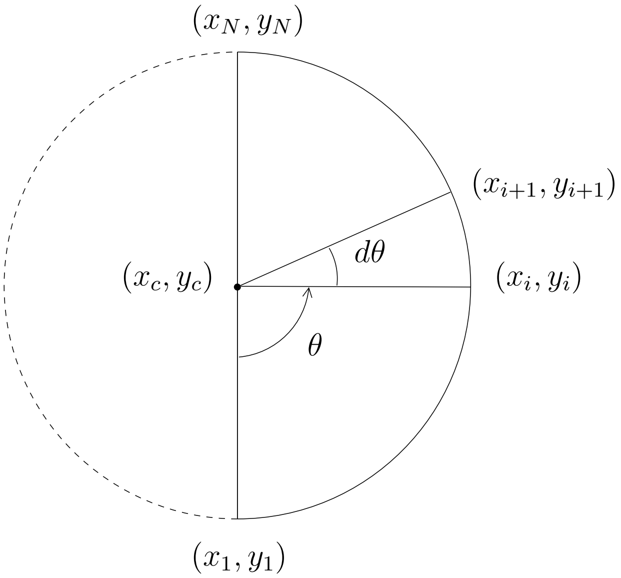

Figure 5.2: Initial circular vortex patch discretized about the centre by the angle θ_i.

The patch is discretized uniformly in the angular direction about its centre using

$\theta_i = (i-1)\pi/N$ such that (see Fig. 5.2), for $i = 1, \ldots, N$

$$x_i = R\cos(\theta_i - \pi/2), \tag{5.10}$$

$$y_i = y_c + R\sin(\theta_i - \pi/2), \tag{5.11}$$

where $R = \frac{y_N - y_1}{2}$ is the initial radius of circular patch and y_c is the centroid of the vortex patch. Note that only half of the vortex (the positive half) needs to be discretized owing to the mirror symmetry about the $y-$axis possessed by the vortex patch.

The $y-$coordinates, y_i, of the system are kept constant and the system is solved for $x_2, \ldots, x_{N-1}$ and the translational velocity V_t, i.e. $x_i, i = 2, \ldots, N-1$ and V_t are adjusted at each iteration until the boundary becomes a streamline. Note that the solution is steady state and the vortex patch is not advected in time. Contour dynamics is used to find the velocity field (u_i, v_i), $i = 1, \ldots, N$ at each node due to the patch and its image in $y = 0$. As the size of the vortex patch gets smaller, the scale of surgery must be increased to get more accurate results. The scale of surgery was modified so that $N > 100$ regardless of the size of the vortex patch.

Let, without loss of generality,

$$\psi(x_1, y_1) = 0, \tag{5.12}$$

then using

$$d\psi = \frac{\partial \psi}{\partial x}dx + \frac{\partial \psi}{\partial y}dy, \tag{5.13}$$

the change in successive values of ψ along the boundary can be written as,

$$\psi_{i+1} - \psi_i = \bar{v}_i dx_i - \bar{u}_i dy_i, \; (i = 1, \ldots, N-1), \tag{5.14}$$

where $\psi_i = \psi(x_i, y_i)$ and

$$\bar{u}_i = \frac{u_{i+1} + u_i}{2}; \; \bar{v}_i = \frac{v_{i+1} + v_i}{2}, \tag{5.15}$$

and

$$dx_i = x_{i+1} - x_i; \; dy_i = y_{i+1} - y_i. \tag{5.16}$$

When the vortex patch is at a steady state, the boundary must be a streamline in a frame moving with the patch at a constant velocity, V_t, i.e.

$$\Psi(x,y) \Big|_{\text{patch boundary}} = (\psi(x,y) + V_t y) \Big|_{\text{patch boundary}} = c, \tag{5.17}$$

where c is a constant. Equation (5.17) can be written as

$$\Psi_i = \psi_i + V_t y_i = c, i = 2, \ldots, N, \tag{5.18}$$

which yields $N-1$ equations in the $N-1$ unknowns $x_i, i = 2, \ldots, N-1$ and V_t.

The Taylor expansion of $\Psi_i(x_2, x_3, \ldots, V_t)$ about $x_i^{new} = x_j + \Delta x_j$ can be used to form a linear system of simultaneous equations which can be solved to find the change in x_j, i.e. Δx_j at each iteration. Thus, iteratively, the solution for Ψ can be found using Newton's method. After Taylor expansion the system of equations can be written in matrix form as follows,

$$\begin{pmatrix} \frac{\partial \Psi_2}{\partial x_2} & \frac{\partial \Psi_2}{\partial x_3} & \cdots & \frac{\partial \Psi_2}{\partial V_t} \\ \frac{\partial \Psi_3}{\partial x_2} & \ddots & & \frac{\partial \Psi_3}{\partial V_t} \\ \vdots & & \ddots & \frac{\partial \Psi_4}{\partial V_t} \\ \frac{\partial \Psi_N}{\partial x_2} & \frac{\partial \Psi_N}{\partial x_3} & \cdots & \frac{\partial \Psi_N}{\partial V_t} \end{pmatrix} \begin{pmatrix} \Delta x_2 \\ \Delta x_3 \\ \vdots \\ \Delta V_t \end{pmatrix} = \begin{pmatrix} c - \Psi_2 \\ c - \Psi_3 \\ \vdots \\ c - \Psi_N \end{pmatrix}. \tag{5.19}$$

Each iteration involves matrix inversion to find Δx_j, ΔV_t, $j = 2, \ldots, N-1$. In general, the matrix coefficients $\partial \Psi_i / \partial x_j$ must be found numerically (see McDonald (2004)). Instead, we use the approximation made by Pierrehumbert (1980), namely that only the diagonal terms in the matrix are kept in which case the matrix system reduces to

$$\frac{\partial \Psi_i}{\partial x_i} \Delta x_i = c - \Psi_i, i = 2, \ldots, N-1, \tag{5.20}$$

or,

$$\Delta x_i = \frac{c - \Psi_i}{v_i}, i = 2, \ldots, N-1, \tag{5.21}$$

since

$$v_i = \frac{\partial \Psi_i}{\partial x_i}. \tag{5.22}$$

Thus, there is no need for matrix inversion and each iteration is very quick. There is no real justification for neglecting the off-diagonal elements $\partial \Psi_i / \partial x_j$, $(i \neq j)$, except that the resultant numerical method works in that it converges. This may be due to the diagonal dominance in the matrix in (5.19). Note the coefficients $\partial \Psi_i / \partial x_i = v_i$ given by (5.22) are simply the $y-$velocities at each node and are given at each iteration by the contour dynamics algorithm. The translational velocity, V_t is calculated using (5.19)

$$V_t = \frac{\psi_N - \psi_1}{y_1 - y_N}, \tag{5.23}$$

and the constant can be found at each iteration by putting $i = 1$ in (5.19):

$$c = V_t y_1. \tag{5.24}$$

Δx is then calculated using (5.21). To ensure convergence, an under-relaxation coefficient, $\mu = 0.6$ is used. The resulting iterative scheme can be written

$$x_i^{n+1} = x_i^n + \mu \Delta x_i^n. \tag{5.25}$$

The new value, x_i^{n+1}, is used to re-calculate values of V_t, c and Ψ_i iteratively until the boundary of the vortex patch has a constant streamline and the relative difference between successive iterations of translational velocities is less than 10^{-6}.

Depending on the steady shape of the vortex patch and its deviation from the initial circular shape, the number of iterations required until convergence varies. Smaller patches stay roughly circular, therefore the number of iterations required is less. Larger patches tend to be less circular and hence require more iterations until the steady shape is found. The number of iterations, depends on the shape of the final vortex varies between ten and one hundred. It is also noted that a circle need not be the initial basis from which to start the iterations. In particular, when examining certain background flows elliptical initial shapes were needed to achieve convergence.

The number of points N used to discretize the patch boundary also varies depending on the size of the vortex. A minimum number of fifty points for the smallest vortex patch with $R = 0.025$ was used. There needs to be enough points to get an accurate velocity field and therefore smaller vortices require higher resolution. A maximum of four hundred points was used for the larger vortex patches having $R \sim 0.5$.

5.4 Numerical results for the finite Rossby radius

In the non-dimensional problem the value of y_N is set to one, meaning y_1 and a are the only independent variables (in the absence of background flow). The top vortex and the image vortex have non-dimensional vorticity ± 1 respectively.

In Fig. 5.3, two families of solutions corresponding to $a = 5, 99$ for the steady translating vortex pairs are shown. There is effectively no difference in patch shape for $a \gtrsim 5$ and they, not surprisingly, closely resemble the solutions computed by Pierrehumbert (1980) in the $a \to \infty$ limit. Note that the smaller vortex patches are circular while the larger patches are more ‘elliptical’, flattening along the edge closest to the line of symmetry (or wall).

There is a small difference in V_t between $a = 5$ and $a = 99$ as shown in Fig. 5.4), with the smaller value of a having a corresponding smaller translational velocity V_t, since the range of influence of one vortex on the other decreases owing to the exponential decay associated with $K_1(r/a)$. Vortex patch size is also an important factor in determining V_t. Larger vortex pairs that are closer together move quickly, because the velocity induced by the image vortex is stronger than for smaller vortex pairs.

The translational velocity can be scaled by the circulation (or, equivalently, area): let $\hat{V}_t$ be the scaled translational velocity,

$$\hat{V}_t = \frac{V_t}{\mathcal{Q}} \tag{5.26}$$

where the circulation is

$$\mathcal{Q} = \iint_D q \, \mathrm{d}A, \tag{5.27}$$

where q is the potential vorticity of the system and D is the area enclosed within the contour C, i.e. the boundary of the vortex patch. Since $q = 1$ everywhere inside the vortex patch, $\mathcal{Q}$ is simply the area of the vortex patch. The velocity of an equivalent (i.e. same circulation) pair of point vortices located at the centroids of the patches, $(0, \pm y_{cen})$, is compared to $\hat{V}_t$, where y_{cen} is computed from

$$y_{cen} = \iint_D y \, \mathrm{d}A \Big/ \iint_D \mathrm{d}A. \tag{5.28}$$

The location of the centroid is found numerically using Green's theorem,

$$y_{cen} = \frac{1}{\mathcal{Q}} \iint_D y \, \mathrm{d}A = \frac{1}{\mathcal{Q}} \oint_C \frac{y^2}{4} \, \mathrm{d}x - \frac{xy}{2} \, \mathrm{d}y. \tag{5.29}$$

It is noted that by symmetry, $x_{cen} = 0$.

The equivalent point vortex pair translation velocity can be written,

$$V_p(0, y_c) = \frac{K_1(2y_c/a)}{2\pi a}, \tag{5.30}$$

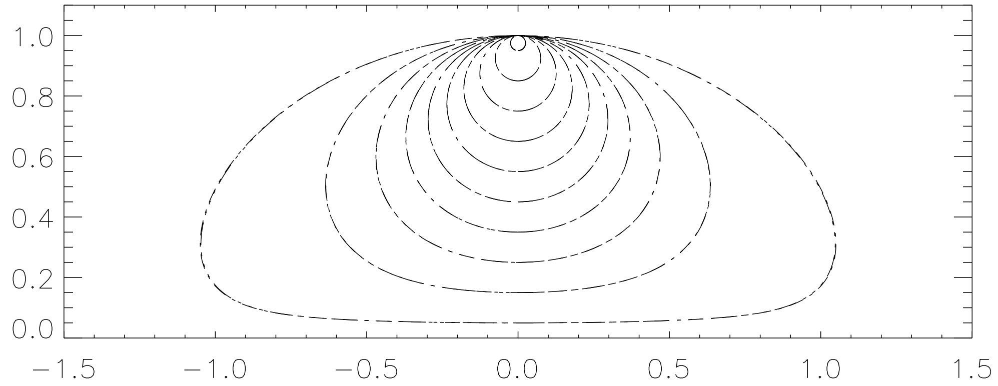

Figure 5.3: Family of solutions for vortex pairs with finite a, $a = 5$ (dashed) $a = 99$ (dotted) with $y_1 = 0.05 + n/10, n = 0, 1 \ldots, 9$. The two sets of results are indistinguishable in this plot.

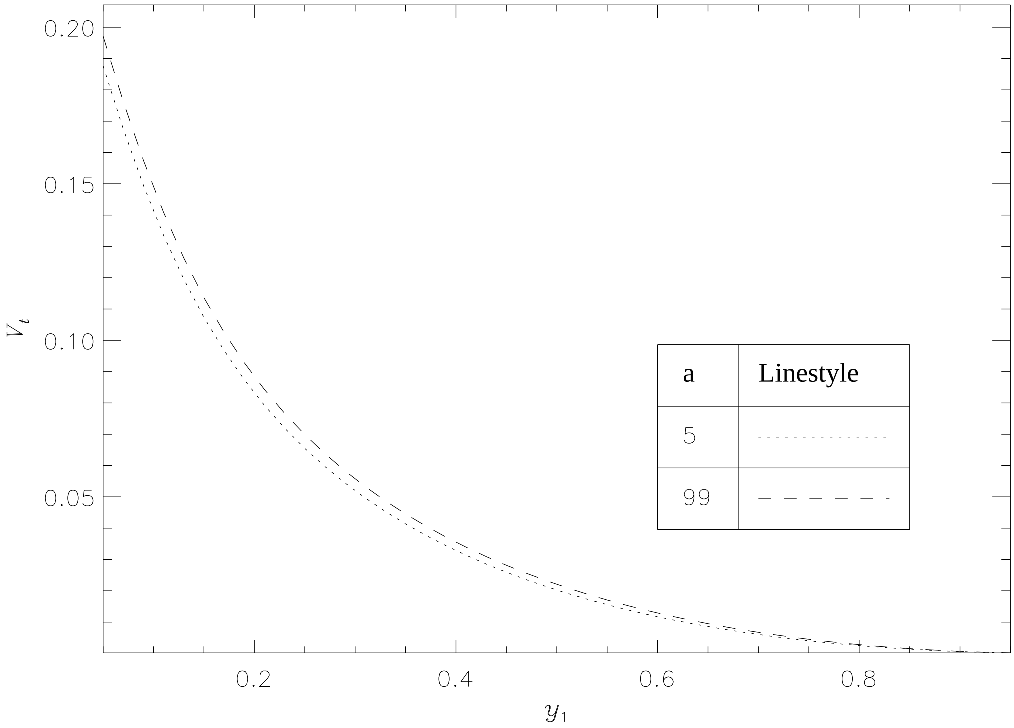

Figure 5.4: V_t is plotted against $y_1 = 0.05 + n/50, n = 0, \ldots, 45$, $a = 5, 99$.

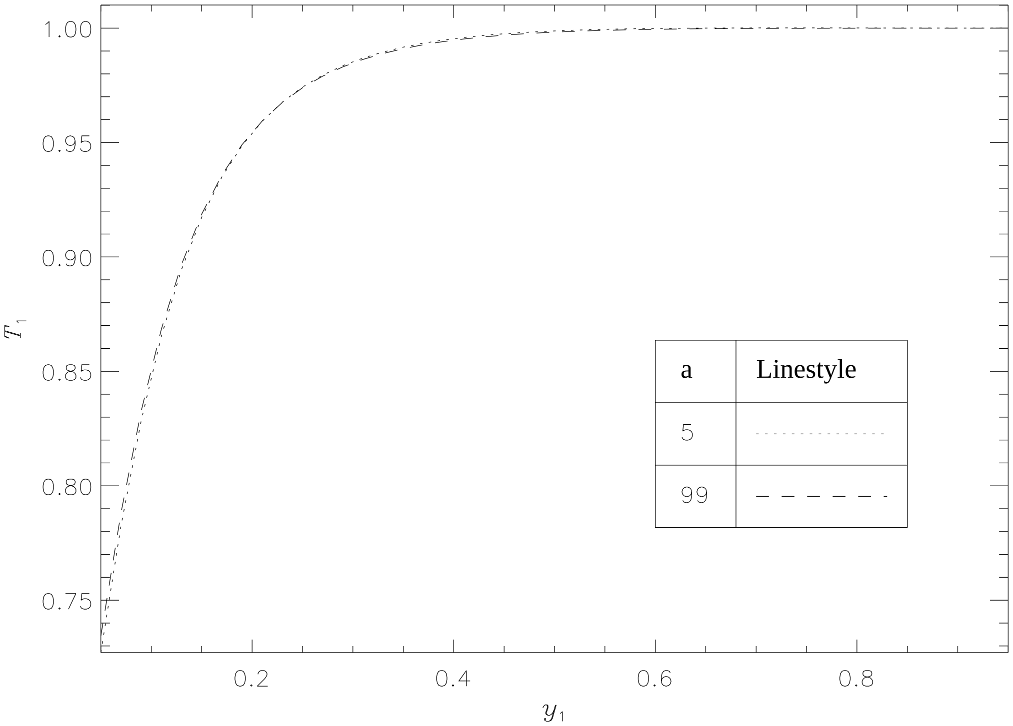

Figure 5.5: The scaled translational speed T_1 is plotted against y_1 for $a = 5, 99$. There is negligible difference in T_1 for these two values of a.

where K_1 is the modified Bessel function of the second kind of order one. The ratio, $T_1 = \hat{V}_t/V_p$ is plotted against y_1 in Fig.5.5. Small vortex patches ($y_1 \rightarrow 1$) remain roughly circular and hence the velocity is expected to approach that of a point vortex pair. Indeed the curve does asymptotically approach unity in this limit. As the vortex patches become larger ($y_1 \rightarrow 0$), they become more deformed, flattening out towards the bottom and thus travelling slower in comparison to a point vortex pair.

The effects of decreasing a further (i.e. below 5) can be seen in Fig. 5.6, where the shapes of the vortex patches are shown for $a = 1, 2, 5$. While the shapes are broadly similar there are some notable differences. For the largest vortex patch, $y_1 = 0.05$, the vortex patches are larger for $a = 1, 2$ than for $a = 5$. However, for $y_1 > 0.05$, smaller a yields slightly smaller vortex patches. This latter effect is because of a decrease in a, there is less of an effect due to the image vortex as the streamfunction of the vortex patches decays faster. However when y_1 is sufficiently small, the counter-rotating vortex patches form larger vortex patches. This is because the self-induced velocity of a patch on itself also decreases with a. At some point the self induced velocity is less than that of its image, causing the patch to elongate near the wall. Notably, for $a = 1$, $y_1 = 0.05$, the two furthest points on the vortex are greater than $2a$ apart.

Let R be the mean radius of a patch, i.e. the mean distance of the patch boundary from its centroid. The difference in R between $a = 5$ and $a = 1$ (i.e. $\Delta R = R|_{a=5} - R|_{a=1}$) (dotted) and $a = 5$ and $a = 2$ (dashed) is plotted in Fig. 5.7 as a function of y_1. There is a clear change in mean radius in that there can be either positive and negative values of ΔR as y_1 is varied. The mean radius in both $a = 1$ and $a = 2$ cases can be either greater or less than that of $a = 5$. Note the magnitude of the difference, as expected, is generally less in the $a = 2$ case.

The translational velocities, V_t, however, are shown to decrease with respect to y_1 in Fig. 5.8, regardless of the size of the vortex patch. Smaller a correspond to

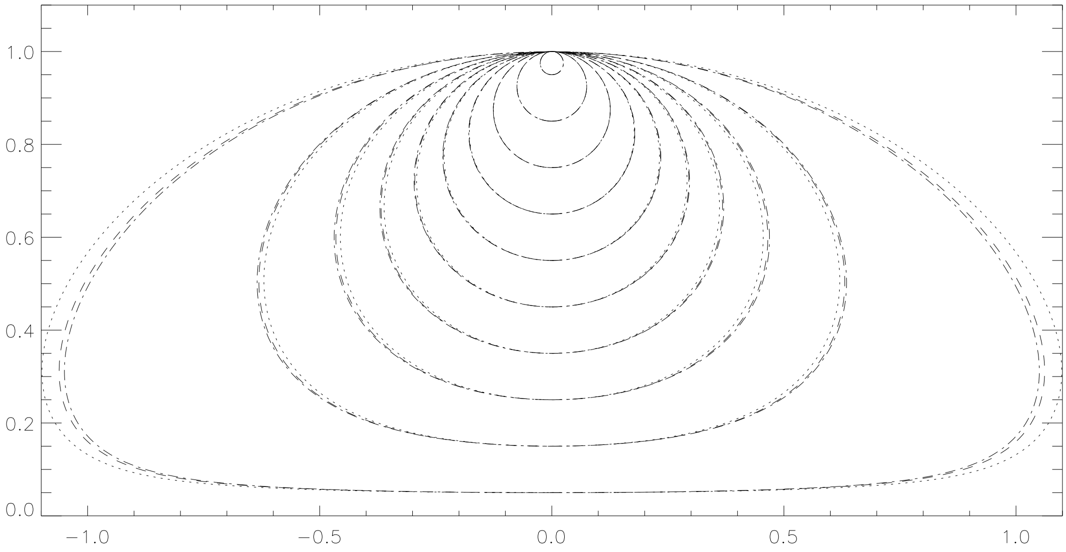

Figure 5.6: Family of solutions for vortex pairs with finite a, $a = 1, 2, 5$ with $y_1 = 0.05 + n/10, n = 0, 1 \ldots, 9$. Here, $a = 1$ (dotted), $a = 2$ (dashed) and $a = 5$ (dot-dash).

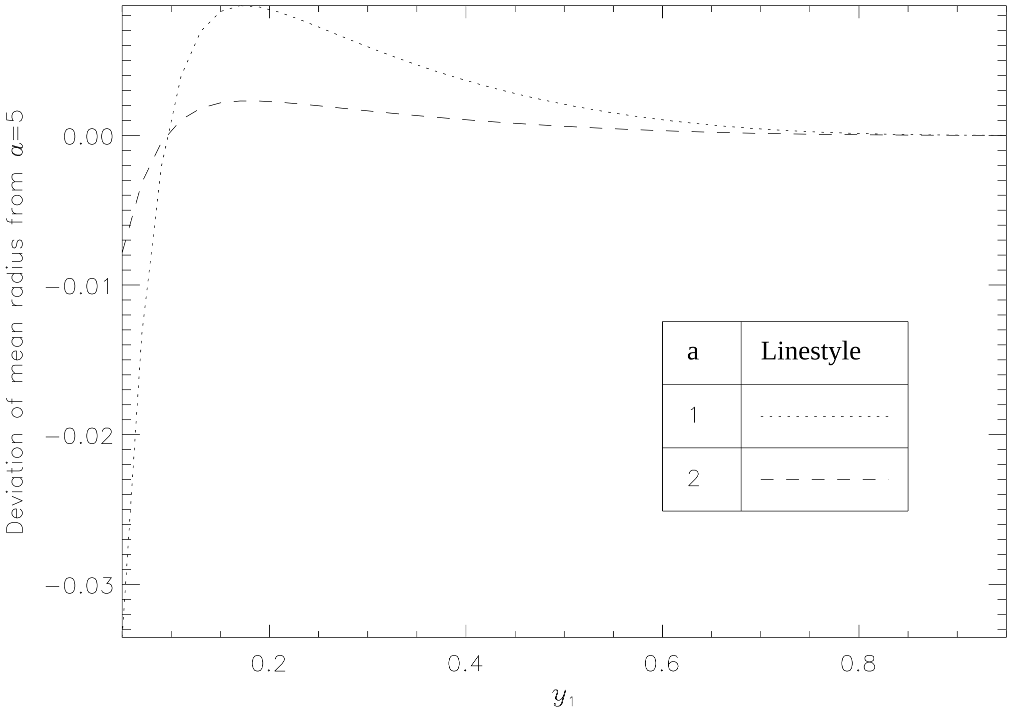

Figure 5.7: Difference in mean radius of steady vortex patch between different values of a. The difference between $a = 5$ and $a = 1$ is dotted and the difference between $a = 5$ and $a = 2$ is dashed.

smaller V_t, again as expected on the basis of more rapid decay of the velocity field induced by a patch.

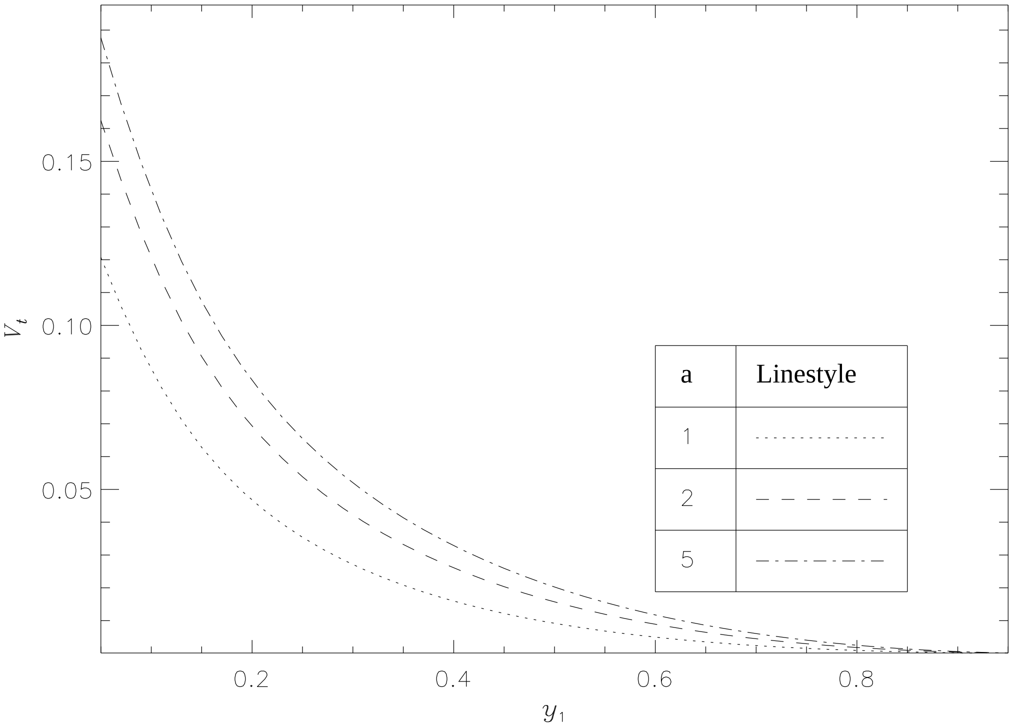

Figure 5.8: V_t is plotted against y_1 for $a = 1, 2, 5$.

The conventional scaling method for the translation speed based on area which is useful for larger a (see Fig. 5.5), is less appropriate for $a = 1, 2$ than $a = 5$ (see Fig. 5.9). An increasing difference in the translation speed as a decreases.

The method used for normalising the vortex patches discussed in Section 4.1 is also employed here: see Fig. 5.10 where the new scaled speed, $T_2 = V_t'/V_p$ is plotted against y_1, where, V_t' is the translational velocity scaled according to the new normalisation scheme,

$$V_t' = \frac{V_t}{\mathcal{S}^2 \mathcal{Q}}, \tag{5.31}$$

where, recall,

$$\mathcal{S} = \frac{2a}{R} I_1(R/a), \tag{5.32}$$

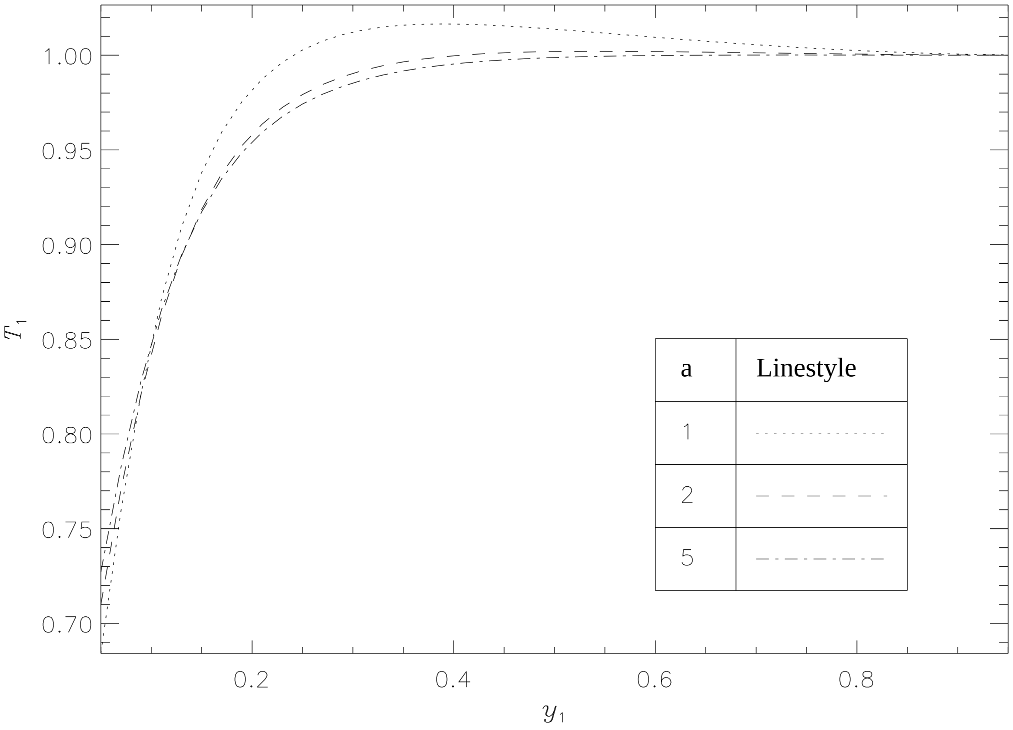

Figure 5.9: T_1 is plotted for $a = 1, 2, 5$. As a becomes smaller, there is a greater deviation from the point vortex solution.

and R is the mean radius of the vortex patch and I_1 is the modified Bessel function of the first kind of order one.

Fig. 5.10 gives much better agreement over a larger range of y_1 than the conventional scaling used in Fig. 5.9.

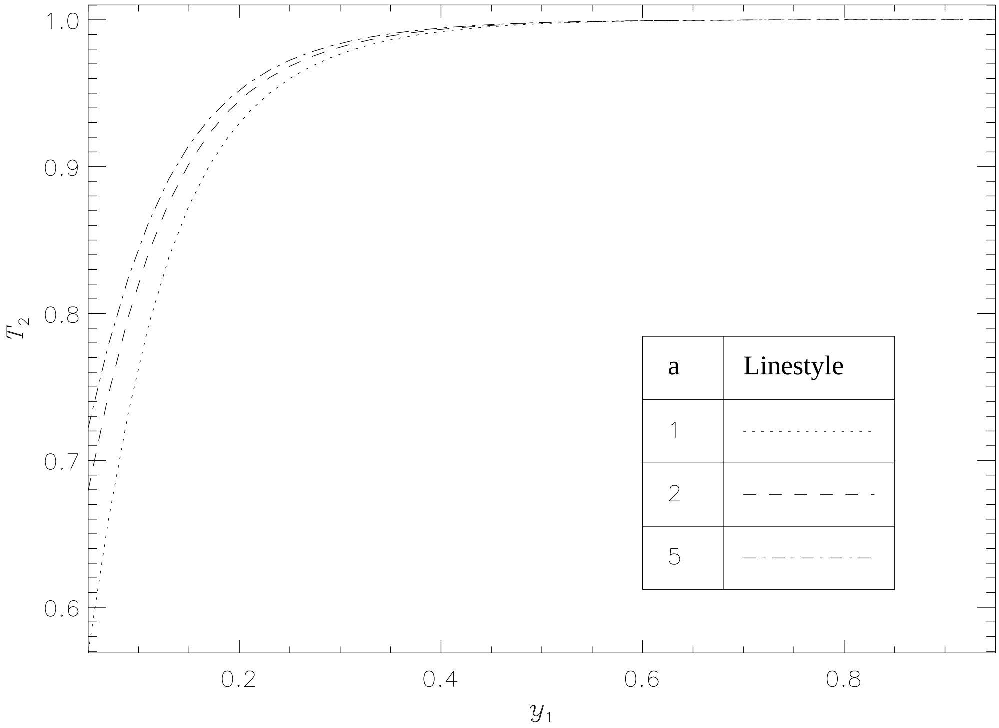

Figure 5.10: Normalised translational velocities using the scale factor $\mathcal{S}^2\mathcal{Q}$.

As is the case for large a, Fig. 5.10 shows that the smaller patches (i.e. $y \to 1$) that stay roughly circular have similar values of the point vortex velocity, however, the vortex patches gradually deform from their circular shape when they get closer to each other. These trends are further exemplified for even smaller values of $a = 0.4, 0.7, 1$ in Fig. 5.11, Fig. 5.12 and Fig. 5.13.

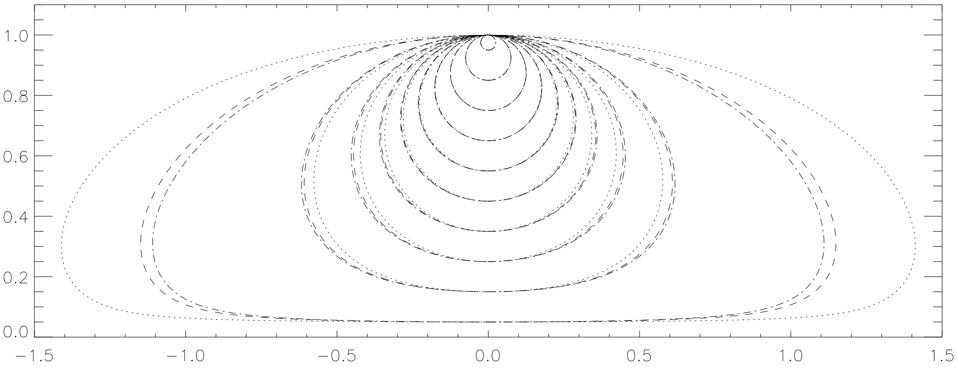

Figure 5.11: Family of solutions for vortex pairs with finite a, $a = 0.4, 0.7, 1$. Here, $a = 0.4$ (dotted), $a = 0.7$ (dashed) and $a = 1$ (dot-dash).

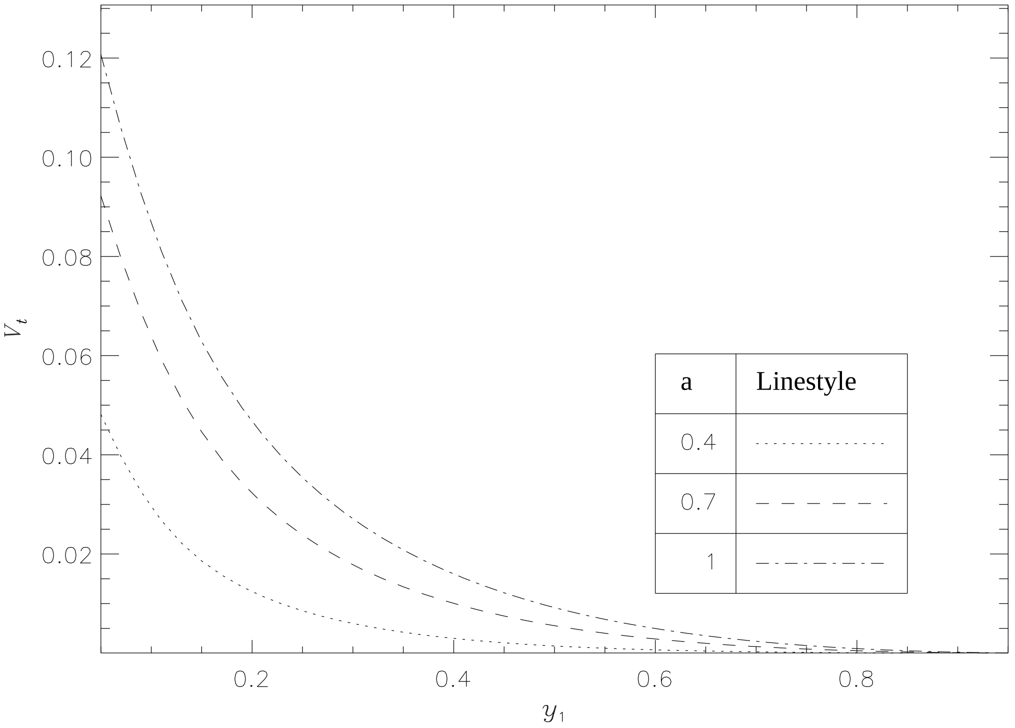

Figure 5.12: V_t plotted against y_1 for $a = 0.4, 0.7, 1$.

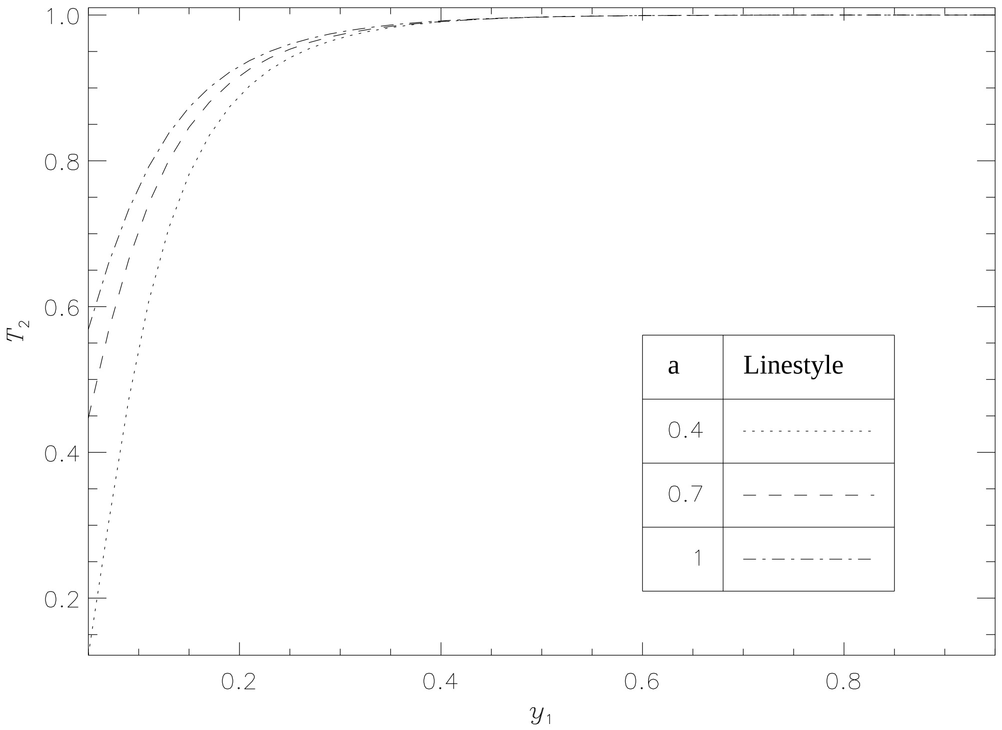

Figure 5.13: Using the new normalisation technique, V_t' for vortex patches is compared to V_p for $a = 0.4, 0.7, 1$. T_2 is plotted against y_1.

5.4.1 Time dependent advection

The stability of the steady vortex shapes can be checked by using them as the initial conditions in a time-dependent contour dynamics algorithm. Here, contours with $y_1 = 0.05$ for $a = 0.4, 100$ are advected using the fourth order Runge-Kutta method with time step, $\Delta t = 0.1$ for one hundred time steps. For comparison, the original vortex patch shape (i.e. the shape at $t = 0$) is plotted over the patch shape after one hundred time-steps, ($t = 10$) in Fig. 5.14-5.15.

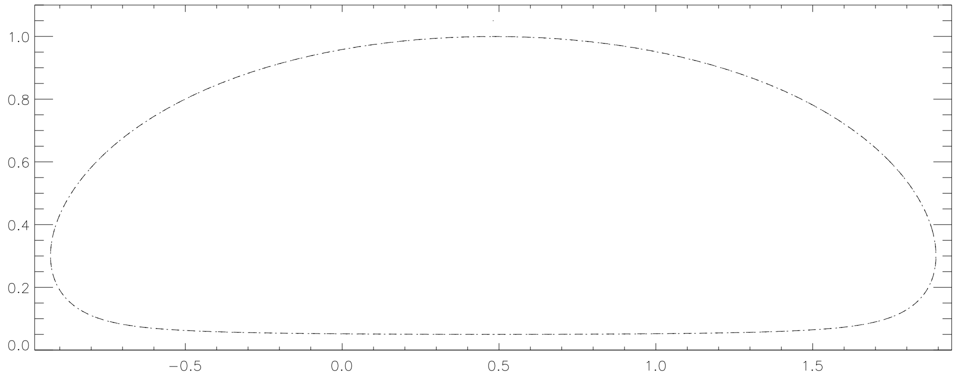

Figure 5.14: The dotted line represents the vortex patch at $t = 10$ with $a = 0.4$, with $y_1 - = 0.05$ at $t = 0$. The dashed line is the original vortex patch.

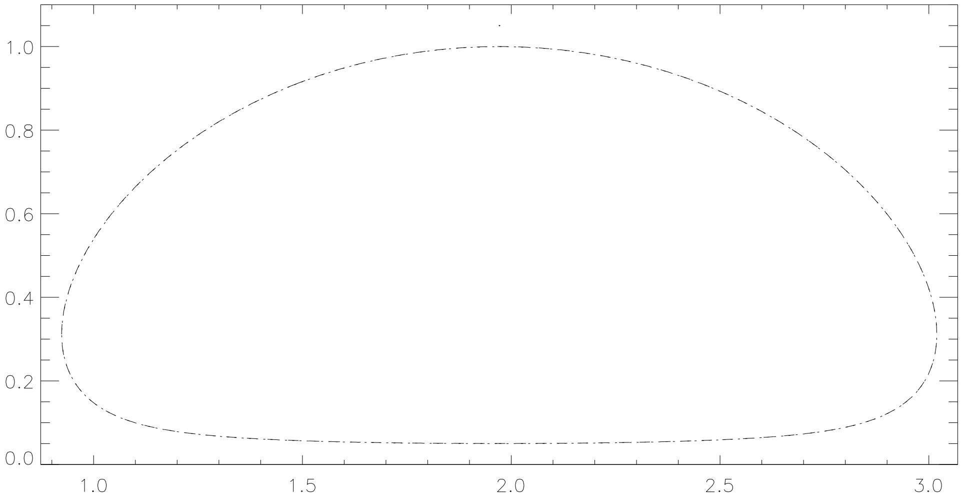

Figure 5.15: Same as in Fig. 5.14 but with $a = 1$.

The excellent comparison shown in Fig. 5.14-5.15 suggests that the equilibria are stable and that their stability is independent of the deformation radius.

5.5 Vortex pair motion in the presence of background shear flow

The effect of background flows can influence the shape, speed and direction of propagation of the vortex patches. V-states in the presence of such background flows are found by adjusting the contour dynamics algorithm. The background flow must satisfy the quasigeostrophic equation such that,

$$\nabla^2\psi_b - \frac{1}{a^2}\psi_b = 0, \tag{5.33}$$

where ψ_b is the streamfunction of the background flow. We note that is trivial in the rigid-lid case as it simply amounts to a different translation speed without change of shape. For arbitrary deformation radius the situation is non-trivial.

For flow parallel to the direction of propagation of the vortex pair the streamfunction satisfying the quasigeostrophic equation (i.e. Helmholtz's equation) and bounded at infinity is

$$\psi_b = C\mathrm{sgn}(y)\exp(-|y|/a), \tag{5.34}$$

where C is a constant, the sign of which determines the direction of the background flow. Hence, there is a constant horizontal velocity induced by the background flow at any given y is

$$u_b(y) = \frac{C}{a}\exp(-|y|/a). \tag{5.35}$$

Note, that (5.35) can be interpreted as a shear flow parallel to the wall which decays exponentially with distance from the wall.

5.5.1 Numerical results

The velocity induced at the boundary of the patch due to the background flow, $u_b(y)$ is used in addition to the velocity induced by the patch itself and its image. Hence, the horizontal velocity at each node is given by,

$$u_i = u_{patch_i} + u_{image_i} + u_b(y_i). \tag{5.36}$$

With this modification the algorithm described in Section 5.3 proceeds as before. The steady shape depends on the coefficient, C, of the background flow and the value of a. It is noted that for $|C| > 0.5/\pi$ and $y_1 < 0.5$ for $a < 1$ steady shapes could not be computed due to the high level of distortion of the vortex patch boundary i.e. convergence could not be achieved. Therefore, in Sections 5.5.2-5.5.3, the $a \geq 1$ cases are considered. First, the case of positive C is examined, which will hence be called the positive background flow. The direction of both the background flow and the self-induced vortex pair velocity are the same, so the net translational velocity increases.

5.5.2 Positive background shear flow

To illustrate the effect of background flow on the steady vortex shape, the previous zero background flow ($C = 0$) steady shapes are plotted over the new steady shapes ($C \neq 0$). For $a = 99$, the velocity $u_b \to C/a$ (i.e. a constant background flow) and the change that occurs in the V-state shapes compared to the zero background flow is negligible. That is, a constant background flow has no effect on the shape, but merely affects the net translational speed. In Fig. 5.16, where $C = 1/\pi$, this can be seen as the $C = 0$ and $C = 1/\pi$ patch boundaries overlap precisely.

Let the translational velocity with $C \neq 0$ be V_b and $C = 0$ be V_t. Fig.5.17 shows the translational velocities, V_t and V_b of the steady vortex patches. Note that the difference of the translational velocity with background flow relative to zero

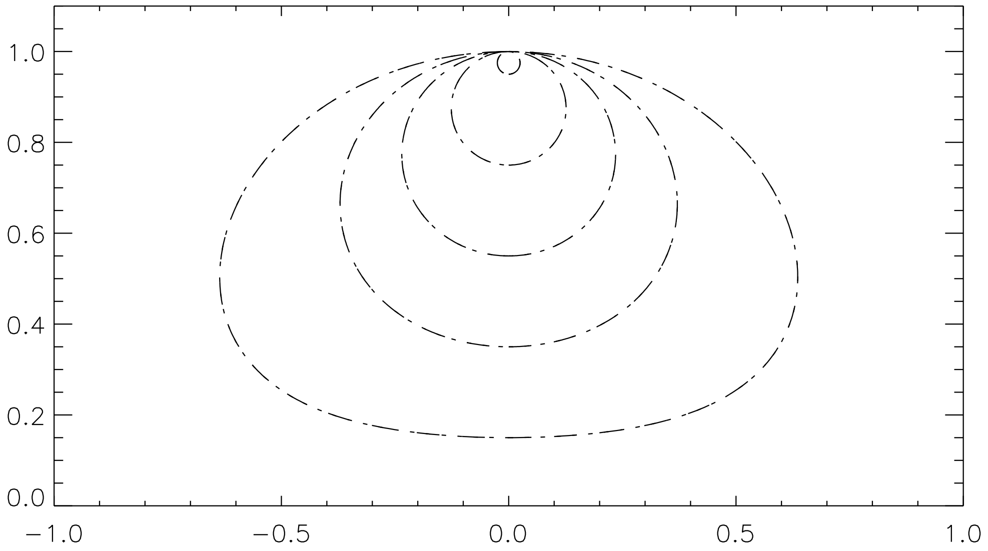

Figure 5.16: Family of solutions for vortex pairs with $a = 99$ with a background flow coefficient $C = 1/\pi$ (dotted) and $C = 0$ (dashed).

background flow becomes larger as the vortex patches become smaller.

In Fig. 5.18, $a = 2$, $u_b = C \exp(-|y|/2)/2$, and the background flow is seen to significantly affect the shape of the steady vortex patches. To aid convergence, the initial shape of the vortex patch was taken to be an ellipse such that the semi-minor axis was along the $y-$axis and with semi-major axis taken to be twice that of the semi-minor axis. In the presence of background flow, the patches are more elliptical, extending wider in the $x-$direction. The translational velocities, V_b and V_t for $a = 2$ are plotted together in Fig. 5.19 showing, as expected, an increase in translational velocity (as is the case for $a = 99$) however, the difference is even greater.

In Fig. 5.20, $a = 1$ and the change in the patch shape in the presence of background flow is even more pronounced. The increase in the translational velocity can be seen in Fig. 5.21

As discussed in Chapter X, Section Y, in the presence of background flow, not only must the point vortex circulation be scaled appropriately, so must the background flow itself. Recall the circulation of the point vortex equivalent of the patch

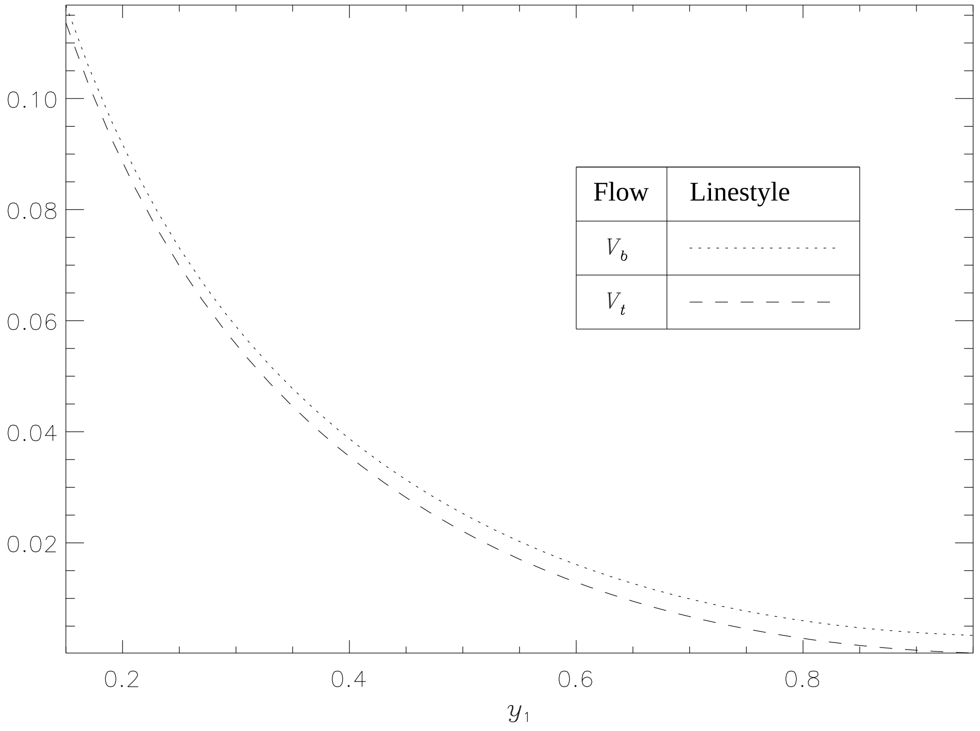

Figure 5.17: V_b and V_t plotted against y_1 and the horizontal velocity, $C = 1/\pi$ and $a = 99$ (dotted) and $C = 0$ (dashed). The background flow and the self-induced vortex propagation are cooperative, hence, the translational speed in the presence of the background flow are greater.

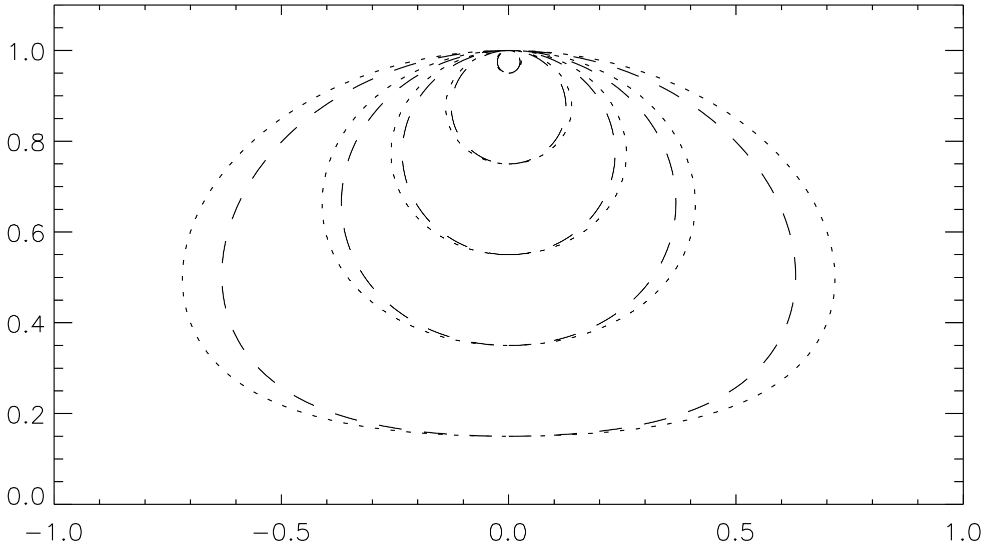

Figure 5.18: Family of solutions for vortex pairs with $a = 2$ with a background flow coefficient $C = 1/\pi$ (dotted) and $C = 0$ (dashed).

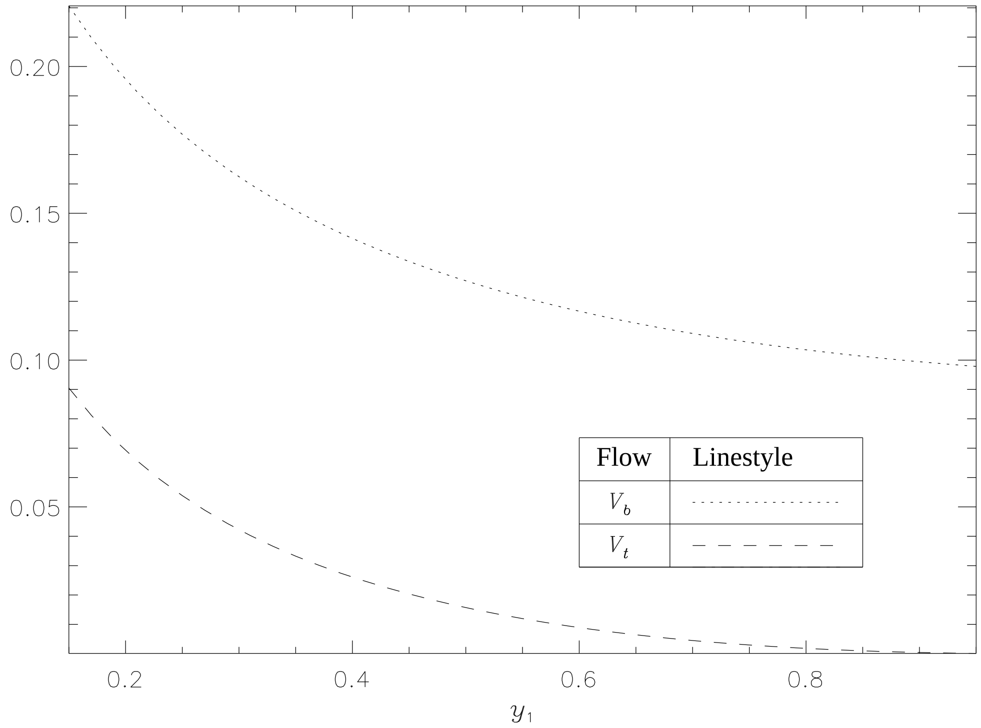

Figure 5.19: V_b and V_t plotted against y_1 and the horizontal velocity, $C = 1/\pi$ and $a = 2$.

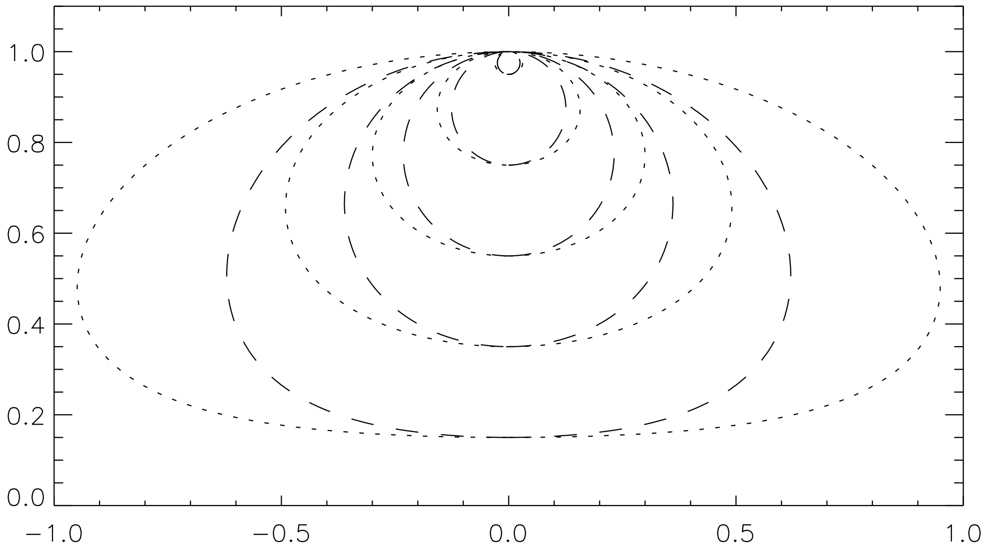

Figure 5.20: Family of solutions for vortex pairs with $a = 1$ with a background flow coefficient $C = 1/\pi$ (dotted) and $C = 0$ (dashed).

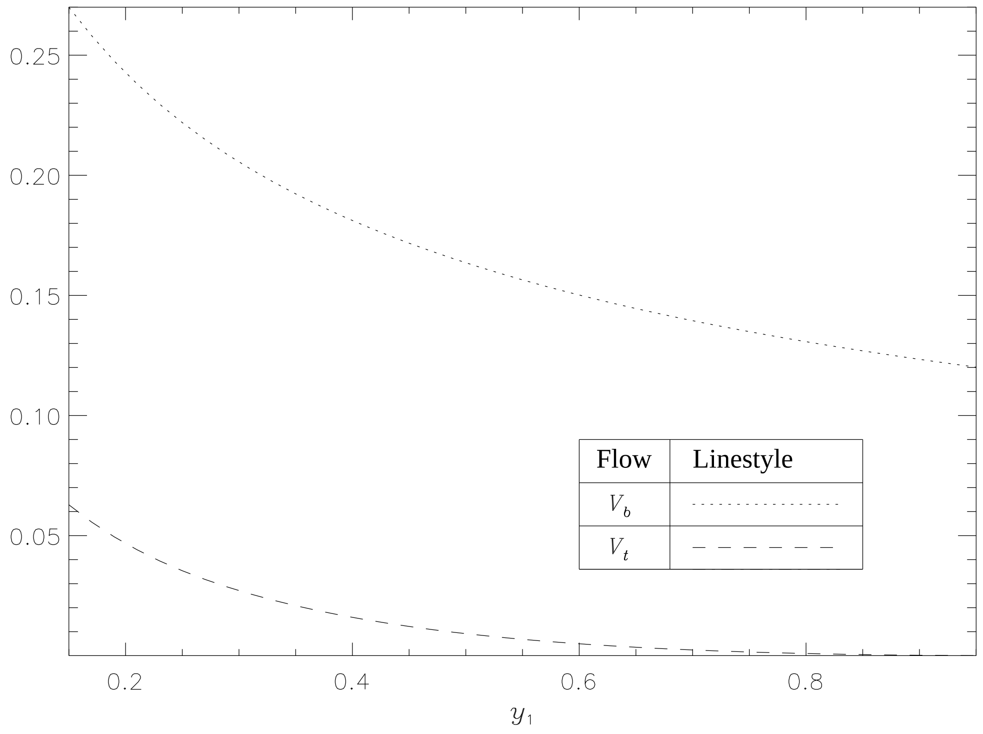

Figure 5.21: V_b and V_t plotted against y_1 and the horizontal velocity, $C = 1/\pi$ and $a = 1$.

is $\Gamma_V = \mathcal{S}^2\mathcal{Q}$, where,

$$\mathcal{S} = \frac{2a}{R} I_1(R/a), \tag{5.37}$$

and R is the mean radius of the patch. The external velocity field owing to the background flow is scaled with $\mathcal{S}$, and hence $C_p = \mathcal{S}C$, is the constant associated with the background flow. The point vortex is again located at the centroid of the patch and can be written as,

$$V_p = \Gamma_p \frac{K_1(2y_{cen}/a)}{2\pi a} + \frac{C_p}{a}\exp(-|y_{cen}|/a). \tag{5.38}$$

The velocity ratio, $T_3 = V_b/V_p$ is shown in Fig. 5.22 for $a = 1, 2, 99$. For the smaller, circular patches ($y_1 \to 1$), the agreement of V_b with the normalised point vortex pair velocity, V_p is good. However, for the $a = 1$ case, recall the rate of deformation of the vortex shape with increase of radius is faster and hence, tapers away from

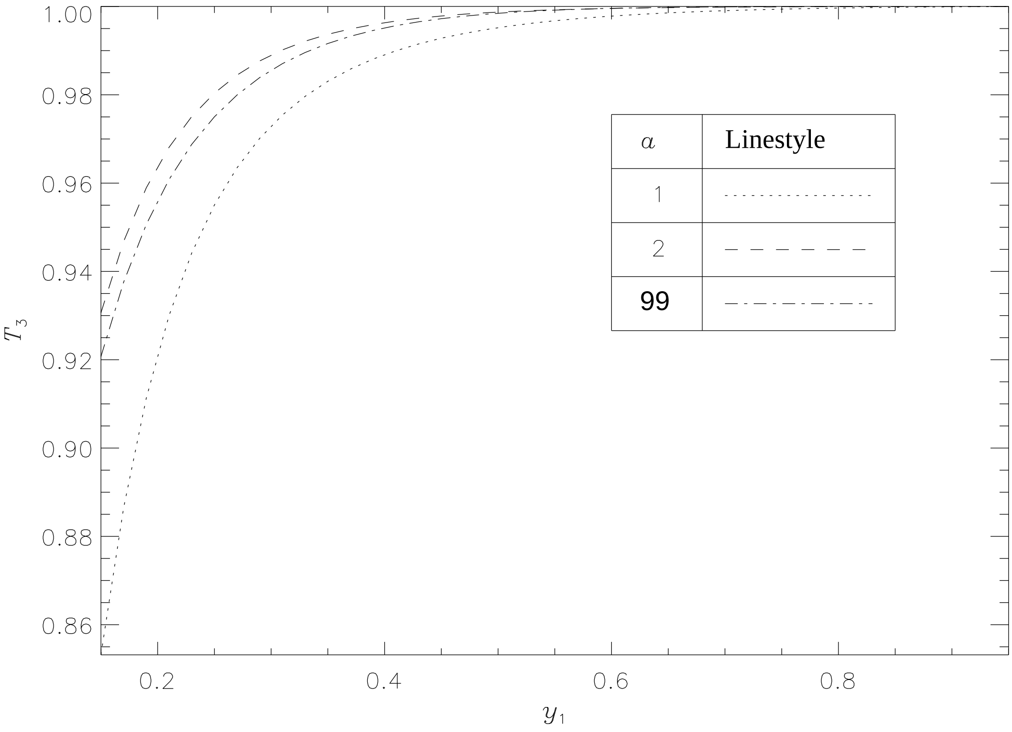

Figure 5.22: T_3 plotted against y_1

$T_3 = 1$ asymptote faster than the $a = 2, 99$ cases as y_1 decreases.

5.5.3 Negative background shear flow

Using a negative coefficient $C = -1/\pi$ the background flow now opposes the self propagation velocity of the vortex pair.

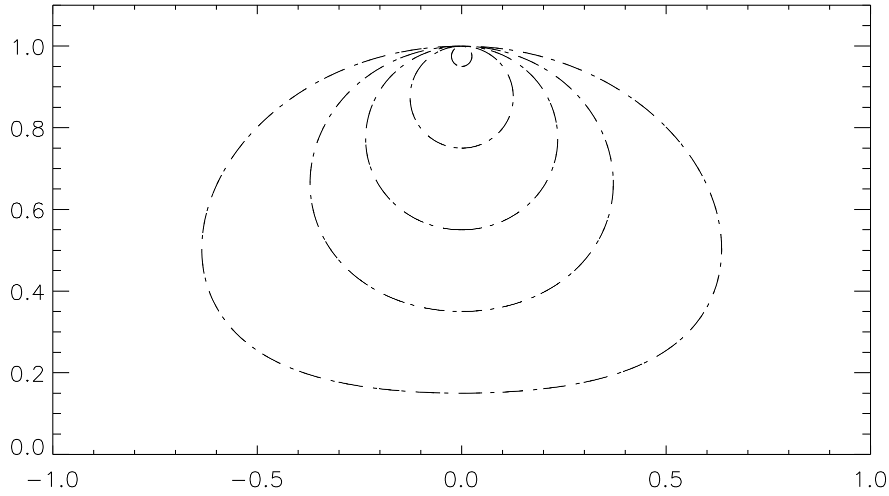

Figure 5.23: Family of solutions for vortex pairs with $a = 2$ with a background flow coefficient $C = -1/\pi$ (dotted) and $C = 0$ (dashed).

As is the case for the positive background flow, when $a = 99$, there is little change in the shape of the steady vortex patches and the same is true for the negative background flow (see Fig. 5.23). Also, there is only a slight decrease in the translational velocity V_b due to the negative background flow (see Fig. 5.24).

In Fig 5.25, $a = 2$ and the negative background flow forces the steady shapes to become smaller compared to their zero background flow counterparts. Note, in order to ensure convergence, in this case, the initial shape of the vortex patch was taken to be an ellipse such that the semi-major axis was along the $y-$axis and with semi-minor axis half that of the semi-major axis.

The translational velocity is also affected (see Fig. 5.26) with all patches going in the opposite direction (i.e. negative velocity) to the zero background flow case.

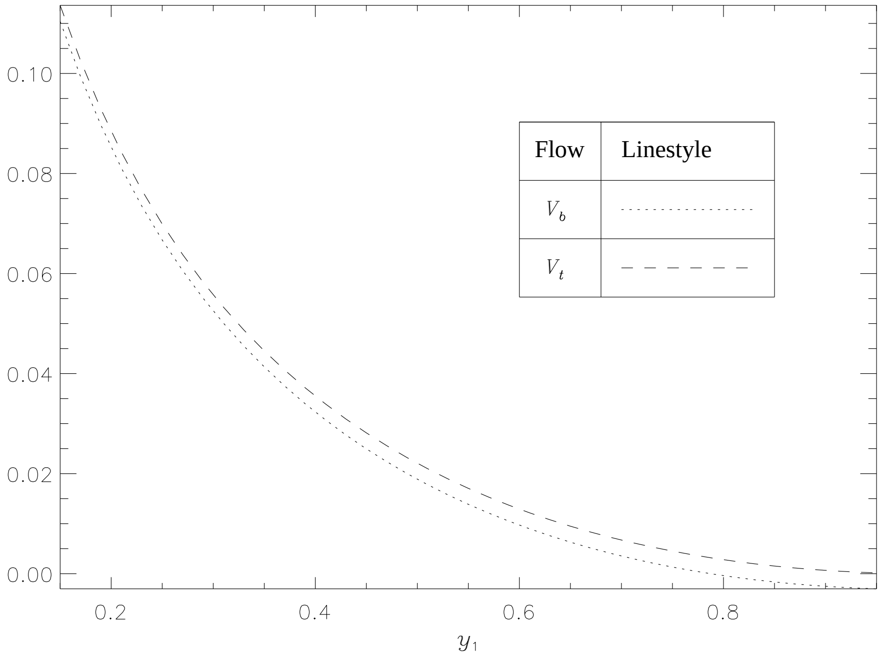

Figure 5.24: V_b and V_t plotted against y_1 and the horizontal velocity, $C = 1/\pi$ and $a = 99$ (dotted) and $C = 0$ (dashed). The background flow and the self-induced vortex propagation now oppose each other, hence, the translational speed in the presence of the background flow are decreased.

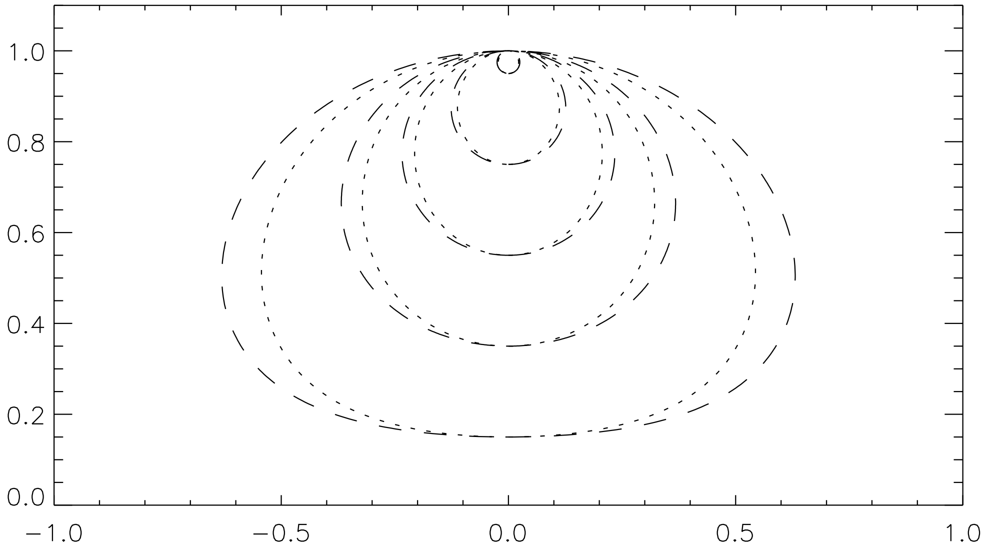

Figure 5.25: Family of solutions for vortex pairs with $a = 2$ with a background flow coefficient $C = -1/\pi$ (dotted) and $C = 0$ (dashed).

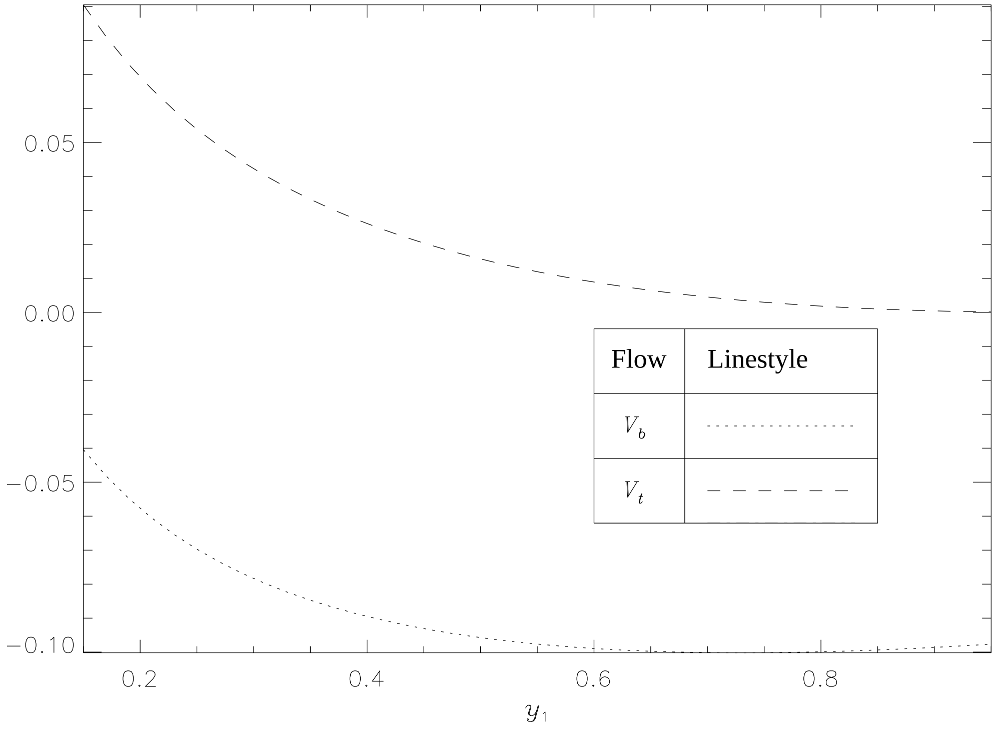

Figure 5.26: V_b and V_t plotted against y_1 and the horizontal velocity, $C = -1/\pi$ and $a = 1$. The vortex patch pairs propagate in the direction of the background flow contrary to the direction of the propagation with zero background flow.

The velocity induced by the image vortex is never stronger than the background flow and all the vortex patch pairs travel in the direction of the background flow.

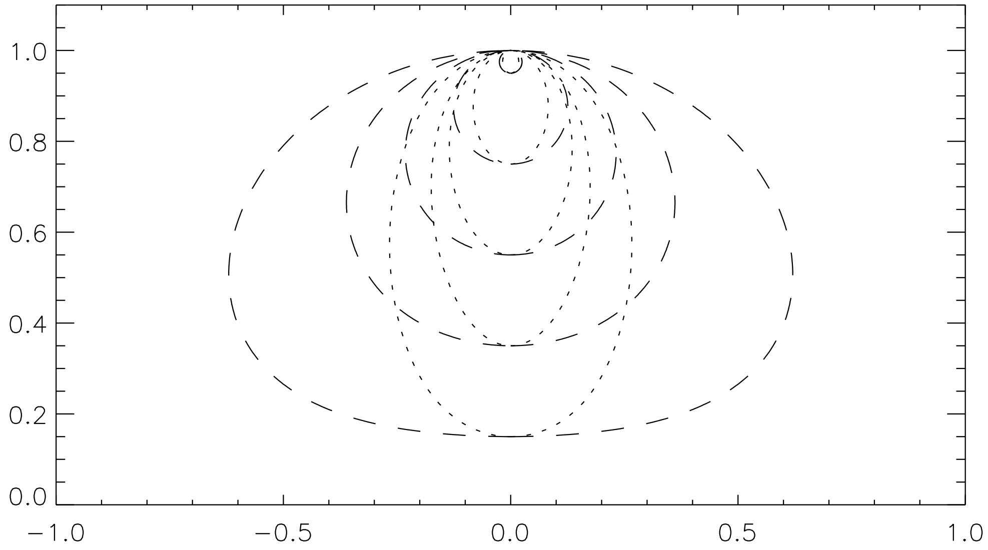

Figure 5.27: Family of solutions for vortex pairs with $a = 1$ with a background flow coefficient $C = -1/\pi$ (dotted) and $C = 0$ (dashed).

The contrast between the shapes is even more stark for the $a = 1$ case in Fig. 5.27. The vortex patches are roughly elliptical. The background flow now has a relatively strong effect, forcing all of the vortex patches in the opposite direction (see Fig. 5.28).

The normalisation technique is used again to show the comparison with the point vortex pair in Fig. 5.29 as before. The discrepancy, as expected, is great for large vortex patches, however, due to the deformation from the circular shapes of the vortex patch.

In Fig. 5.30 vortex shapes for a number of different background flow strengths $C = -(1. + n/2)/\pi, n = 0, \ldots, 4$ for fixed $y_1 = 0.15$ and $a = 1$ are shown.

The point where the translational velocity V_b changes from positive to negative is where the vortex patch is stationary. In Fig. 5.31, V_b is plotted against C and the point where, $V_b = 0$ is found using linear interpolation and marked with (+). The relaxation algorithm can be modified slightly to accurately compute the critical value of C. This is discussed in the next section.

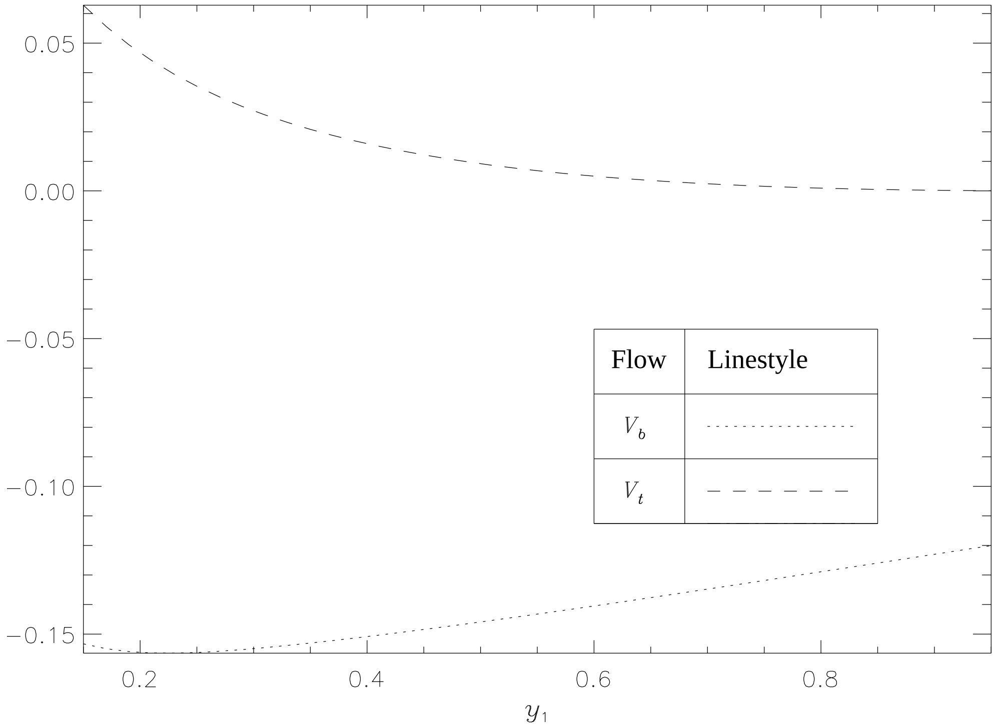

Figure 5.28: V_b and V_t plotted against y_1 and the horizontal velocity, $C = -1/\pi$ and $a = 0.5$.

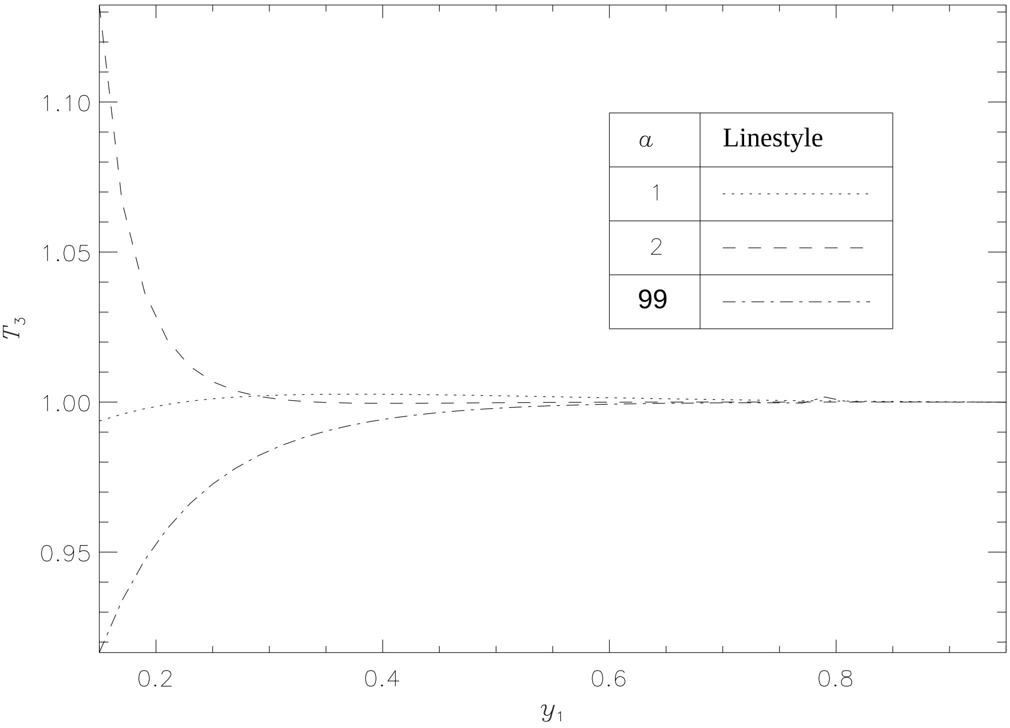

Figure 5.29: T_3 plotted against y_1

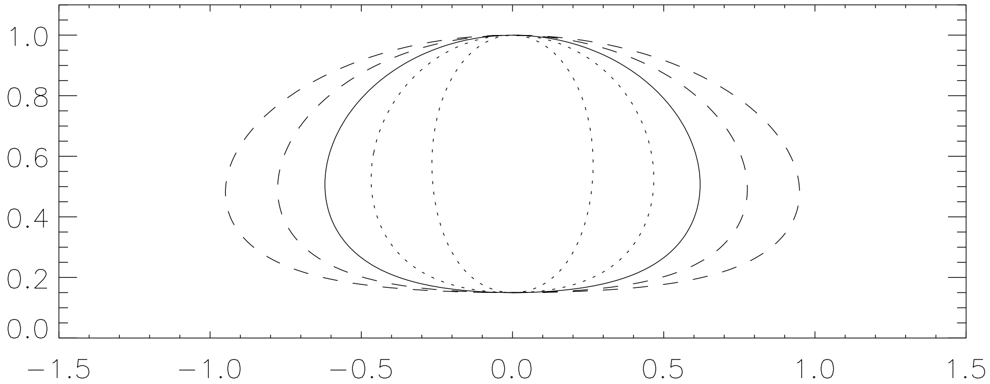

Figure 5.30: For fixed $a = 1$, the coefficient of the background flow C is varied to generate different vortex shapes. The dotted and dashed lines are the steady shapes for negative and positive background flows respectively. The solid line is the zero background flow ($C = 0$) case.

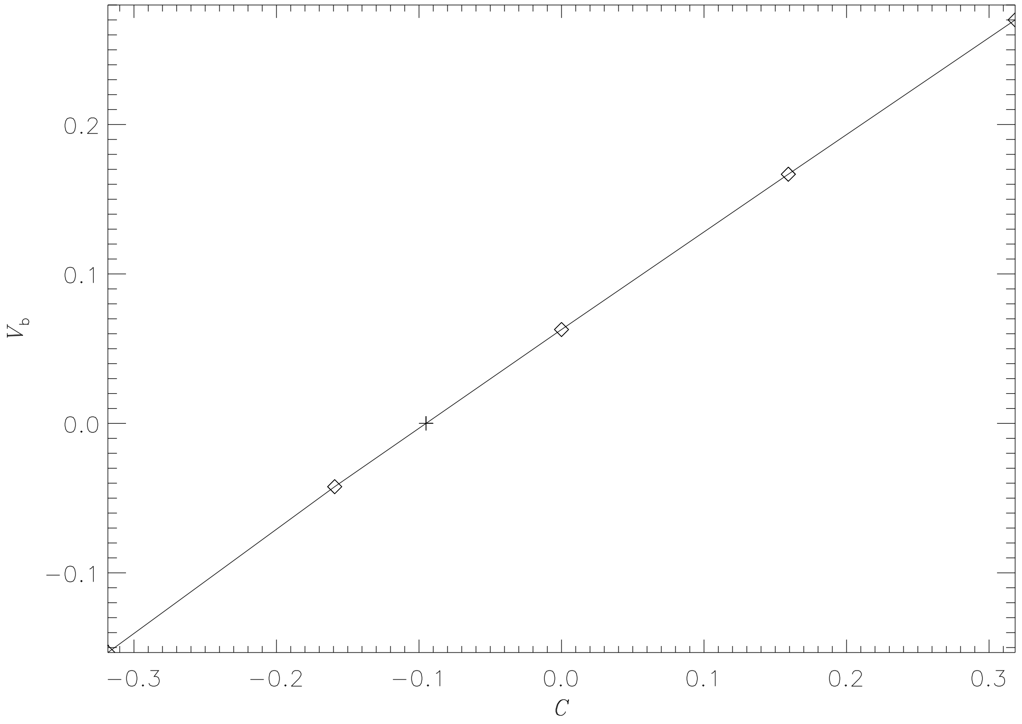

Figure 5.31: Values of V_b for constant a. The (+) represents the point where the vortex patch has zero translational velocity, $V_b = 0$.

5.6 Stationary vortex patches

For sufficiently large negative C, the vortex is forced to propagate contrary to its motion in the absence of a background flow. By adjusting the relaxation algorithm, the required coefficient, C, to bring the vortex patch to rest can be calculated iteratively. Previously, in the algorithm the value C was held constant. Now the translational velocity V_b is set to zero, with the value of C updated at each iteration.

Let $V_b = V_t + CU_b$, where V_t is the translational velocity of the patch with zero background flow and CU_b is the translational velocity calculated due to the background flow, such that

$$U_b = \frac{e^{-y_1/a} - e^{-1/a}}{(y_1 - 1)}. \tag{5.39}$$

V_t is calculated as before, but as V_b is zero, the coefficient C can be deduced:

$$C = -\frac{V_t}{U_b}. \tag{5.40}$$

The new streamfunction, Ψ, is simply the sum of the zero background flow streamfunction, ψ and the background flow streamfunction, ψ_b i.e.

$$\Psi = \psi + \psi_b. \tag{5.41}$$

The boundary of the vortex is computed until the relative difference between successive iterations of C is less than 10^{-6}. Depending on the size of the vortex patch and the value of a, the number of iterations required ranged from as few as ten (for vortex patches of radius 0.05) to 60 (for vortex patches of initial radius 0.475).

Fig. 5.32 shows the steady shapes for $a = 99$ in a background flow such that the patch is at rest along with the steady solutions in the absence of a background flow. As expected, there is no change in shape. The corresponding coefficients C that yield zero translational velocity are plotted against y_1 in Fig. 5.33. As assumed, for constant $a = 99$, as y_1 increases and the vortex patch radius decreases, C also decreases as a background flow with less strength can force the patch to a stop.

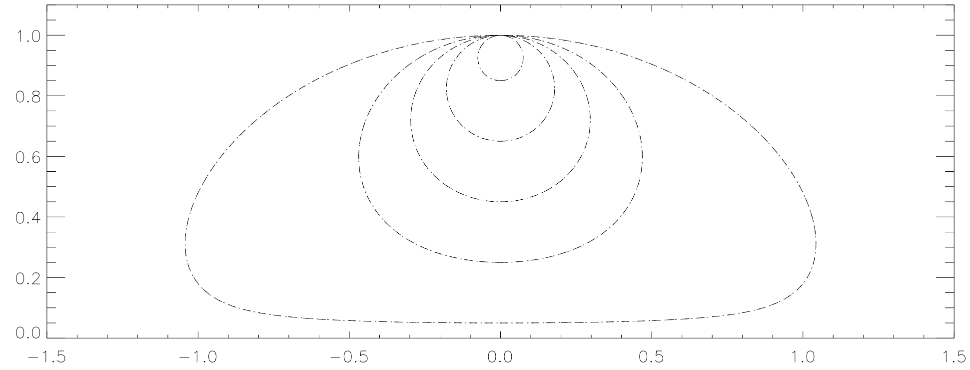

Figure 5.32: Family of solutions for vortex pairs with $a = 99$ such that the vortex patch pair is brought to rest (dotted) and when $C = 0$ (dashed).

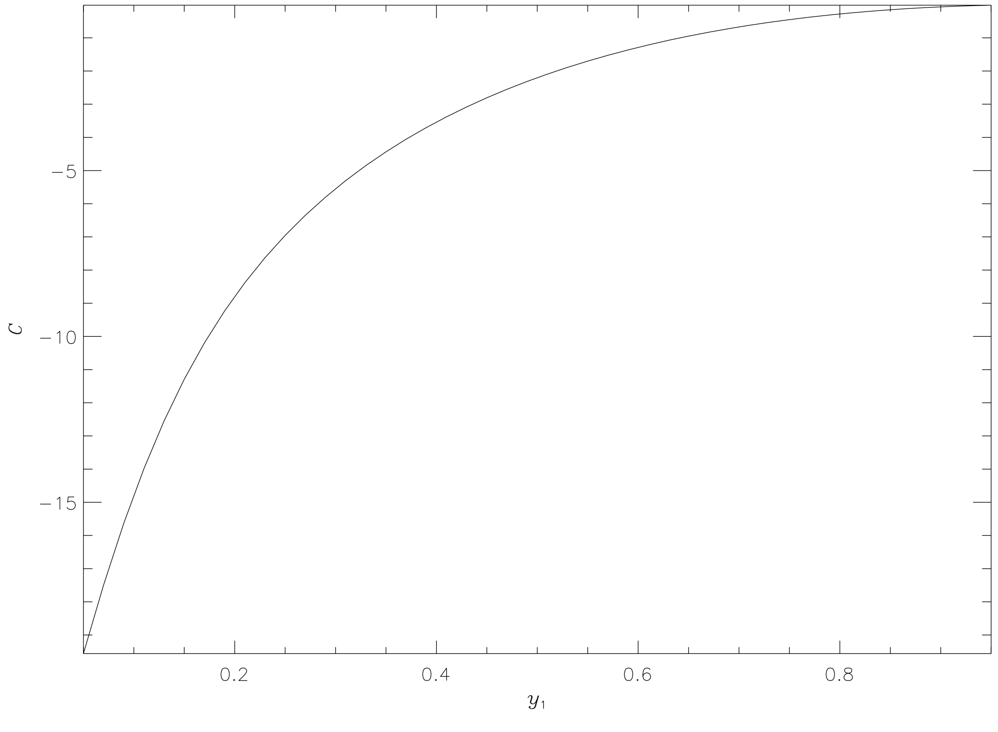

Figure 5.33: C plotted against y_1 with $a = 99$.

The change in patch shape for smaller a is evident in Fig. 5.34, where $a = 1$.

As the vortex patches move slower regardless of background flow, the coefficient required for creating $V_b = 0$ is also smaller than the $a = 99$ case. These coefficients are plotted in Fig. 5.35

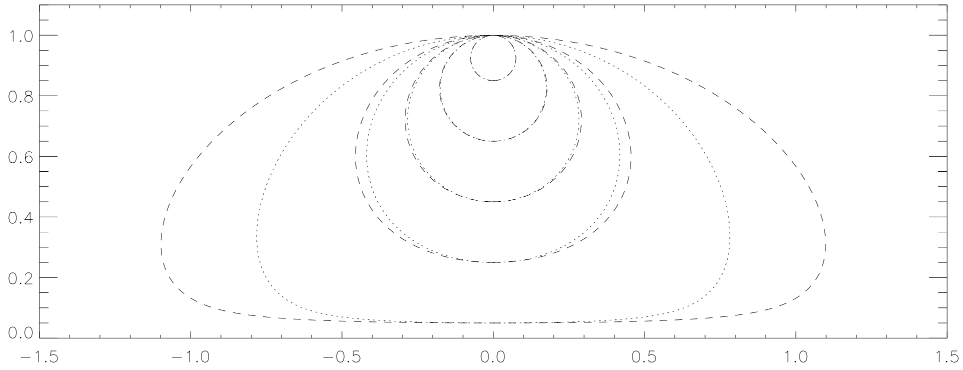

Figure 5.34: Family of solutions for vortex pairs with $a = 1$ such that the vortex patch pair is brought to rest (dotted) and when $C = 0$ (dashed).

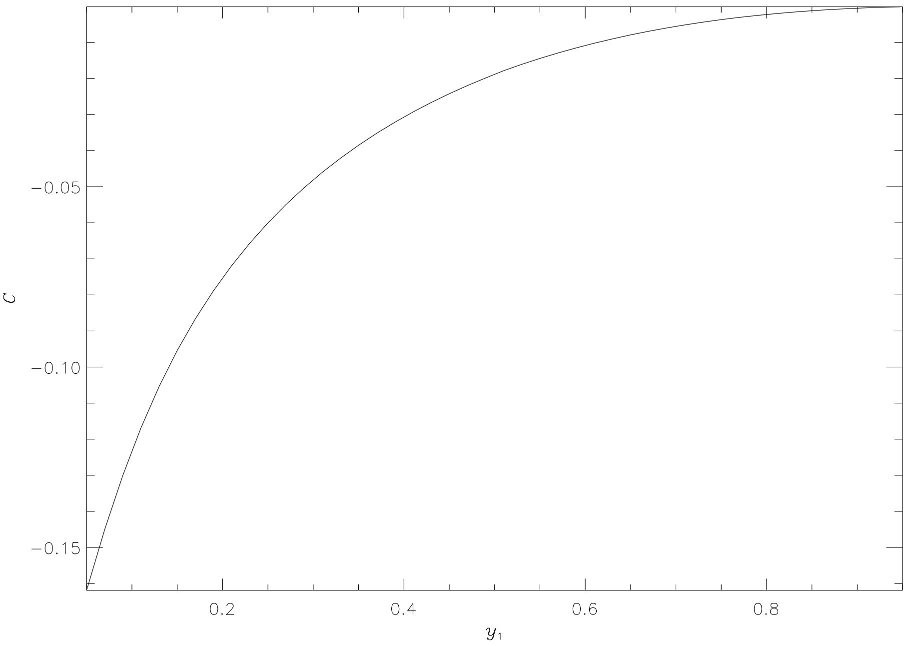

Figure 5.35: C plotted against y_1 with $a = 1$.

In Fig. 5.36, C is calculated and plotted against a when y_1 is fixed at $y_1 = 0.15n, n = 1, \ldots, 5$. As a increases, so does the translational velocity, hence, the magnitude of the strength of the background flow, $|C|$, also increases. As the vortex patches become smaller, the velocity induced by the image vortex also decreases, hence the magnitude required to bring the pair to rest also decreases.

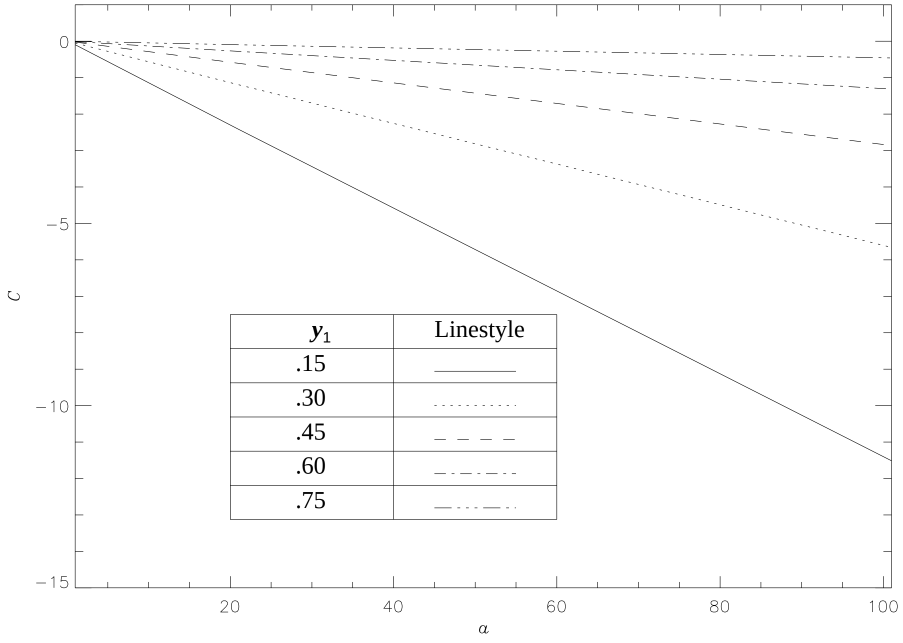

Figure 5.36: C plotted against a with $y_1 = 0.15n, n = 1, \ldots, 5$.

5.6.1 Time dependent advection with background flow

To investigate the stability of the V-states, they are used as initial conditions in the time-dependent contour dynamics code. We examine the effect of both the positive and negative background flow on their evolution. If stable, the structure should persist without changing shape for considerable time. The strength of the background flow in Fig. 5.37-5.38 is $C = \pm 1/2\pi$ with $a = 0.5$ and $y_1 = 0.5$, respectively. The vortex propagates in the positive $x-$direction and was allowed to evolve up to $t = 40$. In Fig. 5.37 there is no change of shape and we conclude the structure is stable.

In Fig. 5.38 $C = -/2\pi$, the vortex is forced backwards. Again, the vortex is

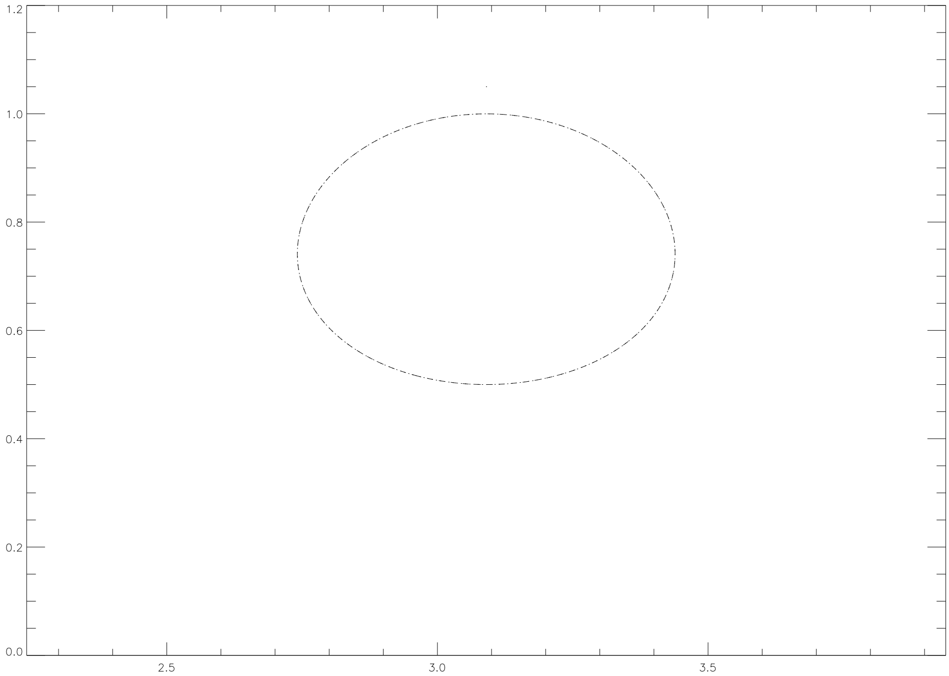

Figure 5.37: Steady vortex patch time-dependent propagation with background flow $C = 1/2\pi$. Snapshot taken at $t = 40$ (dotted) and overplotted with the original vortex patch shape (dashed).

allowed to propagate up to $t = 40$ and there is no discernible change in shape and the vortex appears stable.

The completely stationary vortex patch pairs computed in Section 5.6 are also stable as shown in Fig. 5.39-5.40 where $a = 99$ and $a = 1$ respectively.

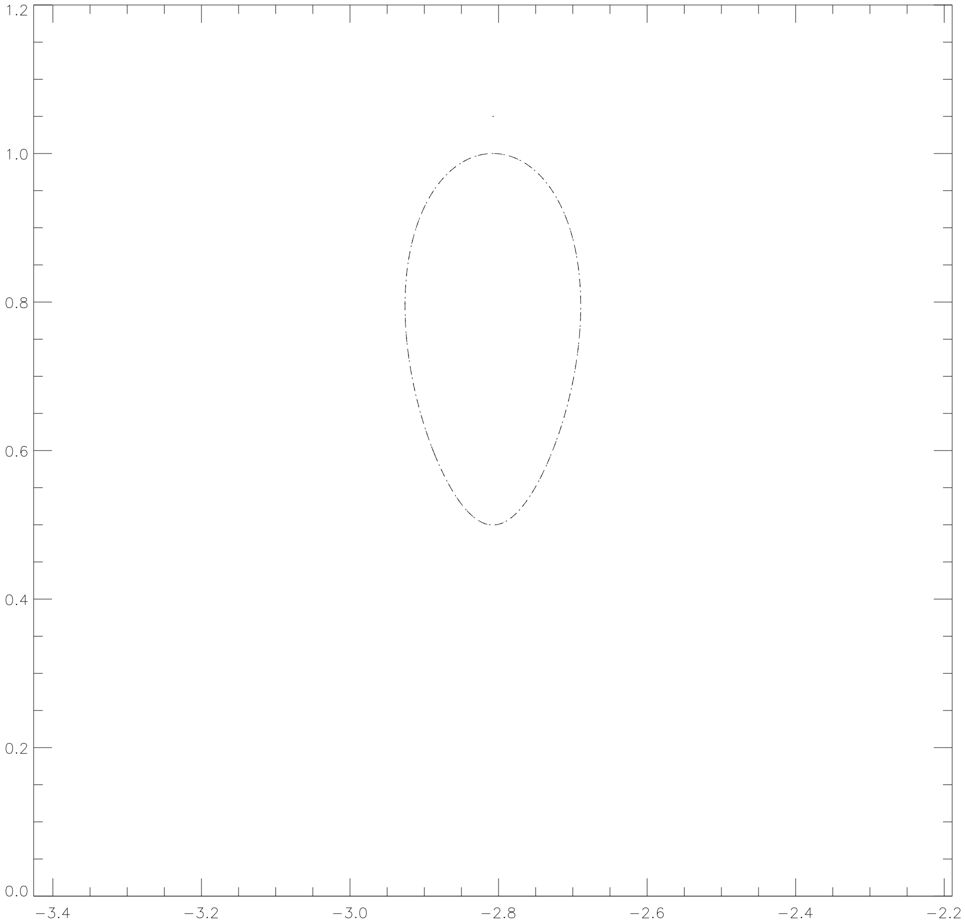

Figure 5.38: Same as in Fig. 5.37 but with $C = -1/2\pi$.

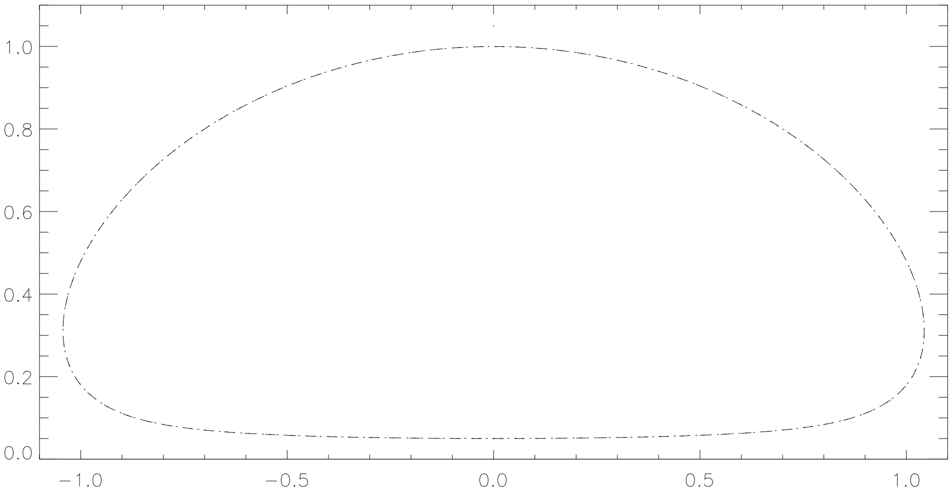

Figure 5.39: The dotted line represents the vortex patch advected with snapshots taken at $t = 10$ with $a = 99$. The dashed line is the original V-state.

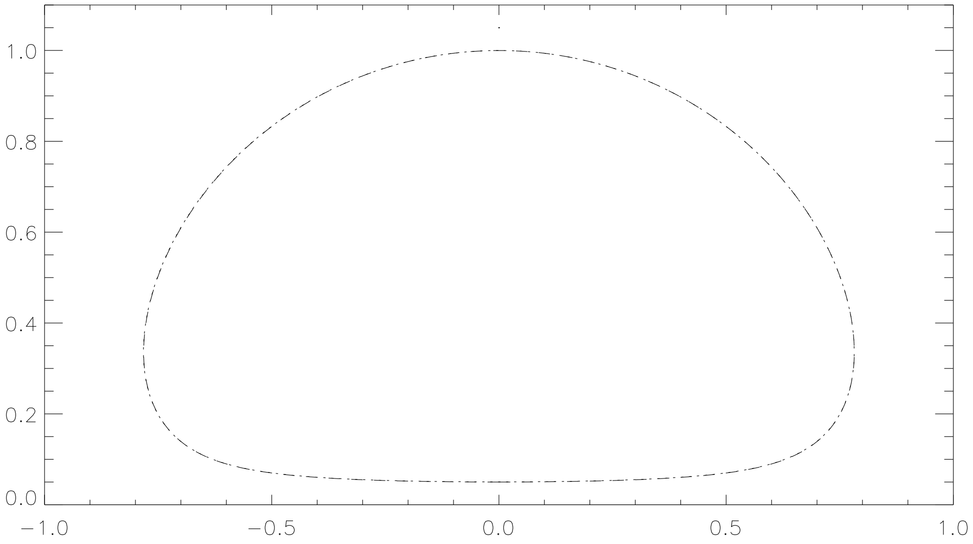

Figure 5.40: Same as in Fig. 5.39 but with $a = 1$.

5.7 Summary

The effects of finite Rossby deformation radius on steady vortex pair motion has been examined. Assuming quasigeostrophic dynamics, Pierrehumbert's (1980) relaxation algorithm was modified to compute the steady state shapes of a pair of counter-rotating vortex patches propagating in a straight line, or, equivalently, the shape of a vortex patch adjacent, and propagating parallel to, an infinite wall.

First, it was noted that for large $a \geq 5$, there was negligible difference in the steady shapes compared to those computed by Pierrehumbert in the rigid-lid case, although there was a slight decrease in the translational velocity, V_t, as a decreases from infinity. This is due to the exponential decay of the velocity induced by the counter-rotating vortex, $K_1(r/a)$ which is used to calculate the velocity at every node along the vortex patch.

Furthermore, the circulation of the patch was scaled by its area to give, $\hat{V_t}$ and compared to the velocity of a pair of equivalent point vortices in the same configuration, with each point vortex located at the centroid of the vortex patches. For large vortex patches that were close together, the steady shapes were quasi-elliptical and move more slowly than the equivalent pair of point vortices. For smaller vortex patches, however, there was good agreement to the equivalent point vortex configuration.

With decreasing a, the change in vortex shape from the rigid-lid case became more apparent. The translational velocities continued to decrease with a decrease in a, due to the exponential decay of $K_1(r/a)$. Small vortex patches with $a < 5$ were more circular than the $a = 5$ case. This is partly due to the fact that the image vortex is not felt as strongly. However, there is a value of a below which the mean radius of large vortex patches starts to increase as a is reduced (see Fig. 5.11).

The method of scaling circulation based on patch area is no longer valid as the behaviour of the translation speed is non-systematic. The method formulated in Chapter 4.1 was used instead which gave good agreement for the small radius vortex patches for all values of deformation radius. As the vortex patches became more deformed from circular, the scaling was no longer applicable.

The stability of the steady shapes were also tested by advecting the vortex patches using the time-dependent contour dynamics code in time and comparing to their original shape. Excellent agreement was found confirming that the vortex pairs were indeed streamlines in a frame moving at a constant horizontal velocity.

The influence of a parallel background shear flow satisfying the Helmholtz equation was also accounted for in the relaxation algorithm. New families of shapes were found and with translational velocities, denoted by V_b. For large a, there is little change in the steady shape since the background flow merely advects the patch at a constant velocity. However, decreasing a gives substantially different vortex equilibrium shapes. As a decreases, the positive background flow stretches the vortex patches horizontally, whereas the negative background flow shrinks the vortex patch in the horizontal direction.

There were also a range of strengths of negative background flows that resulted in the vortex patches travelling in the direction contrary to normal motion in the absence of the background flow. Another modification to the algorithm allowed strengths of background flows to be calculated such that the vortex patch pairs were perfectly stationary.

Both the stability of the family of solutions in the presence of background flows, and including those vortex patches which were stationary were tested using the time dependent contour dynamics code. In all cases for arbitrary a, the equilibria were found to be stable.

Chapter 6

Conclusions and future work

This work examines the effects of the Rossby radius of deformation on vortex interactions in a two dimensional ideal rotating fluid. In chapters 2, 3 and 4, the motion of a vortex near a gap in a wall was studied and in chapter 5 steadily propagating vortex pairs were found.

In chapter 2, large finite a is considered. First modelling the effect of the gap by replacing it with a vortex sheet, an integral equation is derived such that there is no normal flow through the barriers and such that the Helmholtz equation was satisfied at every point inside the fluid except at the point vortex. The hypersingular integral equation was solved iteratively using the solution of the rigid-lid case ($a \to \infty$) found by Johnson and McDonald (2004).

When the vortex approaches the gap, however, a further singularity is encountered in the integrand. Hence, a conjugate method (the barrier method) was also developed for when the vortex is near the gap. The barrier method models the semi-infinite barriers by replacing them by vortex sheets whose strength is determined by solving an integral equation. The two methods are used to find solutions valid for all vortex positions and give good comparisons with the analytical solutions for the rigid-lid case.

For finite a, it was noted that as a decreased, the tendency of vortices to pass through the gap rather than leap across increased. For $a < 1$, the method fails as the initial guess is based on the infinite a case. Thus, another method was developed to solve the integral equation derived using the barrier method.

In chapter 3, the finite, small Rossby radius is considered. The integral equation from the barrier method was solved by discretizing and the resulting set of linear equations solved using matrix inversion techniques. The results using both the iterative method and the matrix method showed good agreement for a range of a. For small a, the point vortex propagates at a notably slower speed, due to the exponential decay of the modified Bessel function K_0 and thus takes longer to notice the presence of the gap. Therefore, when close to the barrier the trajectory is parallel to the wall for longer than the equivalent, larger a, point vortex. However, when starting further from the barrier, when approaching the gap, the point vortex takes longer to notice the downstream barrier and hence, turns into the gap and passes through.

The separatrix, i.e. the critical trajectory separating vortices that either pass through the gap or leap across, was calculated for various a by advecting vortices backwards in time starting from near the origin until the point vortex was travelling with constant horizontal velocity and negligible vertical velocity i.e. point vortex behaviour near an infinitely long wall.

The influence of background flows were also considered by modifying the integral equation. Two cases were considered, the symmetric flow and anti-symmetric flow through the gap. For the symmetric flow case, if the self-induced velocity of the point vortex and direction of the background flow are acting in the same direction (i.e. cooperative), there is an increased ability of a vortex to pass through the gap. By contrast, if the self-induced velocity opposes the background flow, the trajectory will leap across the gap or turn back in on itself and travel in the opposite direction. An example was given showing that if the symmetric flow was strong enough, all vortices from the bottom half plane to the upper half plane pass through the gap, without any vortices leaping across the gap.

When the anti-symmetric flow (which has no rigid-lid analogy) is cooperative (i.e. travelling in the same direction as the point vortex), more vortices pass through the gap. However, when the background flow opposes a point vortex's self-induced velocity, trapped vortex paths near the gap form. Stagnation points were created, the locations of which were dependent on the strength of the background flow.

In chapter 4 the motion of a finite area patch of uniform vorticity (i.e. a vortex patch) near a gap in a wall was investigated using contour dynamics, in the presence of the finite Rossby radius of deformation. The matrix method was used to compute the velocity field at every node along the vortex patch boundary. A new normalisation scheme was introduced so that circular patches travel at the same velocity as a point vortex irrespective of the value of the deformation radius and radius of the patch.

Background flows were also implemented in the finite area patch motion algorithm. Various examples were computed to exemplify the results of the normalisation using the point vortex trajectories, and these demonstrated that near-circular vortices travel at the same speed as the point vortex path. Larger vortex patches deform into less circular shapes which deviate from the point-vortex trajectory.

In chapter 5 the motion of a pair of steadily translating vortex patches were examined. V-states were found for finite a using a modified version of Pierrehumbert's (1980) algorithm. For large a, there was little difference in the shape of the vortex patches found by Pierrehumbert for the rigid-lid case. Decreasing a had interesting results: for small vortex patches the V-states were more circular in comparison to their $a \to \infty$ counterparts, as the effect of the image vortex patch was felt less strongly; on the other hand large vortex patches were more elongated.

The normalisation technique developed in chapter 4 was used to non-dimensionalise the results for arbitrary sized patches. Good agreement was found for circular patches compared to an equivalent point vortex pair (i.e. the point vortex pair were located at the centroids of the vortex patches). The effect of positive and negative background flows parallel to the direction of pair propagation were also investigated with new families of steady solutions being found. For large a the effect of the background flow had no effect on the V-state shape, merely changing the translational velocity. As a decreased, the effect on the V-state shape became more prominent, with positive and negative flows either elongating or constricting the vortex patch in the direction of propagation.

Obvious extensions to the vortex motion near the gap would be to investigate the effects of the Rossby radius on multiple gaps, periodically spaced gaps or circular islands in the same vein as the work done by Johnson and McDonald (2005) and Crowdy and Marshall (2005-2006). Again an integral equation approach could be used here with vortex sheets being aligned with the multiple barriers.

The interaction of a vortex with a bay (or harbour) is of interest. The problem is similar to that considered here except the domain in, say, the lower half plane is of finite area. The vortex would then flush, or mix, fluid between the bay and the larger "infinite" ocean – such flushing problems are of environmental interest.

Perhaps the biggest dynamical phenomenon neglected in this study is that of varying topography – this being more significant than neglect of friction. In the ocean, the sea bed usually slopes uniformly upwards from the deep to the coast. The relatively shallow water near ocean margins gives them a different potential vorticity than the surrounding deep ocean. Any vortex will advect fluid columns leading to a change of depth. Conservation of potential vorticity will cause relative vorticity to be generated which, in turn, will influence the primary vortex. This complex interaction will markedly affect the vortex trajectory. Careful numerical study of this variable topography remains to be done.

The time-dependent interactions of V-states with each other is also of interest, e.g. what happens when V-states propagating in opposite directions collide? Equally, what happens when V-states moving at different speeds in the same direction catch up with each other? Both these questions could be tackled using time-dependent contour dynamics.

Appendix A

Matrix method: derivation of a system of linear equations

The integral equation (3.27) can be approximated by a system of linear equations obtained by discretizing the barrier in the $x-$direction. The singularity present in the integrand is of Cauchy principal value type: $(x - x_0)^{-1}$. Hence, when $|x - x_0|$ is small, the integrand to leading order is

$$\mathcal{E}(x, x_0)\lambda(x) = \frac{\lambda(x)}{x - x_0}. \tag{A.1}$$

The integral is discretised two ways over the interval $[a, b]$ (see Fig. A.1). First $[a, b]$ is discretized uniformly into $N - 1$ sections

$$\begin{aligned} x_i &= a + \frac{(b-a)}{N-1}(i-1) \\ &= 1 + h(i-1), \text{ for } i = 1, \ldots, N, \text{ where } h = \frac{(b-a)}{N-1}. \end{aligned} \tag{A.2}$$

Second, let the midpoints of the line segments between x_i and x_{i+1} be denoted by x_0^i:

$$x_0^j = x_j + \frac{h}{2}, \text{ for } j = 1, \ldots, N-1. \tag{A.3}$$

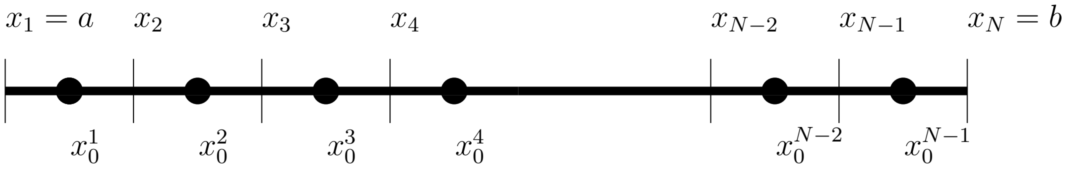

Figure A.1: Discretisation of the barrier $[a, b]$ into N points x_i with midpoint x_0^i.

The integral can written using (A.1) as

$$\begin{aligned}\int_a^b \mathcal{E}(x, x_0)\lambda(x)\,\mathrm{d}x \simeq \int_a^{x_J} \mathcal{E}(x, x_0)\lambda(x)\,\mathrm{d}x + \int_{x_J}^{x_{J+1}} \frac{\lambda(x)}{x - x_0^J}\,\mathrm{d}x \\ + \int_{x_{J+1}}^b \mathcal{E}(x, x_0)\lambda(x)\,\mathrm{d}x,\end{aligned} \tag{A.4}$$

where $x \simeq x_0^j$ is taken to be the approximate location of the singularity. The non-singular terms on the right hand side,

$$\int_a^{x_J} \mathcal{E}(x, x_0)\lambda(x)\,\mathrm{d}x, \int_{x_{J+1}}^b \mathcal{E}(x, x_0)\lambda(x)\,\mathrm{d}x$$

can be integrated numerically in a standard way using the trapezoidal rule i.e.

$$\int_a^{x_J} \mathcal{E}(x, x_0)\lambda(x)\,\mathrm{d}x = \sum_{i=1}^{J} \mathcal{E}(x_i, x_0^J)\lambda(x_i)w_i, \tag{A.5}$$

$$\int_{x_J+1}^{x_N} \mathcal{E}(x, x_0)\lambda(x)\,\mathrm{d}x = \sum_{i=J+1}^{N} \mathcal{E}(x_i, x_0^J)\lambda(x_i)w_i \tag{A.6}$$

where,

$$w_i = \begin{cases} \frac{h}{2} & \text{if } i = 1, J, J+1, N \\ h & \text{otherwise,} \end{cases} \tag{A.7}$$

are the standard weightings of the trapezoidal rule.

This leaves the integral which contains the singularity,

$$\begin{aligned}\int_{x_J}^{x_{J+1}} \mathcal{E}(x,x_0)\lambda(x)\,\mathrm{d}x &= \int_{x_J}^{x_{J+1}} \mathcal{E}(x,x_0)(\lambda(x)-\lambda(x_0^J))\,\mathrm{d}x \\ &\quad + \lambda(x_0^J)\int_{x_J}^{x_{J+1}} \frac{1}{x-x_0^J}\,\mathrm{d}x \\ &= \int_a^b \mathcal{E}(x,x_0)(\lambda(x)-\lambda(x_0^J))\,\mathrm{d}x \end{aligned} \tag{A.8}$$

where the second term of the first line of the right hand side of (A.8) is zero, due to symmetry of the Cauchy Principal Value integral.

The non-singular terms can be integrated approximately as follows

$$\begin{aligned}\int_{x_J}^{x_{J+1}} \mathcal{E}(x,x_0)(\lambda(x)-\lambda(x_0^J))\,\mathrm{d}x \simeq & \frac{h}{2}\mathcal{E}(x_{J+1},x_0^J)\left(\lambda(x_{J+1})-\lambda(x_0^J)\right) \\ & + \frac{h}{2}\mathcal{E}(x_J,x_0^J)\left(\lambda(x_J)-\lambda(x_0^J)\right), \\ = & \frac{h}{2}\mathcal{E}(x_{J+1},x_0^J)\lambda(x_{J+1}) \\ & + \frac{h}{2}\mathcal{E}(x_J,x_0^J)\lambda(x_J). \end{aligned} \tag{A.9}$$

Thus, from (A.5), (A.6) and (A.9),

$$\int_a^b \mathcal{E}(x,x_0)\lambda(x)\,\mathrm{d}x \simeq \sum_{i=1}^{N} \mathcal{E}(x_i,x_0^J)\lambda(x_i)w_i, \tag{A.10}$$

where

$$w_i = \begin{cases} \frac{h}{2} & \text{if } i = 1, N \\ h & \text{otherwise,} \end{cases} \tag{A.11}$$

which is the standard trapezoidal approximation rule.

Thus we have $N-1$ equations,

$$n_e(x_0^i) = \sum_{i=1}^{N} \mathcal{E}(x_i,x_0^J)\lambda(x_i)w_i, \text{ for } J = 1,\ldots,N-1, \tag{A.12}$$

where $n_e(x_0^i)$ is the normal velocity induced along the barrier at point x_0^i, which is known.

To close the system an extra evaluation point, $x_0^N = x_N + h/2$, outside the truncated barrier $[a,b]$. This gives an extra equation,

$$n_e(x_0^N) = \sum_{i=1}^{N} \mathcal{E}(x_i, x_0^N)\lambda(x_i)w_i. \tag{A.13}$$

In matrix form, the N equations (A.12) and (A.13) can be written,

$$\begin{pmatrix} \mathcal{E}(x_1, x_0^1)w_1 & \cdots & \mathcal{E}(x_N, x_0^1)w_N \\ \vdots & \ddots & \vdots \\ \mathcal{E}(x_1, x_0^N)w_1 & \cdots & \mathcal{E}(x_N, x_0^N)w_N \end{pmatrix} \begin{pmatrix} \lambda(x_1) \\ \vdots \\ \lambda(x_N) \end{pmatrix} = \begin{pmatrix} f(x_0^1) \\ \vdots \\ f(x_0^N) \end{pmatrix}. \tag{A.14}$$

Bibliography

Aref, H., Newton, P. K., Stremler, M. A, Tokieda, T., and Vainchtein, D. L. (2003), "Vortex Crystals", *Advances in Appl. Mech.* , Vol. 39, p. 1979.

Cenedese, C., Adduce, C. & Fratantoni, D. M. (2005), "Laboratory experiments on mesoscale vortices interacting with two islands", *J. Geophys. Res.* , Vol. 110, p. C09023.

Crowdy, D. G. (1999), "A class of exact multipolar vortices.", *Phys. FLuids* , Vol. 11, pp. 2556–2564.

Crowdy, D. G. (2002), "Exact solutions for rotating vortex arrays with finite-area cores", *J.Fluid Mech* , Vol. 469, pp. 209–235.

Crowdy, D. G. & Marshall, J. S. (2005), "The motion of a point vortex around multiple circular islands", *Phys. Fluids* , Vol. 17, p. 056602.

Crowdy, D. G. & Marshall, J. S. (2006), "The motion of a point vortex through gaps in walls", *J. Fluid Mech.* , Vol. 551, pp. 31–48.

Deem, G. S. & Zabusky, N (1978), "Stationary 'V-states', interactions, recurrence and breaking", *Phys. Rev. Lett.* , Vol. 40, pp. 859–862.

Dritschel, D. G. (1989), "Contour dynamics and contour surgery: numerical algorithms for extended, high-resolution modelling of vortex dynamics in two-dimensional, inviscid, incompressible flows", *Computer Physics Reports* , Vol. 10, pp. 77–146.

Duran-Matute, M. & Velasco Fuentes, O. U. (2008), "Passage of a barotropic vortex through a gap", *J. Phys. Oceanogr.* , Vol. 38, pp. 2817–2831.

Euler, L. (1757), "Principes generaux du mouvement des fluides", *Mémoires de l'Académie des Sciences de Berlin* , Vol. 11, pp. 274–315.

f, P. G. & Tanveer, S. (1982), "The touching pair of equal and opposite uniform vortices", *Phys. Fluids.* , Vol. 25, pp. 1929–1930.

Fraenkel, E. (1970), "On steady vortex rings of small cross-section in an ideal fluid", *Proc. Roy. Soc. A.* , Vol. 316, pp. 29–62.

Helmholtz, H. (1858), "Über integrale der hydrodynamischen Gleichungen,welche den wirbelbewegungen entsprechen", *J. Reine Agnew. Math.* , Vol. 55, pp. 25–55.

Jochumsen, K., Rhein, M., Hüttl-Kabus, S. & Böning, C.W. (2010), "On the propagation and decay of North Brazil current rings", *J. Geophys. Res.* , Vol. 115, p. C10004.

Johnson, E. R. & McDonald, N. R. (2004), "The motion of a vortex near a gap in a wall", *Phys. Fluids* , Vol. 16, pp. 462–469.

Johnson, E. R. & McDonald, N. R. (2005), "Vortices near barriers with multiple gaps", *J. Fluid Mech.* , Vol. 531, pp. 335–358.

Karman, T. von & Rubac, H. L. (1913), "Über den Mechanismus des Flussigkeitsund Luftwidertands", *Phys. Z* , Vol. 3, pp. 49–59.

Kelvin, Lord (1867), "On Vortex Atoms", *Proc. R. Soc. Edin* , Vol. VI, pp. 94–105.

Kelvin, Lord (1869), "On vortex motion", *Trans. Roy. Soc. Edinburgh.* , Vol. 25, pp. 217–260.

Kelvin, Lord (1878), "Floating magnets (illustrating vortex systems)", *Collected works* , Vol. IV, pp. 135–140.

Küchemann, D. (1965), “Report on the I.U.T.A.M. symposium on concentrated vortex motions in fluids”, *J. Fluid Mech.* , Vol. 21, pp. 1–20.

Lamb, H. (1932), *Hydrodynamics*, Cambridge University Press.

McDonald, N. R. (2004), “A new translating quasigeostrophic V-state”, *European Journal of Mechanics B/Fluids* , Vol. 23, pp. 633–644.

Nof, D. (1994), “Choked flows from the Pacific to the Indian Ocean”, *J. Phys. Oceanogr.* , Vol. 25, p. 1369.

Norbury, J. (1972), “A steady vortex ring close to Hill’s spherical vortex”, *Proc. Cambridge. Phil. Soc.* , Vol. 72, p. 253.

Norbury, J. (1975), “Steady planar vortex pairs in an ideal fluid”, *Comm. Pure Appl. Math.* , Vol. 28, pp. 679–685.

Pedlosky, J. (1994), “Stratified abyssal flow in the presence of fractured ridges”, *J. Phys. Oceanogr.* , Vol. 24, p. 403.

Pierrehumbert, R. T. (1980), “A family of steady, translating vortex pairs with distributed vorticity”, *J. Fluid Mech.* , Vol. 99, pp. 129–144.

Pratt, L. J. & Spall, M. A. (2003), “A porous media theory for geostrophic flow through ridges and archipelagos”, *J. Phys. Oceanogr.* , Vol. 33, pp. 2702–2718.

Richardson, P. L., Bower, A. S. & Zenk, W. (2000), “A census of Meddies tracked by floats”, *Progress in Oceanography* , Vol. 45, pp. 209–250.

Rosenhead, L. (1929), “The Kármán street of vortices in a channel of finite breadth.”, *Phil. R. Soc. Lond.* , Vol. A 208, pp. 275–329.

Sadovskii, V. S (1972), “Vortex regions in a potential stream with a jump of Bernoulli’s constant at the boundary”, *App. Math. Mech.* , Vol. 35, pp. 773–779.

Saffman, P. G. (1992), *Vortex Dynamics*, Cambridge University Press.

Saffman, P. G. & Schatzman, J. C. (1982*a*), "An inviscid model for the vortex street wake", *J. Fluid Mech* , Vol. 122, pp. 467–486.

Saffman, P. G. & Schatzman, J. C. (1982*b*), "Stability of a vortex street of finite vortices", *J. Fluid Mech* , Vol. 117, pp. 171–185.

Saffman, P. G. & Szeto, R. (1980), "The stability of vortex arrays to two- and three-dimensional disturbances", *Fluid Dynamics Research* , Vol. 12, pp. 581–588.

Sheu, W., Wu, C. & Oey, L. (2010), "Blocking and westward passage of eddies in the Luzon Strait", *Deep Sea Res. Part II: Topical Studies in Oceanogr.* , Vol. 57, pp. 1783–1791.

Simmons, H. L. & Nof, D. (2002), "The squeezing of eddies through gaps", *J. Phys. Oceanogr.* , Vol. 32, p. 314.

Tait, P. G. (1867), "Translation of (Helmholtz 1858): On the integrals of the hydrodynamical equations, which express vortex-motion ", *Phil.Mag* , Vol. 33, pp. 485–512.

Thomson, J. J. (1883), *A treatise on the motion of vortex rings*, MacMillan.

Vallis, G. K. (2006), Cambridge University Press.

Vanden-Broeck, J.-M. & Smith, F. T. (2010), "Supercritical two-fluid interactions with surface tension and gravity", *Mathematika* , Vol. 56, pp. 93–106.